NUMERICAL STUDY OF THE AERODYNAMIC CHARACTERISTICS OF
A WAVE DISC ENGINE

By

Guangwei Sun

A DISSERTATION

Submitted to
Michigan State University
In partial fulfillment of the requirements
for the degree of

DOCTOR OF PHILOSOPHY

Mechanical Engineering

2012

ABSTRACT

NUMERICAL STUDY OF THE AERODYNAMIC CHARACTERISTICS OF
A WAVE DISC ENGINE

By

Guangwei Sun

The demand for mobile power generation and low-cost durable and yet efficient and low emission engines is ever increasing. This work focuses on the aerodynamic characteristics of a novel combustion engine – the wave disc engine. This new core technology uses a turbo combustion shock wave technique to efficiently convert fuel sources to mechanical power and subsequently electrical power. In such engines, sudden closing of the flow passage is used to generate shock wave that can enhance combustion and allow for compression and expansion of the operating gases. This new engine concept combines the advantages of (a) high efficiency confined combustion comparable to automotive internal combustion engines (IC-E) and cutting-edge pulse detonation engines (PDE), with (b) the high power density and low maintenance of continuous flow gas turbines (GT), but (c) at a much lower unit cost due to its physical simplicity and compactness.

This work performs a detailed thermodynamic analysis of a Wave Disc Engine by taking a single channel as the control volume as well as a full rotor. The analysis gives the general expression of the net work done by the flow and the thermal efficiency in terms of the mass-average properties, and states that under some certain conditions the operation can achieve the efficiency of Humphrey cycle. Two one-dimensional numerical codes were created using

TVD-MacCormack scheme and Gottlieb-Turkel scheme to provide an estimation of the ports timing for multi-dimensional design. A simple arc was chosen as the channel shape of the baseline engine. After some geometric adjustments, the configuration of the baseline design was determined. However, its efficiency is very low. Energy losses were investigated by a 2D simulation of a single channel. The results showed that the significant outgoing kinetic energy and the under-expansion of the exhaust gas were the main sources of energy loss. To improve the performance of the energy extraction by the curved channels, the mechanism of the torque generation by the expansion wave was studied and the principle for the channel shape design was obtained. Several channel shapes were proposed and tested. Eventually the convergent channel was chosen as the best design and implemented on a full engine. The results showed that the efficiency of the engine increased from 2.2% to 3.3% by using the convergent channel. Then the effects of the peak pressure in the channel and of the tip speed on the engine power and efficiency was investigated. Two methods to reuse the energy from the exhaust gas were proposed – adding a return channel or an external turbine. It was proved by the simulations that both methods can improve the efficiency and adding an external turbine is more effective. At last, various plans to prevent the leakage going into the inlets were compared and the jagged wall design was found to be the best.

TABLE OF CONTENTS

LIST OF TABLES

LIST OF FIGURES

x

NOMENCLATURE

A	area
c	absolute velocity
c_v	constant volume specific heat
c_p	constant pressure specific heat
Cr	courant number
E	total energy in the control volume
h	specific enthalpy
H	enthalpy
k	kinetic energy
$\dot{m}$	mass flow rate
m_{ch}	mass in one channel
N	node number
N_{ch}	channel number of one cycle
p	pressure
Q	heat release
s	specific entropy
T	temperature
T_{cycle}	cycle period
T_{ch}	channel period

u	specific internal energy
W	work done by the fluid
α	ports wall angle
β	blade angle
ρ	density
η	thermal efficiency
γ	specific heat ratio
ω	angular velocity
τ	torque on the channel walls
Δ	discrepancy

Subscripts and Superscripts

1	left boundary node
2	the beginning of the constant volume combustion
3	the end of the constant volume combustion
CV	control volume
c	compression process
e	expansion process
in	inflow
mean	mean value
net	net value

new	new time step
old	old time step
origin	origin point of characteristic line
out	outflow
r	radial component
ref	reference value
s	scavenging process
tot	total property
$\overline{}$	mass-average property
$\cdot$	time rate of property
"	per unit area
θ	tangential component

CHAPTER 1. INTRODUCTION

1.1. Wave Rotor Technology

The idea of the energy exchange between two mediums without any separation goes back to the beginning of the 20th century. In its second decade, along the longitudinal axis perforated drum, a channeled rotor was patented by the German engineer Burghard - a machine delivering an uninterrupted mass flow of the pressurized air [3]. As the unsteady flow theory, a necessity for the development of a usable machine, was not developed until the 1920's and 1930's, Burghard's invention did not succeed in becoming an available device until 1940's when the Brown Boveri (BBC, today ABB) turbocharger engineer Seippel designed a pressure exchanger, also called the wave rotor, as an air compressor of a gas turbine used as the propulsion of an experimental locomotive [3].

1.1.1. Wave Rotor

The wave rotor is a non-steady flow device that uses shock waves to pressurize fluids by transferring energy from a high-pressure flow to a low-pressure flow in narrow channels. For a gas turbine engine application, the wave rotor employs the hot, high pressure exhaust gas from the combustion chamber to generate a shock wave that compresses the cooler, lower pressure air received from the compressor. This results in an increase in both temperature and pressure of the air entering the combustion chamber, allowing for a higher overall pressure ratio for the entire cycle for the fixed turbine inlet temperature. Such pressure exchange wave rotor effectively

combines the steady-state traditional turbomachinery with unsteady, compressible gas flow principles, to allow for higher cycle efficiency.

The wave rotor, shown in Figure 1, consists of a series of axial channels in a rotating drum, driven either by a motor or by V belt direct from the internal combustion (IC) engine crank shaft. The wave rotor was firstly successfully commercialized as an IC engine supercharger by Mazda in 1980's and 90's in serial production of diesel passenger cars [52]. The air inlet represents the low-pressure air received from the compressor (in case of the gas turbine) or from the ambient air (in case of the IC engine supercharger), exhaust inlet is the high-pressure gas (exhaust) from the combustor or from cylinders of the IC engine, exhaust outlet is the low-pressure gas delivered to the turbine from the wave rotor or to the low pressure part of the IC engine exhaust manifold, and air inlet is the high pressure-air delivered to the combustor or to the cylinders of the IC engine from the wave rotor. The rotor channels are placed between two end plates with control ports. The number of ports can vary. Usually, as two cycles per rotor revolution are realized, enabling equal thermal stress, four ports at each of the plates are placed. Each port is designed to expose the channels to the working fluids at a specific shaft angle and for a specific duration. Shock and expansion waves are initiated inside the channels by pressure differences, caused by the port opening and closing. Because the channels are exposed to both hot and cool gases, wave rotors can be naturally self-cooled. Due to the pre-expansion of the burned gases in the wave rotor besides the rotor self-cooling feature, the combustor can operate at higher temperatures without raising the turbine inlet temperature. This is especially important in applications where the temperature is limited by material constraints. Schematic diagrams of the

flow through the channels both for the through flow and reverse flow configurations are shown in Figure 2.

1.1.2. Wave Engine

The wave engine consists of a single wave rotor, used for compression of the inlet air and expansion of the exhaust gas, while producing power. It includes a single steady flow gas turbine type combustor.

In the UK of the mid-1950s, the Ruston-Hornsby Turbine Company, manufacturer of diesel engines and industrial gas turbines, supported the construction and testing of a different kind of wave rotor designed by Pearson [3]. This unique wave rotor, known as the wave engine, has helical axially arranged channels that change the direction of the gas flows producing shaft work similar to a conventional turbine blade. The rotor has a 230 mm diameter and a 76 mm length. The engine worked successfully for several hundred hours in a wide range of operating conditions (from 3000 to 18,000 rpm) without variable porting, and produced up to 26 kW at its design point with a cycle peak temperature of 1070 K and a thermal efficiency of around 10%. Better performance seemed possible with improvements to overcome leakage and incomplete scavenging. Even though large number of seizures occurred due to unexpectedly large axial displacement of the rotor, no engine damage resulted. The design of the engine was based on wave diagrams using the method of characteristics (Figure 2).The sealing and bearings were carefully adapted, considering rotor thermal expansion. Eventually, the engine was wrecked due to over-speeding from an improperly connected fuel line, and the project was canceled.

1.1.3. Wave Combustor

The wave combustor is a wave rotor with the internal combustion which can produce a pressure rise, in comparison to the steady flow combustion which is always accompanied by a pressure loss.

ABB in collaboration with the Swiss Federal Institute of Technology Zurich commenced the design of a full wave rotor with 36 combustor axial channels in 1992 [4].   Each channel had 165 mm length and 15×15 mm cross section (Figure 4). The 200 mm inner-diameter rotor was driven by an electric motor capable of up to 5000 rpm. The spark-plug electric ignition was used for the start up, and the auto injection by the hot gas injection was used for the continuous operation. To start up, two spark plugs with sparking frequency of 3000 Hz located at each end of the rotor and for each cycle would ignite the combustible mixture in the channels from both sides simultaneously. Self-sustaining ignition was accomplished by employing axial jet injection of post combustion gas from a neighboring channel. Although the fuel injection and ignition finally worked fine, tests revealed following shortcomings 1) inhomogeneous mixture in the cell, resulting in a slow diffusion flame, 2) maximum pressure of 9 bar, relative to expected 10–15 bar, presumably due to leakage, which also caused premature ignition and misfiring at higher chamber pressures, 3) excess thermal stresses on the ignition ring, 4) inadequate cantilever single-bearing rotor support, 5) complicated and sensitive electromechanical device for controlling leakage gap. Major remedies recommended making the system better included 1) lead away duct for leakage gas removal, 2) rotor cooling by air, 3) two-sided rotor support, and 4) mechanical control for thermal expansion. The prototype wave combustor operated successfully

until the project was concluded in 1994, due to market concerns.

1.2. Working Principle of the WDE

The Wave Disc Engine (WDE) utilizes a combustion engine cycle consisting of compression, combustion, expansion with work extraction, and heat rejection to the ambience in narrow, radial arranged and curved channels.

The compression work is typically provided through a work generated during expansion. A considerable part of the machinery hardware in the GT and IC-E is devoted to extracting and transmitting the work needed for compression (gray in Figure 5). In a WDE this is mainly performed via shock and pressure waves that are formed in the working fluid and triggered by sudden opening and closing of the channels in the rotating disk to the inlet and outlet ports. Because of this, the hardware of the WDE reduces to about one 1/4 to 1/3 that is necessary to extract the brake horsepower (useful external work) shown in red in Figure 5.

Also, using shockwaves that move with sonic speed reduces the inertia of the hardware and ensures rapid response. With the expansion at sonic speed immediately after combustion, the residence time at high temperature is extremely short, even shorter than in a gas turbine. This results in ultra-low NOx emissions. Furthermore, the relevant heat transfer time and areas are extremely small – dramatically reducing heat losses.

Figure 6 shows a schematic of a WDE. The cycle begins with the sudden closing of the outlet port. A hammer shock wave is generated by the deceleration of the exiting flow to zero velocity and propagates towards the inlet, which in turn compresses the fresh air-fuel mixture

behind the shock wave. The inlet port is still open to allow for more loading. Once the shock wave arrives at the inlet end, the inlet port closes and the mixture in the channel is ignited. After the ignition, the constant volume combustion takes place within the channel, producing a pressure and temperature rise during the combustion process. After the combustion is completed, the outlet end of the channel opens to the ambience. This sudden opening of the channel creates an expansion wave propagating towards the inlet. Torque generation is produced by the fluid tangential momentum at the outlet (jet propulsion). Once the pressure near the inlet end of the channel is lowered down by the expansion wave below the inlet pressure, the inlet port opens and the fresh air-fuel mixture at the inlet pressure is drawn into the channel and flushes the exhaust gas away. Centrifugal force on the flow helps the flushing and loading processes. When the channel is filled up with the mixture, the outlet port closes suddenly. Then the cycle starts over.

1.3. Thermodynamic Cycle Analysis

Researchers have performed the thermodynamic analysis of various unsteady flow devices, such as PDE, wave rotor/combustor topped gas turbine, using either Brayton cycle or Humphrey cycle. Weber's engine operated on the Brayton cycle (Weber [67]). Heiser and Pratt used Humphrey cycle for PDE (Heiser and Pratt [65]). Wintenberger and Shepherd used FJ cycle to model PDEs (Wintenberger and Shepherd [66]). Wilson and Paxson used Brayton cycle to model the wave rotor topped gas turbine (Wilson and Paxson [67]). Kentfield modeled PDEs as a Lenoir cycle (Kentfield [23]).

These analyses were based on the energy equation for steady flow or closed system. Since the flow in the WDE is unsteady as in a PDE, not all working fluid particles undergo identical thermodynamic processes. Besides, a WDE cannot be treated as a closed system. Thus, the energy equation for steady flow or closed system does not apply on the WDE. A new analytical way is presented here by integrating the following energy equation over the control volume and the time:

$$\frac{dE_{CV}}{dt} = \dot{Q} + \dot{m}_{in}h_{tot,in} - \dot{m}_{out}h_{tot,out} - \dot{W} \tag{1.1}$$

where all physical quantities vary with time due to the unsteady nature of the flow, and W indicates the work done by the flow through the control volume. If the value of W is negative, the flow consumes energy; if the value is positive, the energy is extracted from the flow. In this analysis, the leakage is neglected and all walls are assumed to be adiabatic.

1.3.1. Single Channel Analysis

When the WDE operates in a periodic mode, each channel experiences the same working process. Thus, any channel can represent all channels. In this analysis, a single channel was taken as the control volume.

From the closing of the outlet (t_1) to the closing of the inlet (t_2), the channel is filled up with fresh fuel-air mixture which is compressed by the hammer shock wave during this process. Integrating Eq. (1.1) over this duration, we obtain

$$\int_{t_1}^{t_2} \frac{dE_{CV}}{dt} dt = \int_{t_1}^{t_2} \dot{m}_{in}h_{tot,in} dt - W_c \tag{1.2}$$

Rearranging Eq. (1.2), we obtain the compression work done by the fluid in the channel in this compression process, which is

$$
W_c = \int_{t_1}^{t_2} \dot{m}_{in} h_{tot,in} dt - \int_{t_1}^{t_2} \frac{dE_{CV}}{dt} dt
$$

$$
= \int_{t_1}^{t_2} \dot{m}_{in} h_{tot,in} dt + E_1 - E_2 \tag{1.3}
$$

From the closing of the inlet (t_2) to the opening of the outlet (t_3), the constant-volume combustion takes place in the channel. Integrating Eq. (1.1) from t_2 to t_3, we obtain the heat addition to the channel, which is

$$
Q = E_3 - E_2 = \oiiint_{CV} \rho_3 u_3 dV - \iiint_{CV} \rho_2 u_2 dV \tag{1.4}
$$

From the opening of the outlet (t_3) to the opening of the inlet (t_4), the high pressure gas discharges to the ambience and the expansion wave propagates towards the inlet. Integrating Eq. (1.1) from t_3 to t_4, we have

$$
\int_{t_3}^{t_4} \frac{dE_{CV}}{dt} dt = -\int_{t_3}^{t_4} \dot{m}_{out} h_{tot,out} dt - W_e \tag{1.5}
$$

Rearranging Eq. (1.5) we obtain the work done by the gas in the channel, which is

$$
W_e = -\int_{t_3}^{t_4} \dot{m}_{out} h_{tot,out} dt - \int_{t_3}^{t_4} \frac{dE_{CV}}{dt} dt
$$

$$
= -\int_{t_3}^{t_4} \dot{m}_{out} h_{tot,out} dt + E_3 - E_4 \tag{1.6}
$$

From the opening of the inlet (t_4) to the closing of the outlet (t_5/t_1), the fresh mixture is sucked into the channel and the residual exhaust gas is scavenged. At the end of this process, the channel returns to the beginning point of the working cycle. Integrating Eq. (1.1) from t_4 to t_5, we have

$$\int_{t_4}^{t_5} \frac{dE_{CV}}{dt}dt = \int_{t_4}^{t_5} \dot{m}_{in}h_{tot,in}dt - \int_{t_4}^{t_5} \dot{m}_{out}h_{tot,out}dt - W_s \tag{1.7}$$

Rearranging Eq. (1.7) we obtain the work done by the flow in this process:

$$W_s = \int_{t_4}^{t_5} \dot{m}_{in}h_{tot,in}dt - \int_{t_4}^{t_5} \dot{m}_{out}h_{tot,out}dt - \int_{t_4}^{t_5} \frac{dE_{CV}}{dt}dt$$

$$= \int_{t_4}^{t_5} \dot{m}_{in}h_{tot,in}dt - \int_{t_4}^{t_5} \dot{m}_{out}h_{tot,out}dt + E_4 - E_5 \tag{1.8}$$

where $E_1 = E_5$ due to the periodicity.

Adding all three expressions of the work done by the fluid, we obtain

$$W_{net} = W_c + W_e + W_s$$

$$= \left(\int_{t_1}^{t_2} \dot{m}_{in}h_{tot,in}dt + E_1 - E_2 \right) + \left(-\int_{t_3}^{t_4} \dot{m}_{out}h_{tot,out}dt + E_3 - E_4 \right)$$

$$+ \left(\int_{t_4}^{t_5} \dot{m}_{in}h_{tot,in}dt - \int_{t_4}^{t_5} \dot{m}_{out}h_{tot,out}dt + E_4 - E_5 \right)$$

$$= \int_{t_1}^{t_2} \dot{m}_{in}h_{tot,in}dt + E_3 - E_2 - \int_{t_3}^{t_4} \dot{m}_{out}h_{tot,out}dt + \int_{t_4}^{t_5} \dot{m}_{in}h_{tot,in}dt - \int_{t_4}^{t_5} \dot{m}_{out}h_{tot,out}dt$$

$$= Q + \int_{t_1}^{t_2} \dot{m}_{in} h_{tot,in} dt + \int_{t_4}^{t_5} \dot{m}_{in} h_{tot,in} dt - \int_{t_3}^{t_5} \dot{m}_{out} h_{tot,out} dt$$

$$= Q + \int_{t_1}^{t_2} \dot{m}_{in} h_{tot,in} dt + \int_{t_4}^{t_5} \dot{m}_{in} h_{tot,in} dt - \int_{t_3}^{t_5} \dot{m}_{out} h_{tot,out} dt \qquad (1.9)$$

Due to the periodicity,

$$\int_{t_1}^{t_2} \dot{m}_{in} h_{tot,in} dt = \int_{t_1+T_{cycle}}^{t_2+T_{cycle}} \dot{m}_{in} h_{tot,in} dt = \int_{t_5}^{t_2+T_{cycle}} \dot{m}_{in} h_{tot,in} dt \qquad (1.10)$$

Substituting Eq. (1.4), Eq. (1.10) into Eq. (1.9), we have

$$W_{net} = Q + \int_{t_5}^{t_2+T_{cycle}} \dot{m}_{in} h_{tot,in} dt + \int_{t_4}^{t_5} \dot{m}_{in} h_{tot,in} dt - \int_{t_3}^{t_5} \dot{m}_{out} h_{tot,out} dt$$

$$= \oiiint_{CV} \rho_3 u_3 dV - \oiiint_{CV} \rho_2 u_2 dV + \int_{t_4}^{t_2+T_{cycle}} \dot{m}_{in} h_{tot,in} dt - \int_{t_3}^{t_5} \dot{m}_{out} h_{tot,out} dt \quad (1.11)$$

Eq. (1.11) gives the general form of the work output of the channel during the cycle.

The general thermal efficiency is

$$\eta = \frac{W_{net}}{Q} = \frac{Q + \int_{t_4}^{t_2+T_{cycle}} \dot{m}_{in} h_{tot,in} dt - \int_{t_3}^{t_5} \dot{m}_{out} h_{tot,out} dt}{Q}$$

$$= 1 - \frac{\int_{t_3}^{t_5} \dot{m}_{out} h_{tot,out} dt - \int_{t_4}^{t_2+T_{cycle}} \dot{m}_{in} h_{tot,in} dt}{\oiiint_{CV} \rho_3 u_3 dV - \oiiint_{CV} \rho_2 u_2 dV} \qquad (1.12)$$

During the combustion, the mass in the channel consists of two parts: 1) the existing mass

in the channel at t_1 which is $\oiiint\limits_{CV} \rho_1 dV$; and 2) the new mass entering the channel from t_1 to t_2

which is $\int\limits_{t_1}^{t_2} \dot{m}_{in} dt$.

At t_1 the existing mass in the channel is equal to the mass that enters from t_4 to t_5 due to the

periodicity, i.e.,

$$\oiiint\limits_{CV} \rho_1 dV = \int\limits_{t_4}^{t_5} \dot{m}_{in} dt \tag{1.13}$$

Since the exhaust gas in the channels is fully scavenged by the fresh mixture and no mixture

overflows out of the channels when the outlet is closed, the mass contained in the closed channel

is incoming mass during the scavenging and compression processes. Combined with the mass

conservation, we have

$$m_{ch} = \oiiint\limits_{CV} \rho_2 dV = \oiiint\limits_{CV} \rho_3 dV = \oiiint\limits_{CV} \rho_1 dV + \int\limits_{t_1}^{t_2} \dot{m}_{in} dt = \int\limits_{t_4}^{t_5} \dot{m}_{in} dt + \int\limits_{t_1}^{t_2} \dot{m}_{in} dt$$

$$= \int\limits_{t_4}^{t_2 + T_{cycle}} \dot{m}_{in} dt = m_{in} = \int\limits_{t_3}^{t_5} \dot{m}_{out} dt = m_{out} \tag{1.14}$$

Defining mass-average specific internal energy and static temperature as

$$\bar{u}_2 = \frac{\oiiint\limits_{CV} \rho_2 u_2 dV}{\oiiint\limits_{CV} \rho_2 dV} = c_v \bar{T}_2 \tag{1.15}$$

11

$$\bar{u}_3 = \frac{\oiiint\limits_{CV} \rho_3 u_3 dV}{\oiiint\limits_{CV} \rho_3 dV} = c_v \bar{T}_3 \qquad (1.16)$$

Defining mass-average total specific enthalpy and total temperature as

$$\bar{h}_{tot,in} = \frac{\int_{t_4}^{t_2+T_{cycle}} \dot{m}_{in} h_{tot,in} dt}{\int_{t_4}^{t_2+T_{cycle}} \dot{m}_{in} dt} = c_p \bar{T}_{tot,in} \qquad (1.17)$$

$$\bar{h}_{tot,out} = \frac{\int_{t_4}^{t_2+T_{cycle}} \dot{m}_{out} h_{tot,out} dt}{\int_{t_4}^{t_2+T_{cycle}} \dot{m}_{out} dt} = c_p \bar{T}_{tot,out} \qquad (1.18)$$

Substituting Eq. (1.15) - (1.18) into Eq. (1.12), we have

$$\eta = 1 - \frac{\bar{h}_{tot,out} - \bar{h}_{tot,in}}{\bar{u}_3 - \bar{u}_2} = 1 - \frac{c_p \left(\bar{T}_{tot,out} - \bar{T}_{tot,in} \right)}{c_v \left(\bar{T}_3 - \bar{T}_2 \right)} = 1 - \gamma \frac{\bar{T}_{tot,out} - \bar{T}_{tot,in}}{\bar{T}_3 - \bar{T}_2} \qquad (1.19)$$

Eq. (1.19) gives the thermal efficiency in terms of mass-average temperature.

Further assumptions can be made. If the incoming kinetic energy is equal to the outgoing kinetic energy, i.e.,

$$\int_{t_4}^{t_2+T_{cycle}} \dot{m}_{in} \frac{c_{in}^2}{2} dt = \int_{t_3}^{t_5} \dot{m}_{out} \frac{c_{out}^2}{2} dt \qquad (1.20)$$

Eq. (1.12) becomes

$$\eta = 1 - \frac{\int_{t_3}^{t_5} \dot{m}_{out} h_{out} dt - \int_{t_4}^{t_2+T_{cycle}} \dot{m}_{in} h_{in} dt}{\oiiint\limits_{CV} \rho_3 u_3 dV - \oiiint\limits_{CV} \rho_2 u_2 dV} \qquad (1.21)$$

Then all total properties can be replaced with the corresponding static properties, and we have

$$\eta = 1 - \gamma \frac{\overline{T}_{out} - \overline{T}_{in}}{\overline{T}_3 - \overline{T}_2} \tag{1.22}$$

1.3.2. Full Rotor Analysis

Now take the entire rotor as the control volume. When the WDE operates in a periodic mode, the period is the time that it takes for a channel rotates to the position of the next channel. To distinguish with the cycle period, this period is named the channel period T_{ch}. Applying Eq. (1.1) to the rotor, we have

$$\int_{T_{ch}} \frac{dE_{CV}}{dt} dt = \int_{T_{ch}} \dot{Q} dt + \int_{T_{ch}} \iint_{inlet} \dot{m}''_{in} h_{tot,in} dA dt - \int_{T_{ch}} \iint_{outlet} \dot{m}''_{out} h_{tot,out} dA dt - \int_{T_{ch}} \dot{W} dt = 0 \tag{1.23}$$

Where E_{CV}, $\dot{Q}$ and $\dot{W}$ varies with time, and the total enthalpy flow rate not only varies with time, but also has a distribution along the inlet and outlet surface.

Rearranging Eq. (1.23), we have the work output:

$$\int_{T_{ch}} \dot{W} dt = \int_{T_{ch}} \dot{Q} dt + \int_{T_{ch}} \iint_{inlet} \dot{m}''_{in} h_{tot,in} dA dt - \int_{T_{ch}} \iint_{outlet} \dot{m}''_{out} h_{tot,out} dA dt \tag{1.24}$$

Since the exhaust gas in the channels is fully scavenged by the fresh mixture and no mixture overflows out of the channels when the outlet is closed, the mass in the rotor is the mass coming into the rotor during one cycle period. Thus, the mass in any closed channel is the incoming mass during one channel period, and we have

$$m_{ch} = \int_{T_{ch}} \iint_{inlet} \dot{m}''_{in} dA dt \tag{1.25}$$

During one cycle period, the heat is released in N_{ch} channels, meaning that in average the heat is released in one channel during one channel period. The heat release rate is

$$\int\limits_{T_{ch}} \dot{Q}dt = m_{ch}\left(\bar{u}_3 - \bar{u}_2\right) = \left(\bar{u}_3 - \bar{u}_2\right) \int\limits_{T_{ch}\ inlet} \iint \dot{m}''_{in}dAdt \qquad (1.26)$$

Combining Eq. (1.24) and Eq. (1.26), we have the thermal efficiency

$$\eta = \dfrac{\int\limits_{T_{ch}} \dot{W}dt}{\int\limits_{T_{ch}} \dot{Q}dt} = \dfrac{\int\limits_{T_{ch}} \dot{Q}dt + \int\limits_{T_{ch}\ inlet} \iint \dot{m}''_{in}h_{tot,in}dAdt - \int\limits_{T_{ch}\ outlet} \iint \dot{m}''_{out}h_{tot,out}dAdt}{\int\limits_{T_{ch}} \dot{Q}dt}$$

$$= 1 + \dfrac{\int\limits_{T_{ch}\ inlet} \iint \dot{m}''_{in}h_{tot,in}dAdt - \int\limits_{T_{ch}\ outlet} \iint \dot{m}''_{out}h_{tot,out}dAdt}{\left(\bar{u}_3 - \bar{u}_2\right) \int\limits_{T_{ch}\ inlet} \iint \dot{m}''_{in}dAdt} \qquad (1.27)$$

Mass conservation gives

$$\int\limits_{T_{ch}\ inlet} \iint \dot{m}''_{in}dAdt = \int\limits_{T_{ch}\ outlet} \iint \dot{m}''_{out}dAdt \qquad (1.28)$$

Due to the periodicity, the total enthalpy coming through the inlet during one channel period is equal to that coming into one channel during the scavenging and compression processes, namely

$$\int\limits_{T_{ch}\ inlet} \iint \dot{m}''_{in}h_{tot,in}dAdt = \int\limits_{t_4}^{t_2+T_{cycle}} \dot{m}_{in}h_{tot,in}dt \qquad (1.29)$$

Combining Eq. (1.14) and Eq. (1.25), we have

$$m_{ch} = \int\limits_{t_4}^{t_2+T_{cycle}} \dot{m}_{in}dt = \int\limits_{T_{ch}\ inlet} \iint \dot{m}''_{in}dAdt \qquad (1.30)$$

Thus, Eq. (1.17) can be rewritten as

$$\bar{h}_{tot,in} = \frac{\displaystyle\int_{T_{ch}\ inlet}\!\!\iint \dot{m}''_{in}h_{tot,in}\,dAdt}{\displaystyle\int_{T_{ch}\ inlet}\!\!\iint \dot{m}''_{in}\,dAdt} = c_p\bar{T}_{tot,in} \tag{1.31}$$

In the same manner Eq. (1.18) can be rewritten as

$$\bar{h}_{tot,out} = \frac{\displaystyle\int_{T_{ch}\ outlet}\!\!\iint \dot{m}''_{out}h_{tot,out}\,dAdt}{\displaystyle\int_{T_{ch}\ outlet}\!\!\iint \dot{m}''_{out}\,dAdt} = c_p\bar{T}_{tot,out} \tag{1.32}$$

Substituting Eq. (1.31) and Eq. (1.32) into Eq. (1.27), we have the same form of the thermal

efficiency as Eq. (1.19)

$$\eta = 1 - \frac{\bar{h}_{tot,out} - \bar{h}_{tot,in}}{\bar{u}_3 - \bar{u}_2} = 1 - \frac{c_p\left(\bar{T}_{tot,out} - \bar{T}_{tot,in}\right)}{c_v\left(\bar{T}_3 - \bar{T}_2\right)} = 1 - \gamma\frac{\bar{T}_{tot,out} - \bar{T}_{tot,in}}{\bar{T}_3 - \bar{T}_2} \tag{1.19}$$

which shows a consistency between the full rotor analysis and the single channel analysis.

In the sense of mass-average flow, all fluid particles can be considered to be of the

mass-average properties at any instance throughout their passing through the channel. The

thermodynamic cycle can be depicted on a T-s diagram (Figure 7). When they enter the rotor,

they are at the state of "in". After being compressed by the hammer shock wave, they are at the

state of "2". During the combustion, their state changes from "2" to "3" following the

constant-volume curve. Then the burned gas expands to the state of "out". If the "out" state has

the identical pressure of the "in" state, the cycle that the particles undergo is a Humphrey cycle

(or Atkinson cycle).

CHAPTER 2.   1D SIMULATION

A key step in the design process is to determine the ports timing, i.e., when the ports should be

open or closed. When the outlet is open to the ambience, the expansion wave propagates into the

channel towards the inlet end. When reaching the inner housing wall, the expansion wave

reflects. Since there is no analytical solution for the reflected waves, a numerical method should

be used to explore the wave timing. Once the reflected expansion wave lowers the pressure at the

inlet end of the channel down to the ambient pressure, the inlet port should be open. Then the

fresh mixture is drawn into the channel. Once the channel is filled up with the mixture and

exhaust gas is cleared away from the channel, the outlet port should be closed. Then a hammer

shock wave is generated by the closing of the outlet and propagates towards the inlet. Once the

shock wave arrives at the inlet, the inlet port should be closed. Thus, the determination of the

ports timing depends on the wave pattern.

Spalding at Imperial College seems to be the first investigator using a 1D numerical method

to investigate unsteady flows inside wave rotors in early 1970s. He has formulated a numerical

procedure considering the effects of heat transfer and friction. The program was later developed

by Jonsson (Jonsson et al [23]), and it was successfully applied to pressure exchangers

calculations (Matthews [27], Azim [7], Azoury and Hai [8]). In the same time, at ABB in

Switzerland, Zehnder [69]-[71] developed and used a finite difference code for evaluation of the

flow in pressure wave machines. By initiating a wave rotor research at NASA Lewis (now Glenn)

Research Center in the late 1980s, Paxson [35][36] has developed a one-dimensional gas

dynamic model to calculate design geometry and off-design wave rotor performance. The model solves the unsteady flow field in an axial passage for time-varying inlet and outlet port conditions, using simplified models to account for losses due to gradual passage opening and closing, viscous and heat transfer effects, leakage, and non-uniform port flow field mixing. Recent improvement and validations have completed it as a preliminary and general design tool Paxson [37]-[40],[41],[42]).

Fatsis and Ribaud from the French National Aerospace Research Establishment (ONERA) have also developed a one-dimensional numerical code based on an approximate Rieman solver taking into account viscous, thermal, and leakage losses (Fatsis and Ribaud [43]-[16]). The code has been also compared with experimental data and applied to three-port, throughflow, and reverse-flow configurations.

Group guided by Reizes in Australia tried to make some attempts to wave rotor technology [59] performing several calculations of shock wave motion in rotating shock tubes. Have been undertaken also attempts of using analytical methods for design of wave rotor cycles (Resler, Moscari and Nalim [56]).

In 2007, Piechna created a 1D code using the Lax-Wendroff scheme taking into account the changing cross sectional area (Piechna [52]).

2.1. Numerical Scheme

First, a 1D code was made to simulate the flow in a rotating straight channel for the preliminary investigation. It is assumed that the flow is along the length the channel (x-direction), the

variables do not change along the width (y-direction), the walls are adiabatic and there is no leakage between the channel and the housing walls. All kinds of gas in the channel were treated as ideal gas and the viscous forces were neglected.

First, the Gottlieb-Turkel scheme was applied to solve the governing equation

$$\frac{\partial U}{\partial t} = -\frac{\partial F}{\partial x} + J \tag{2.1}$$

where $U = \begin{Bmatrix} \rho \\ \rho u \\ \rho e \end{Bmatrix} = \begin{Bmatrix} \rho \\ \rho u \\ \rho c_v T \end{Bmatrix}$ is the solution vector, $F = \begin{Bmatrix} \rho u \\ \rho u^2 + p \\ \rho eu \end{Bmatrix} = \begin{Bmatrix} \rho u \\ \rho u^2 + p \\ \rho c_v Tu \end{Bmatrix}$ is the flux

vector, $J = \begin{Bmatrix} 0 \\ \rho \omega^2 x \\ -p\frac{\partial u}{\partial x} \end{Bmatrix}$ is the source term. In this chapter, u represents the velocity and e the

internal energy.

The element equations are the continuity equation, the x-momentum equation and the energy equation.

Along with Gottlieb-Turkel scheme, fourth order artificial dissipation terms were also explicitly added to reduce the numerical oscillations near the sudden discontinuities (Anderson [1]). For comparison, a TVD-MacCormack (TVDM) scheme was used to solve the problem as well. Both schemes are based on the MacCormack scheme.

2.1.1. Gottlieb-Turkel Scheme

In 1969, MacCormack introduced a two-stage numerical scheme for compressible flows with a

predictor stage followed by a corrector stage (MacCormack [62]). The scheme is second-order accurate in both space and time and is widely applicable, in part, because of its simplicity and robustness. Gottlieb and Turkel improved the MacCormack scheme to fourth-order in space and second-order in time. This scheme has been popular among researchers involved with highly resolved flow fields (Gottlieb and Turkel [63]).

The Gottlieb-Turkel (GT) scheme consists of two steps, predictor step and corrector step. The procedure of the GT scheme is described as follows.

1) Set the initial values of ρ, p, T, u and calculate the initial U and F at all grid points.

2) In the predictor step, the predicted time derivative $\left[\left(\frac{\partial U}{\partial t} \right)_i^t \right]^*$ at the internal points is calculated based on the known values at time level t by replacing the spatial derivative on the right-hand of Eq. (2.1) with a fourth order 3-point backward differencing, as follows.

$$\left[\left(\frac{\partial U}{\partial t} \right)_i^t \right]^* = -\left(\frac{7F_i^t - 8F_{i-1}^t + F_{i-2}^t}{6\Delta x} \right) + J_i^t, \quad i = 2,3,\ldots,N-1 \tag{2.2}$$

3) The predicted solution vector at time level $t + \Delta t$, $\left(\overline{U} \right)_i^{t+\Delta t}$ is calculated using Eq. (2.3).

$$\left(\overline{U} \right)_i^{t+\Delta t} = U_i^t + \left[\left(\frac{\partial U}{\partial t} \right)_i^t \right]^* \Delta t + S_i^t, \quad i = 2,3,\ldots,N-1 \tag{2.3}$$

where S_i^t is the artificial viscosity term, calculated using Eq. (2.4).

$$S_i^t = C_x \frac{\left| P_{i+1}^t - 2P_i^t + P_{i-1}^t \right|}{P_{i+1}^t + 2P_i^t + P_{i-1}^t} \left(U_{i+1}^t - 2U_i^t + U_{i-1}^t \right), \quad 0.01 \leq C_x \leq 0.3 \tag{2.4}$$

4) Use $\left(\overline{U}\right)_i^{t+\Delta t}$ to calculate the predicted values of $\overline{\rho}_i^{t+\Delta t}$, $\overline{T}_i^{t+\Delta t}$, $\overline{u}_i^{t+\Delta t}$ and use $p = \rho RT$ to calculate $\overline{p}_i^{t+\Delta t}$, and then calculate $\overline{F}_i^{t+\Delta t}$ and $\overline{J}_i^{t+\Delta t}$ based on $\overline{\rho}_i^{t+\Delta t}$, $\overline{T}_i^{t+\Delta t}$, $\overline{u}_i^{t+\Delta t}$ and $\overline{p}_i^{t+\Delta t}$.

5) In the corrector step, the time derivative of the predicted solution vector, $\left(\dfrac{\partial \overline{U}}{\partial t}\right)_i^{t+\Delta t}$, is calculated based on the $\overline{F}_i^{t+\Delta t}$ and $\overline{J}_i^{t+\Delta t}$ by replacing the spatial derivative on the right-hand of Eq. (1.1) with fourth order 3-point forward differencing, as follows.

$$\left(\frac{\partial \overline{U}}{\partial t}\right)_i^{t+\Delta t} = -\left(\frac{-7\overline{F}_i^{t+\Delta t} + 8\overline{F}_{i+1}^{t+\Delta t} - \overline{F}_{i+2}^{t+\Delta t}}{6\Delta x}\right) + \overline{J}_i^{t+\Delta t}, i = 2,3,\ldots,N-1 \qquad (2.5)$$

6) The average value of the time derivative is obtained from the arithmetic mean of $\left[\left(\dfrac{\partial U}{\partial t}\right)_i^{t}\right]^{*}$

and $\left(\dfrac{\partial \overline{U}}{\partial t}\right)_i^{t+\Delta t}$.

$$\left[\left(\frac{\partial U}{\partial t}\right)_i^{t+\Delta t}\right]_{avg} = \frac{1}{2}\left\{\left[\left(\frac{\partial U}{\partial t}\right)_i^{t}\right]^{*} + \left(\frac{\partial \overline{U}}{\partial t}\right)_i^{t+\Delta t}\right\}, \quad i = 2,3,\ldots,N-1 \qquad (2.6)$$

7) The corrected solution vector at time level $t+\Delta t$, $U_i^{t+\Delta t}$, is calculated using Eq. (2.7).

$$U_i^{t+\Delta t} = U_i^{t} + \left[\left(\frac{\partial U}{\partial t}\right)_i^{t+\Delta t}\right]_{avg} \Delta t + \overline{S}_i^{t+\Delta t}, \quad i = 2,3,\ldots,N-1 \qquad (2.7)$$

where

$$\overline{S}_i^{t+\Delta t} = C_x \frac{\left|\overline{P}_{i+1}^{t+\Delta t} - 2\overline{P}_i^{t+\Delta t} + \overline{P}_{i-1}^{t+\Delta t}\right|}{\overline{P}_{i+1}^{t+\Delta t} + 2\overline{P}_i^{t+\Delta t} + \overline{P}_{i-1}^{t+\Delta t}}\left(\overline{U}_{i+1}^{t+\Delta t} - 2\overline{U}_i^{t+\Delta t} + \overline{U}_{i-1}^{t+\Delta t}\right), \quad 0.01 \le C_x \le 0.3 \quad (2.8)$$

8) Use $U_i^{t+\Delta t}$ to calculate the corrected values of $\rho_i^{t+\Delta t}$, $T_i^{t+\Delta t}$, $u_i^{t+\Delta t}$ and use $p = \rho RT$ to

calculate $p_i^{t+\Delta t}$, and then calculate $F_i^{t+\Delta t}$ and $J_i^{t+\Delta t}$ based on $\rho_i^{t+\Delta t}$, $T_i^{t+\Delta t}$, $u_i^{t+\Delta t}$

and $p_i^{t+\Delta t}$.

9) Go back to step (3) to run a new iteration until the final time.

In this code, the time step size is determined by the Courant-Friedrichs-Lowry (CFL)

criterion and given by

$$\Delta t^t = \min\left(\Delta t_i^t\right), i = 2,3,\ldots,N-1 \tag{2.9}$$

where

$$\Delta t_i^t = Cr\frac{\Delta x}{\left(\left|u_i^t\right| + a_i^t\right)} \tag{2.10}$$

with Cr being the Courant number and set to be 0.8 in this code.

2.1.2. TVD-MacCormack Scheme

Total-variation-diminishing (TVD) algorithm is used to eliminate the numerical oscillations in

the vicinity of discontinuities. In this section, a TVDM scheme (Dongfang Liang et al [64]) is

used. This scheme includes the addition of a five-point symmetric total variation diminishing

(TVD) term to the corrector step of the standard MacCormack scheme.

The procedure of the TVDM scheme is described as follows.

1) Set the initial values of ρ, p, T, u and calculate the initial U and F at all grid points.

2) In the predictor step, the predicted time derivative $\left[\left(\dfrac{\partial U}{\partial t}\right)_i^t\right]^*$ at the internal points is

calculated based on the known values at time level t by replacing the spatial derivative on

the right-hand of Eq. (2.1) with a second order backward difference, as follows.

21

$$\left[\left(\frac{\partial U}{\partial t}\right)_i^t\right]^* = -\left(\frac{F_i^t - F_{i-1}^t}{\Delta x}\right) + J_i^t, \quad i = 2,3,\ldots,N-1 \tag{2.11}$$

3) The predicted solution vector at time level $t + \Delta t$, $\left(\bar{U}\right)_i^{t+\Delta t}$, is calculated using Eq. (2.12).

$$\left(\bar{U}\right)_i^{t+\Delta t} = U_i^t + \left[\left(\frac{\partial U}{\partial t}\right)_i^t\right]^* \Delta t, \quad i = 2,3,\ldots,N-1 \tag{2.12}$$

4) Use $\left(\bar{U}\right)_i^{t+\Delta t}$ to calculate the predicted values of $\bar{\rho}_i^{t+\Delta t}$, $\bar{T}_i^{t+\Delta t}$, $\bar{u}_i^{t+\Delta t}$ and use $p = \rho RT$

to calculate $\bar{p}_i^{t+\Delta t}$, and then calculate $\bar{F}_i^{t+\Delta t}$ and $\bar{J}_i^{t+\Delta t}$ based on $\bar{\rho}_i^{t+\Delta t}$, $\bar{T}_i^{t+\Delta t}$, $\bar{u}_i^{t+\Delta t}$

and $\bar{p}_i^{t+\Delta t}$.

5) In the corrector step, the time derivative of the predicted solution vector, $\left(\frac{\partial \bar{U}}{\partial t}\right)_i^{t+\Delta t}$, is

calculated based on the $\bar{F}_i^{t+\Delta t}$ and $\bar{J}_i^{t+\Delta t}$ by replacing the spatial derivative on the

right-hand of Eq. (2.1) with forward difference, as follows.

$$\left(\frac{\partial \bar{U}}{\partial t}\right)_i^{t+\Delta t} = -\left(\frac{\bar{F}_{i+1}^{t+\Delta t} - \bar{F}_i^{t+\Delta t}}{\Delta x}\right) + \bar{J}_i^{t+\Delta t}, \quad i = 2,3,\ldots,N-1 \tag{2.13}$$

6) The average value of the time derivative is obtained from the arithmetic mean of $\left[\left(\frac{\partial U}{\partial t}\right)_i^t\right]^*$

and $\left(\frac{\partial \bar{U}}{\partial t}\right)_i^{t+\Delta t}$.

$$\left[\left(\frac{\partial U}{\partial t}\right)_i^{t+\Delta t}\right]_{avg} = \frac{1}{2}\left\{\left[\left(\frac{\partial U}{\partial t}\right)_i^t\right]^* + \left(\frac{\partial \bar{U}}{\partial t}\right)_i^{t+\Delta t}\right\}, \quad i = 2,3,\ldots,N-1 \tag{2.14}$$

7) The corrected solution vector at time level $t + \Delta t$, $U_i^{t+\Delta t}$, is calculated using Eq. (13).

22

$$U_i^{t+\Delta t} = U_i^t + \left[\left(\frac{\partial U}{\partial t}\right)_i^{t+\Delta t}\right]_{avg} \Delta t + TVD_i, \quad i = 2,3,\ldots, N-1 \tag{2.15}$$

where

$$TVD_i = \left[G\left(r_i^+\right) + G\left(r_{i+1}^-\right)\right]\left(U_{i+1}^t - U_i^t\right) - \left[G\left(r_{i-1}^+\right) + G\left(r_i^-\right)\right]\left(U_i^t - U_{i-1}^t\right) \tag{2.16}$$

$$r^+ = \frac{\left(U_i^t - U_{i-1}^t\right)\left(U_{i+1}^t - U_i^t\right)}{\left(U_{i+1}^t - U_i^t\right)\left(U_{i+1}^t - U_i^t\right)} \tag{2.17}$$

$$r^- = \frac{\left(U_i^t - U_{i-1}^t\right)\left(U_{i+1}^t - U_i^t\right)}{\left(U_i^t - U_{i-1}^t\right)\left(U_i^t - U_{i-1}^t\right)} \tag{2.18}$$

The function G() is defined as

$$G(x) = 0.5C[1 - \varphi(x)] \tag{2.19}$$

where the flux limiter function is given as

$$\varphi(x) = \max\left(0, \min(2x, 1)\right) \tag{2.20}$$

and the variable C is

$$C = \begin{cases} Cr(1 - Cr), & Cr \leq 0.5 \\ 0.25, & Cr > 0.5 \end{cases} \tag{2.21}$$

8) Use $U_i^{t+\Delta t}$ to calculate the corrected values of $\rho_i^{t+\Delta t}$, $T_i^{t+\Delta t}$, $u_i^{t+\Delta t}$ and use $p = \rho RT$ to

   calculate $p_i^{t+\Delta t}$, and then calculate $F_i^{t+\Delta t}$ and $J_i^{t+\Delta t}$ based on $\rho_i^{t+\Delta t}$, $T_i^{t+\Delta t}$, $u_i^{t+\Delta t}$

   and $p_i^{t+\Delta t}$.

9) Go back to step (3) to run a new iteration until the final time.

   The time step size is determined in the same way as in the previous section.

2.1.3. Boundary Conditions

Three types of boundary conditions (B.C.s) were used in this code:

Inflow

The stagnation pressure and temperature are imposed; the velocity and density are determined by Piechna's method (Piechna [52]) which is a combination of energy equation

$$\frac{a_{in}^2}{\gamma - 1} = \frac{a_1^2}{\gamma - 1} + \frac{u_1^2}{2} \tag{2.22}$$

and the compatibility relation

$$a_{1new} = a_{origin} + \frac{\gamma - 1}{2}\left(u_{1new} - u_{origin}\right) \tag{2.23}$$

The static pressure is obtained from the isentropic relation

$$\frac{T_{1new}}{T_{tot,in}} = \left(\frac{p_{1new}}{p_{tot,in}}\right)^{\frac{\gamma - 1}{\gamma}} \tag{2.24}$$

Outflow

If the outflow is subsonic, the static pressure is imposed; temperature and velocity are determined by a simple linear extrapolation method using the information of the interior nodes; if the outflow is supersonic, the static pressure, temperature and velocity are all determined by the linear extrapolation (Anderson [1]):

$$p_N = \begin{cases} 2p_{N-1} - p_{N-2}, & supersonic \\ p_{out}, & subsonic \end{cases} \tag{2.25}$$

$$u_N = 2u_{N-1} - u_{N-2} \tag{2.26}$$

$$T_N = 2T_{N-1} - T_{N-2} \tag{2.27}$$

24

Solid Wall

In the case of right closed end wall the simplest but efficient B.C.s are following:

$$p_N = p_{N-1} \qquad (2.28)$$

$$u_N = -u_{N-1} \qquad (2.29)$$

$$T_N = T_{N-1} \qquad (2.30)$$

They represent the existence of the rigid wall between node N and node N-1. In the similar way the B.C.s on the left end wall can be defined (Piechna [52]).

2.2. Determination of the Ports Timing

The procedure to determine the ports timing is as follows:

a) In the initialization step, the temperature and pressure in the channel are specified and the velocity is set to 0.

b) At the beginning of the simulation, the outflow B.C. is applied to the outlet and the solid wall B.C. is applied to the inlet.

c) Once the pressure at the inlet end of the channel is below the inlet pressure ($p(1) < p_{tot,in}$), the inlet B.C. is switched from the solid wall B.C. to the inflow B.C. and the Inlet Opening time is recorded.

d) Once the condition of $T(0.98N)_{new} > 3T(0.98N)_{old}$ is satisfied, the interface between the mixture and the exhaust gas is considered as arriving at the outlet. Then the outlet B.C. is switched from the outflow B.C. to the solid wall B.C. and the Outlet Closing time is recorded.

e) Once the condition of $u(0.02N)_{new} < 0.2u(0.02N)_{old}$ is satisfied, the hammer shock wave is about to arrive at the inlet. Then the simulation stops and the Inlet Closing time is recorded.

f) The Inlet Opening time, Outlet Closing time and Inlet Closing time multiplied by the angular velocity yields the Inlet Opening angle AI_open, Outlet Closing angle OC_open and Inlet Closing angle IC_closed.

2.3. Test Case and Results

A test case was tested to validate the code. The dimension of the computational domain and the working condition is shown in Table 2-1, where $p_{tot,in}$ and $T_{tot,in}$ are the total pressure and total temperature at the inlet, p_0 and T_0 are the initial pressure and temperature in the channel, and p_{out} is the static pressure at the outlet.

Table 2-1: Dimension of the computational domain and the working condition of the test case for the validation of the 1D code

IR (cm)	OR (cm)	$p_{tot,in}$ (Pa)	$T_{tot,in}$ (K)	p_0 (Pa)	T_0 (K)	p_{out} (Pa)	RPM
5	10	111325	300	709275	2100	101325	10000

The wave diagram was obtained from the TVDM scheme, shown in Figure 8. From the pressure contour it can be clearly seen that after the opening of the outlet, an expansion wave propagates towards the inlet, lowering down the pressure; and then it is reflected on the inlet wall and the reflected expansion wave propagates towards the outlet; once arriving at the outlet, the reflected expansion wave is reflected as a compression wave due to the subsonic outflow; during the scavenging process expansion waves and compression waves travels back and forth; once the outlet closes a hammer shock wave is generated and propagates towards the inlet. From the temperature contour it can be seen that the expansion waves decrease the temperature and a clear interface lies between the exhaust gas and the fresh mixture.

Table 2-2 lists the ports timing results from two schemes. The discrepancy shows that they are consistent.

Table 2-2: Ports timing obtained by GT scheme and TVDM scheme

	GT	TVDM	Discrepancy (%)
$t_{IO}(\times 10^{-4}s)$	1.3331	1.3340	0.07
$t_{OC}(\times 10^{-4}s)$	4.3046	4.3292	0.57
$t_{IC}(\times 10^{-4}s)$	6.0082	6.0538	0.76

Analytical time for the head of the expansion wave to arrive at the inlet end is calculated as follows:

$$t = \frac{L}{a} = \frac{L}{\sqrt{\gamma RT}} = \frac{0.05}{\sqrt{1.4 \times 287 \times 2100}} = 5.44 \times 10^{-5} s \qquad (2.31)$$

Figure 9 shows the property profiles of two schemes at 5.44×10^{-5} s. It can be seen that their profiles overlap with each other, which shows a perfect consistency between them; the heads of the expansion waves arrives at the inlet end, which is consistent with the analytic result.

Figure 10 shows the comparison between the results from GT scheme and TVDM scheme at 7×10^{-5} s. The diagrams show that the results from two 1D codes match well.

Once the pressure at the inlet wall is just below the inlet pressure, the channel inlet opens and the mixture is sucked into the channel. The mixture-exhaust interface can be obtained by tracking the discontinuity location in the profiles. Figure 11 shows that the result from the GT scheme and that from the TVDM scheme match well, but near the continuity the TVDM scheme has some numerical oscillations.

Once the code sees the mixture-exhaust interface arrives at the outlet, the channel outlet

closes and a hammer shock is generated by bringing the mixture to rest. The location of the shock wave can be obtained by tracking the discontinuity location in the profiles. Figure 12 shows that the wave front from the GT scheme is slightly ahead of that from the TVDM scheme, which is because the outlet closed earlier in the GT scheme. When the inlet is closed, the pressure in the channel is approximately 180000 Pa, which means the precompression ratio by the hammer shock wave is 180000/111325 = 1.6.

2.1.Particle Tracking

It is useful to analyze the thermodynamic cycle of the engine through the T-s diagram and p-v diagram. However, since the flow is unsteady, not all fluid particles experience the same thermodynamic cycle and the flow field changes with time. Thus, the diagrams cannot be drawn by acquiring data on various locations along the flow at one time instance as in a steady-state flow. Tracking a particular particle is required to obtain the diagrams.

A numerical code was created to track the particles and draw the diagrams. In the tracking process, the location of the fluid particle at the next time step is calculated based on the location at the current time step and its current velocity, and the values of its properties at various time step are recorded. At last, the diagrams are drawn by sequencing the property values in time. Figure 13 shows the T-s and p-v diagrams obtained by tracking a single fluid particle from it enters the channel to it leaves. The diagrams showed a clear Humphrey cycle, which is consistent with the expectation.

CHAPTER 3.   2D SIMULATION

Since the 1D code does not take into account the 2D effect, such as the complex channel shape, the leakage, gradual opening and closing of the ports and interaction between the channels, and to apply more sophisticated combustion model and calculate the power and efficiency, the 2D simulation is required for the design process.

3.1. Optimization Parameters

For the design in Figure 6, only the fresh air is drawn into the channels through the inlet. When the channel closes, the fuel is directly injected to the channel and then ignited. However, the mixing takes a lot of time and leaves short time for the combustion. Thus, to take advantage of the fast speed of the premixed combustion, the air-fuel mixture is supplied through the inlet which is called mixture inlet. In the configuration in Figure 6, the mixture will be ignited when the channel with the combustion products opens to the mixture inlet and the hot gas contacts the mixture. To prevent the backfire, another inlet is added before the mixture inlet. It is used for the supply of the fresh air only, to create a buffer layer between the burned gas and the mixture. This additional inlet is called air inlet. The configuration for the premixed combustion is shown in Figure 14, along with the geometric parameters that need to be determined yet. The geometric parameters contain the ports opening and closing angles, the inner and outer diameters of the rotor, the inclination angles of the ports walls and the blade angles. The symbols and their corresponding parameters are tabulated in Table 3-1.

Table 3-1: Symbols in Figure 14 and their meaning

AI_open	The opening angle of the air inlet	AI_closed	The closing angle of the air inlet
FI_open	The opening angle of the fuel inlet	FI_closed	The closing angle of the fuel inlet
EO_open	The opening angle of the outlet	EO_closed	The closing angle of the outlet
α_AI1	The right wall angle to the radial direction of the air inlet	α_AI2	The left wall angle to the radial direction of the air inlet
α_FI1	The right wall angle to the radial direction of the fuel inlet	α_FI2	The left wall angle to the radial direction of the fuel inlet
α_EO1	The right wall angle to the radial direction of the outlet	α_EO2	The left wall angle to the radial direction of the outlet
β_1	Inlet blade angle	β_2	Outlet blade angle

The other parameters are the rotational speed, disc cycles, the channel number and the ratio of the wall thickness to the channel width.

To create the channel wall in Gambit, a number of points on the wall are supposed to be created first, which requires the knowledge of the coordinates of these points. For the first try, a circular arc is chosen to be the channel shape (C1 shape). Its inlet blade angle is 100° and outlet angle is 10°. Both walls have the identical shape. A Matlab code was made to calculate the coordinates of the arc. Once the points are created, Gambit connects them using a NURBS curve.

3.2. Simulation methodology

For the simulations in this chapter, the ports timing is first obtained from the 1D code. Then the 2D simulations are performed using Fluent. Since the flow is unsteady, the transient solver is

used. Because the flow is mainly subsonic and the density-based solver is much slower than the pressure-based one, the pressure-based solver is used. The standard k-ε model is used for the turbulent flow. All walls are treated as adiabatic walls. Methane is chosen to be the fuel. The Laminar Finite-Rate model is chosen for the combustion simulation, where the Arrhenius rate is used for the reaction rate. Inlet Diffusion, Diffusion Energy Source, Full Multicomponent Diffusion and Thermal Diffusion were turned on. The constant pressure specific heat is calculated by the mixing law. The thermal conductivity is set to 0.0454 W/m-K and the viscosity 1.72×10^{-5} kg/m-s. The mass diffusivity and the thermal diffusion coefficient follow the kinetic theory. The spark ignition is simulated using a heater in the channel. In Figure 15 the rectangular is the heater. Each channel has one heater near the inlet. In the beginning, the boundary type of the rectangular is INTERIOR. When the channel rotates to a particular position, the heater is turned on by switching its boundary type to RADIATOR and its temperature is set to 2000 K and heat transfer coefficient is 10×10^{6} W/m^2-K. After 0.1 ms the heater is turned off by switching its boundary type back to INTERIOR. The time step size is set to 5×10^{-7} s. The working conditions are listed in Table 3-2.

Table 3-2: Working conditions for the baseline design

Air inlet total pressure (barg)	0	Fuel inlet total temperature (K)	300
Fuel inlet total pressure (barg)	0.1	Outlet pressure (barg)	0
Air inlet total temperature (K)	300	RPM	10000

3.3.Optimization for a Given Rotor

After 4 rotations, the operation reaches the periodic mode. For a given rotor, the geometry of the ports should be optimized for the best performance. The optimization is done in the following aspects:

1) The air inlet opening angle should be adjusted to make sure when the channel inlet is open, the pressure is below the ambient pressure, so that there is no backflow into the air inlet.

Figure 16(a) shows that when the channel is about to open to the air inlet, the pressure in the channel is higher than that in the air inlet. As a results, when it is open to the air inlet, some exhaust gas flows into the air inlet, as shown in Figure 16(b).

2) The wall angles of the ports should match with the blade angles to avoid the incidence loss.

In Figure 17(a) the incoming flow impacts the suction surface of the blade, which generates negative torque. The mismatching of the ports wall angles does not only decrease the torque generation, but harms the fuel loading. In Figure 17(b) the mixture concentrates only on the suction side of the blade so the channel cannot be fully filled. To prevent this, the inlet porting walls should incline more.

The outlet walls should be diverging because when the channel is just open, the direction of the absolute velocity at the channel outlet is opposite to the rotational direction and as channel rotates the absolute velocity gradually turns to the rotational direction, as shown in Figure 18.

3) The air inlet is wide enough to generate an air layer between the hot gas and the fresh

mixture.

4) The closing angles of the outlet port and the fuel inlet are proper for the channel to be filled up with the mixture without spill.

In Figure 17(b) the interface between the mixture and the air does not arrive at the outlet end of the channel when the outlet is closed, so the outlet port and the fuel inlet port should be enlarged.

5) No backfire should occur in the fuel inlet port.

Figure 19(a) shows that the hot burned gas is leaked into the following channels and the fuel inlet. As a result, the mixture in the following channels and the fuel inlet is ignited by the leakage. To prevent the backfire, the mixture needs to be ignited later so that the hot leakage can be absorbed by the following channels.

6) The combustion should be complete before the channel is open to the outlet port.

Figure 20 shows that in this design when the channel is open to the outlet port, there is still some unburned mixture left in the channel. To obtain a complete combustion, the spark location should be moved to the center of the channel and one set of the ports should be removed to ensure enough time for the combustion.

3.4. Baseline Design

After the geometry adjustment, the design was finalized. The final geometric parameters are listed in Table 3-3.

Table 3-3: Final geometric parameters of the baseline WDE

ID (cm)	10	AI_open (°)	72
OD (cm)	20	AI_close (°)	112
Gap (cm)	0.04	FI_open (°)	113
α _AI1 (°)	50	FI_close (°)	170
α _AI2 (°)	50	EO_open (°)	25
α _FI1 (°)	50	EO_close (°)	150
α _FI2 (°)	50	β1 (°)	100
α _EO1 (°)	-50	β4 (°)	10
α _EO2 (°)	20	Channel number	30
Height (cm)	2.5	Channel-to-wall ratio	4

Figure 21(a) shows that the air inlet effectively created an air layer between the hot gas and the fresh mixture. Figure 21(b) shows that the channel is filled up with the mixture when the channel is closed and the combustion is complete before the channel is open. Figure 21(c) shows that the relative velocity of the incoming flow follows the blade shape.

Table 3-4 shows the power and efficiency of the baseline engine in the second rotation. The power is calculated from the equation below

$$P = \tau_{\text{mean}} \omega \qquad (3.1)$$

where τ_{mean} is the mean torque during the chosen rotation and ω the angular velocity of the rotor. The efficiency is calculated from the equation below

$$\eta = \frac{P}{\dot{m}_{\text{mixture}} Y_{\text{CH4}} LHV_{\text{CH4}}} \qquad (3.2)$$

where $\dot{m}_{\mathrm{mixture}}$ is the average mass flow rate through the fuel inlet, Y_{CH4} is the mass fraction

of methane in the mixture and LHV_{CH4} is the lower heating value of methane. Theoretically, the

efficiency of Humphrey cycle without a pre-compression ratio of 1 is about 30% which is much

higher than the simulation. Thus, the energy loss should be examined to enhance the efficiency.

Table 3-4: Power and efficiency of the baseline design

Cycle	Power (kW)	Efficiency (%)
2	2.3712	1.23

Figure 22 shows the power history in the second rotation. Due to the unsteady nature, the

power fluctuates with time.

CHAPTER 4.   METHODS TO IMPROVE THE EFFICIENCY

4.1. Investigation into the Energy Usage

4.1.1.   1D Investigation

First, the particle tracking technique based on the 1D simulation was used to investigate the thermodynamic process that different fluid particles experience.

Figure 23 shows the T-s diagrams of 10 fluid particles that enter the channel at different time. From the figure it can be found that due to the unsteady nature of the flow, not all the exhaust gas particles leaves the channel at the ambient pressure, meaning that not all gas experiences a full Humphrey cycle. The gas that leaves first is at a high pressure and temperature, which is one of the sources of the energy lost and a low efficiency.

4.1.2.   2D Investigation

To verify the conclusion from the 1D investigation and take into account the 2D effect (channel curvature, gradual opening and closing of the channel), a further investigation was performed by 2D simulation.

Figure 24 shows the geometric configuration of the 2D simulation. To shorten the simulation time, only one channel is examined. The rotor has two sets of ports, so the channel experiences two cycles in each revolution. To eliminate the influence of the leakage, the gaps between the rotor and the stator were removed.

In this investigation only the thermodynamic characteristic is of interest and, a lot of

information from the combustion model is redundant, such as the flame propagation and the concentration of the species. Thus, a simpler model for the combustion can be adopted to accelerate the simulation. The species transport and reaction model was turned off and the air was chosen as the working material. Since the gradualness of the heat release by the combustion does not affect the power generation in this perfectly closed channel, the heat release can be modeled as a sudden rise in temperature and pressure. This was done by patching a high temperature and high pressure to the channel when it is fully closed. In this investigation, 2100 K was chosen as the patching temperature assuming that after the combustion the temperature in the channel increases to 2100 K. if the pressure is patched the arbitrarily, the density in the channel would change and consequently the mass is not conserved. To satisfy the mass conservation, the channel pressure should be patched according to the ideal gas law:

$$p_3 = \frac{2100\text{K}}{T_2} p_2 \qquad (4.1)$$

where T_2 and p_2 are the temperature and pressure before the patching and p_3 is the patching pressure.

As the thermodynamic analysis in section 1.3, the channel is taken as the control volume and the integral form of the energy equation Eq. (1.1) is applied.

The simulation ran for 6 working cycles (3 revolutions). The results are shown in Table 4-1. The net work done by the fluid to the channel was calculated by the following equation

$$W_{net} = \tau_{mean}\omega T_{cycle} \qquad (4.2)$$

The heat addition was obtained by

$$Q = E_3 - E_2 \qquad (4.3)$$

where E_2 is the internal energy in the channel before the patching and E_3 is that after the patching.

The cycle efficiency is

$$\eta = \frac{W_{net}}{Q} \qquad (4.4)$$

The kinetic energy is

$$k = H_{tot} - H \qquad (4.5)$$

The potential efficiency is

$$\eta_{potential} = \frac{W_{net} + \left(k_{out} - k_{in}\right)}{Q} \qquad (4.6)$$

The discrepancy of the energy equation is

$$\Delta_{energy} = \frac{Q - \left(H_{tot,out} - H_{tot,in} + W_{net}\right)}{Q} \times 100\% \qquad (4.7)$$

The discrepancy of the mass conservation equation is

$$\Delta_{mass} = \frac{\dot{m}_{in,mean} - \dot{m}_{out,mean}}{\dot{m}_{in,mean}} \times 100\% \qquad (4.8)$$

Table 4-1: Results of the 2D simulation for the analysis of the energy loss

Cycle	1	2	3	4	5	6
W_{net} (J)	0.8423	0.9905	0.9885	1.0014	1.0061	1.0061
Q (J)	23.9362	26.6363	26.3928	26.7855	26.8005	26.8326
η (%)	3.52	3.72	3.75	3.74	3.75	3.75
$H_{tot,in}$ (J)	0.2161	0.2115	0.1036	0.1037	0.1002	0.1000
H_{in} (J)	0.1089	0.0965	-0.0268	-0.0271	-0.0307	-0.0305
k_{in} (J)	0.1072	0.115	0.1304	0.1308	0.1309	0.1305
$H_{tot,out}$ (J)	-22.7106	-25.463	-25.2206	-25.5301	-25.5395	-25.5518
H_{out} (J)	-18.4599	-20.4108	-20.2095	-20.4261	-20.4228	-20.4309
K_{out} (J)	-4.2507	-5.0522	-5.0111	-5.1040	-5.1167	-5.1209
$\eta_{potential}$ (%)	20.83	22.25	22.24	22.31	22.36	22.35
Δ_{energy} (%)	2.50	1.48	1.09	1.34	1.32	1.40
$\dot{m}_{in,mean}$ (g/s)	8.269	8.3601	8.4485	8.4705	8.4127	8.3443
$\dot{m}_{out,mean}$ (g/s)	-7.4641	-8.4208	-8.3621	-8.4647	-8.4032	-8.3643
Δ_{mass} (%)	9.73	-0.726	1.02	0.0685	0.113	-0.240
$p_{compression}$ (Pa)	125400.7	124597.9	124567	124861	125140.6	125068.3
$p_{compression} / p_{in}$	1.126	1.119	1.119	1.122	1.124	1.123

For the sixth cycles, the discrepancy of the energy equation is 1.40% and that of the mass

conservation equation is -0.24%, which means that both of the energy and mass accumulated in the channel can be negligible and the working mode of the sixth cycle can be considered as a periodic mode.

In section 1.3, to achieve the efficiency of the Humphrey cycle, it was assumed that the incoming kinetic energy is equal to the outgoing one. However, in this simulation, the latter (5.1209 J) is much greater than the former (0.1305 J), meaning that a lot of energy was released to the ambience in the form of kinetic energy without being utilized. If the outgoing kinetic energy could be reused, the efficiency would increase from 3.75 % to 22.35 %.

Moreover, in the sixth cycle after the patching, the mean pressure in the channel is 805654.83 Pa. In the ideal Humphrey cycle, when the gas expanded isentropically from $p_3 = 805654.83$ Pa and $T_3 = 2100$ K to $p_4 = 1$ atm, the temperature should be lowered down to $T_4 = 1162.64$ K calculated from the isentropic relationship

$$\frac{T_4}{T_3} = \left(\frac{p_4}{p_3} \right)^{\frac{\gamma-1}{\gamma}}$$
(4.9)

Thus, the corresponding specific enthalpy is

$$h_4 = c_p \left(T_4 - T_{ref} \right) = 1006.43 \times \left(1162.64 - 298.15 \right) = 869699 \left(\text{J/kg} \right)$$
(4.10)

From Figure 25 it can be seen that the specific enthalpy at the outlet of the channel gradually drops down after the channel is open, and it is above the theoretical value in the first half of the expansion. Theoretically, during the expansion process (0.0129435 s to 0.0133225 s), the outgoing enthalpy should have been

$$H_4 = \dot{m}h_4\Delta t = 0.0365999 \times (0.0133225 - 0.0129435) \times 869699 = 13.8071(\text{J}) \qquad (4.11)$$

However, from the simulation, this value is 16.3922 J which is higher than the theoretical one, meaning that not all the gas is fully expanded. In fact, from the Figure 25 it can be seen that the gas leaving first is under-expanded and that leaving later is over-expanded. The enthalpy analysis shows that the gas is under-expanded in terms of the net effect.

Based on Eq. (4.9) for the Humphrey cycle with the precompression ratio of 1 (Lenoir cycle), if the temperature and pressure after the heat addition are $T_3 = 2100$ K and $p_3 = 7$ atm, the temperature after the expansion is $T_4 = 1205.7$ K. The thermal efficiency of an air-standard can be calculated as follows:

$$\eta = 1 - \gamma\frac{T_4 - T_1}{T_3 - T_2} = 1 - 1.4 \times \frac{1205.7 - 300}{2100 - 300} = 29.6\% \qquad (4.12)$$

In sum, there are two sources of the energy loss in this simulation. One is the difference between the outgoing kinetic energy and the incoming one, and the other is the under-expansion of the gas. Thus, the method to improve the efficiency would be further expanding the gas in the channel, reducing the outgoing kinetic energy, increasing the incoming kinetic energy and reusing the energy from the exhaust gas.

4.2. Investigation into the Channel Shape

To improve the efficiency, more energy should be extracted from the rotor. To exploit the potential of energy extraction from the channel, more advanced channel shapes need to be explored.

4.2.1. Torque Generation Mechanism for Unsteady Flow

Although researchers intended to use the curved channel in wave engines to generate power, the principle of the power generation has not been explained clearly. Since the WDE is an unsteady flow device, the power generation principle should be distinguished from the traditional steady flow turbine.

For a steady flow turbomachinery, when a fluid particle passes through a blade passage, it is subject to the centripetal force provided by the pressure gradient pointing to the center of blade curvature. The pressure gradient increases with the curvature, the velocity and the density. One way to increase the pressure gradient is to increase the curvature. Based on this idea the C1 channel is modified to the C2 shape to obtain a higher efficiency. The curve of C2 is obtained by increasing the inlet blade angle from 100° to 150° while keeping the outlet blade angle of 10°. Both walls are of the identical shape and the volume of the C2 channel is identical to that of the C1 channel. The geometry of the C2 channel is shown in Figure 26.

To compare their performance in a steady flow, two steady state simulations were done for them respectively. In the simulations, the gauge total pressure at the inlet is set to 0.1 bar and that at the outlet is 0.

Figure 27 shows the pressure contour in the tested channels. Due to the curvature, the pressure on the pressure side of the channel is higher than that on the suction side in both cases. For the C1 channel the flow generates 7.09 N·m of torque, and the torque on the C2 channel is 14.59 N·m. The torque of C2 channel is approximately twice as much as the C1 channel, which is consistent with the principle above. However, since the WDE operates in an unsteady flow, the

principle for the steady flow blade design might not be valid. Thus, the performance of power generation in unsteady flow must be examined.

For a steady flow turbine, the torque on the blades does not vary with time. In contrast, the torque on the channel walls of a WDE fluctuates a lot. The moment coefficient history in the sixth cycle of the energy loss simulation is shown in Figure 28, where the moment coefficient

$$C_m = \frac{\tau}{\frac{1}{2}\rho_{ref}v_{ref}^2 A_{ref}L_{ref}} \tag{4.12}$$

is a non-dimensional torque.

In the torque history diagram, the area between the curve and the time axis shows the energy extracted from the flow. It can be seen that the major extraction is done in the expansion process. The energy extracted in each process is tabulated in Table 4-2. From the table it is noticed that the major power is generated in the expansion process when the outlet is open and the inlet is closed. The power generated in the other processes is negligible. Thus, in this section the energy extraction performance of various channel shapes in unsteady flow is investigated only for the expansion process.

Table 4-2: Work generated in each process in the sixth cycle

	Expansion	Scavenging	Compression	Combustion
Starting time (s)	0.0159435	0.016322	0.0177695	-
Ending time (s)	0.016322	0.0177695	0.017915	-
Work generated (J)	1.051	-0.02726	-0.02078	0.002889
Contribution to total work (%)	104.5	-2.709	-2.065	0.2872

Several channel shapes were tested. In each case, the computation domain consists of a rotating channel and a stationary outlet port. In the beginning of the simulation the channel was fully closed with the air at 1 atm and 300K. Then the channel temperature is patched to 2100 K and the pressure is patched based on Eq. (4.1). The simulation proceeds as the channel rotates at 10,000 RPM. Finally, the simulation stops when the pressure at the inlet wall of the channel decreases to the ambient pressure.

To compare various channel shapes, the C1 channel was chosen as the baseline shape. The geometry of the C1 channel is shown in Figure 29.

The work done by the flow to the channel wall is calculated using Eq. (4.2). The heat addition is the internal energy increase due to the patching. The efficiency is calculated by dividing the energy generated by the heat addition. The tests for the C1 channel and C2 channel were done, and the results are shown in Table 4-3. However, the efficiency of C2 is not higher than the C1 channel as in the steady flow tests. Thus, the unsteady factors must play an important role in the energy extraction and the traditional blade design for steady flow does not apply.

Table 4-3: Results of the unsteady simulations for C1 and C2 channel

Shape	C1	C2
Duration (ms)	0.3835	0.3445
Efficiency (%)	3.38	3.13

To obtain a guidance to improve the channel shape, the power generation principle should

be investigated first.

The source of the torque on the channel wall is the pressure and the viscous force exerted by the fluid. However, compared to the pressure, the effect of the viscous force is negligible. Thus, it is only necessary to investigate the pressure in the channel. The pressure on the pressure side generates positive torque, while the pressure on the suction side generates negative torque. So the net torque depends on the pressure differential.

Previous research has shown that the front of the acoustic/shock wave propagating through a curved channel is approximately perpendicular to the channel wall.

The similar phenomenon has been observed in the C1 channel. As shown in Figure 31, as the channel gradually opens, the expansion wave originates at the trailing edge of the upper wall, and then the wave front adjusts to be perpendicular to the channel walls.

During propagating towards the inlet, the wave front is always perpendicular to the walls, shown in Figure 32.

While the reflecting wave interferes with the incident wave, the front is convex to the inlet wall, shown in Figure 33.

The torque on the channel walls is generated by the pressure distribution. For simplicity, a rotating straight channel was tested to explain the principle of torque generation by the expansion wave. In the beginning of the simulation, the channel contains the gas at 7 bar and 2100 K, and then the outlet suddenly opens to the ambience. Figure 34 shows the pressure contours during the expansion wave travels towards the inlet end of the channel.

Figure 34 shows the expansion wave propagates towards the inlet end of the channel,

causing a pressure gradient after its head. In this analysis, a positive pressure gradient is defined as the pressure decrease in the direction from the inlet to the outlet. If the pressure decreases in the opposite direction, the pressure gradient is negative. It can be found that the isobaric lines are perpendicular to the channel walls. Two points on the channel walls, point a and point b, are used for analysis. They are the intersections of the circumferential line and the two walls, i.e., they are at the same radius. Since the walls are not radial, each isobaric line has an angle with respect to the circumferential direction. Due to this angle and the pressure distribution, there is a pressure difference between point a and point b. In this case where the inlet angle of the channel wall is smaller than 90°, the pressure at point a is higher than that at point b. In the same way, all points on the upper wall are at higher pressure than their corresponding points on the bottom wall, which generates positive net torque. If the blade angle is greater than 90°, the net torque would be negative. A more general principle of the torque generation can be expressed by Table 4-4.

Table 4-4: General principle of torque generation by travelling expansion wave

	Blade angle < 90°	Blade angle > 90°
+ pressure gradient	+	-
- pressure gradient	-	+

The result that the C2 channel has a lower efficiency than C1 channel can be explained by this theory. Figure 35 shows the pressure contours of the C2 channels. It can be observed that near the outlet the blade angle is smaller than 90° and near the inlet the blade angle is greater

than 90°. Consequently, the torque generated by the part near the outlet is positive, while that near the inlet is negative. According to the positive efficiency, the net torque it positive. Near the inlet, the blade angle of the C2 channel is greater than that of the C1 channel, so the angle between the isobaric line near the inlet and the circumferential direction is greater in the C2 channel, which causes greater negative torque than the C1 channel.

To further justify this principle, two new channel shapes were proposed. The first one is a C shape channel with 70° of the inlet blade angle and 10° of the outlet one, which is shown in Figure 36.

The second one consists of two parts - a straight line and a circular arc, and the straight line is tangent to the arc. This shape is named J shape. Figure 37 shows two channels of the J shape. Both of them have the inlet blade angle of 100° and outlet blade angle of 10°. For J1 channel, the radius of the tangent point of the straight portion and the arc is 7 cm. for J2 channel, the tangent point is at 8 cm of radius. If the length of the straight portion reduces to 0 cm, the J shape becomes the C shape.

The results of these three channels are tabulated in Table 4-5. Among C1, J1 and J2 channels, J2 has the lowest efficiency while C1 has the highest one because J2 has the longest straight portion where the negative torque is generated, while the C1 has the smallest. Since the blade angle is smaller than 90° everywhere for C3 channel, the torque is always positive. Thus, C3 has the highest efficiency among all channels that have been tested so far.

Table 4-5: Results of the single channel simulations for C3, J1 and J2 channels

Shape	C3	J1	J2
Duration (ms)	0.4515	0.3290	0.2935
Efficiency (%)	3.89	2.94	2.33

4.2.2. Effect of the Outlet Opening

If we plot the relationship between the efficiency and the expansion duration for the tests in the previous section (see Figure 38), it can be found that the efficiency increases with the expansion duration.

One important geometric parameter that influences the expansion duration is the outlet opening, which is defined as the smallest distance from the trailing edge of the upper wall to the surface of the lower wall, shown in Figure 39.

From the relationship between the expansion duration and the outlet opening (Figure 40), it can be found that the expansion process is slowed down by the smaller outlet opening. Combining with Figure 38, the smaller outlet opening gives higher efficiency. Based on this idea, the J2 and C3 channels are modified to have smaller outlet openings.

The modification method is to rearrange the curvature of the upper wall while maintaining the outlet blade angle. The geometries of the modified channels (MJ2 and MC3) are shown in Figure 41. Their outlet openings, expansion durations and efficiencies are listed in Table 4-6. From the results, it can be seen that both of them have higher efficiency than the channel tested in the previous section and their outlet openings are smaller than those channels, which justifies

the relationship between the outlet opening and the efficiency. However, even if the MC3

channel has a bigger outlet opening and shorter expansion duration than the MJ2 channel, its

efficiency is still higher, which can be explained by the torque generation principle describe in

the previous section.

Table 4-6: Outlet openings, expansion durations and efficiencies of the single channel simulations for J2, C3, MJ2 and MC3 channels

Shape	J2	MJ2	C3	MC3
Outlet opening (cm)	0.7971	0.1500	0.4350	0.1515
Expansion duration (ms)	0.2935	1.5947	0.4515	1.275
Efficiency (%)	2.33	4.77	3.89	5.12

For all channels that have been tested so far, both walls have the identical inlet blade angle

and the identical outlet blade angle. A convergent channel with two different shape walls was

tested additionally. The geometry is shown in Figure 42, and the blade angles are listed in Table

4-7.

Table 4-7: Blade angles of the convergent channel

	Upper wall	Lower wall
Inlet angle (°)	75	90
Outlet angle (°)	10	10

Its outlet opening, expansion duration and efficiency are listed in Table 4-8. Due to the

bigger outlet opening, the expansion duration of the convergent channel is shorter than those of MJ2 and MC3. However, the efficiency is higher than MJ2, which is because the inlet blade angles are smaller than those of MJ2. The efficiency is lower than MC3 is resulted from that the blade angles and the outlet opening are bigger than those of MC3.

Table 4-8: Results of the single channel simulations for the convergent channel

Outlet opening (cm)	Expansion duration (ms)	Efficiency (%)
0.2338	0.7860	4.82

Comparing the torque histories of all tested channels (see Figure 43), it can be found that for the short expansion the torque has only one peak, while for the long expansion the torque has multiple peaks. As the expansion gets longer, the torque oscillation becomes clearer.

The torque oscillation can be explained by the variation of the pressure gradient with time. Take the MC3 channel for example. When the channel outlet opens, an incident expansion wave propagates into the channel, causing the positive pressure gradient behind the wave front and accelerating the mass flow out of the channel. As the incident expansion wave propagates towards the inlet end, the area with the positive pressure gradient grows (Figure). Since the blade angle is smaller than 90°, according to the torque generation mechanism, the positive torque increases in this duration. The torque can be illustrated directly by the profiles of pressure as a function of radius on the pressure surface and the suction surface (Figure). In the profile

plots, the area under each curve is the tangential component of the force on the corresponding surface and the area between the black curve and the red one gives the net tangential force on the channel (shaded area). The force is positive in the regions where the black curve is above the red curve and negative where the black curve is below the red one. Figure   shows that the region of positive force grows as the incident expansion wave propagates. When the head of the expansion wave arrives at the inlet end, the positive torque is generated in the entire channel and reaches the first peak. Therefore, the propagation of the incident expansion wave is the main reason for the first rise of the torque.

Besides the propagation of the incident expansion wave, the gradual opening is another reason. Figure 45 shows that there is a relatively high pressure region (the circled area in the pressure contour) near the trailing edge of the suction surface, and the gauge pressure decreases to the ambient pressure at $r = 0.099$ cm and then increases to 2.5 bar, which is because the bottom corner of the channel outlet is still closed. Compared with the imaginary scenario where the pressure remains ambient pressure beyond $r = 0.099$ cm, the net force is smaller (the shaded area in the bottom diagram) in the real case and hence a smaller positive torque. This is the undesirable effect of the gradual opening. To reduce this effect, the opening time should be shortened by either increasing the blade tip speed or decreasing the channel circumferential opening (the circumferential length of the channel outlet).

Figure   shows that when the channel outlet is fully open, the high pressure region disappears and the gauge pressure near the trailing edge of the suction surface decreases to -1 bar. From Figure   one can see that the flow is supersonic outside the channel opening. When the

52

supersonic flow sees the trailing edge of the channel bent away from the flow, a Prandtl-Meyer expansion wave is generated on the bent edge further decreasing the pressure. Compared with the scenario where the pressure remained atmospheric in the region where the Prandtl-Meyer expansion wave is located, the Prandtl-Meyer expansion wave generates additional force (shaded area in the middle diagram) and hence an additional positive torque. This is the benefit of the supersonic outflow and the curved trailing edge. Thus, the shrinking of the high pressure region as the channel outlet opens is the minor reason for the first rise of torque.

Once reaching the inlet end, the incident expansion wave reflects. The reflected expansion wave further decreases the pressure behind its head and decelerates the mass flow. As propagating towards the outlet, the reflected wave interferes with the rest of the incident expansion wave, forming a nonsimple region. In this case and other the long expansion cases, such as the convergent channel and MJ2, the pressure gradient is negative (Figure 47) in the nonsimple region, and the peak pressure occurs at the interface between the simple and nonsimple regions. According to the torque generation principle, the negative pressure gradient with the blade angle smaller than 90° generates negative torque. In the short expansion cases, although the negative pressure gradient is not observed, the positive pressure gradient in the nonsimple region is very small. As the reflected expansion wave propagates towards the outlet, the nonsimple region grows. Thus, during this process the net torque on the channel walls decreases. Due to the fact that the flow is choked at the outlet, the tail of the incident expansion wave cannot propagate into the channel. Therefore, when the head of the reflected wave arrives at the outlet, the nonsimple region is all over the channel. However, near the outlet of the channel,

the positive pressure gradient caused by the incident expansion wave is greater than the negative pressure gradient caused by the reflected expansion wave, the net pressure gradient is still positive. Therefore, the net torque on the walls is still positive.

As the reflected expansion wave propagates, the mass velocity in the nonsimple region decreases to zero and then to negative values due to the inertia. In other word, the gas flows backward (Figure 48). When the backflow impacts on the inlet end wall, a compression wave is generated at the inlet end. The compression wave and the incident expansion wave cause a positive pressure gradient behind the compression wave, shown in Figure 49. As the compression wave propagates towards the outlet, the positive pressure gradient zone grows, and consequently the positive torque increases near the inlet end. Thus, the net torque in the whole channel increases. Eventually, the pressure gradient becomes positive everywhere in the channel and torque oscillation cycle goes back to the state when the incident expansion wave propagates towards the inlet.

The process described above repeats several times, and the positive and negative pressure gradients occur near the inlet of the channel alternately, causing the torque oscillation. The torque oscillation phenomenon is very obvious in MJ2, MC3 and the convergent channels; in the case of C3 channel, the torque oscillates less than the three long expansion cases but more than the other short expansion cases. Although the smaller channel opening prolongs the expansion process, the reflected expansion wave has a negative effect on the torque generation.

Another conclusion can be drawn by the observation of the pressure profiles. In all processes, the maximum tangential force (the area between the black curve and the red one in

Figure , Figure 47 and Figure 49) occurs near the outlet of the channel. This force generates greater torque when the channel outlet is at the outer radius than at the inner radius due to a longer force arm at the outer radius. Thus, the channel outlet should be at the outer radius so that the force can be made used of more efficiently.

4.3.Implementation of the New Shape

Although the longer expansion gives the higher efficiency, it has some disadvantages. For example, at a certain rotational speed, the total time for the expansion, scavenging, compression and combustion is fixed. The long expansion channels have smaller outlet openings, which causes a longer scavenging. Since both the expansion and scavenging times are longer, the time left for the combustion is shorter and the combustion may not be complete. In this section, the convergent channel is chosen to be implemented on a WDE, for it has a high efficiency and a relatively shorter expansion.

To compare with the convergent channel engine, a baseline simulation was performed first. The geometry of the baseline engine was taken to be tested. However, in this simulation the combustion behavior is not of interest, but the aerodynamic performance of the engine. Thus, the species transport and reaction model were turned off and the patching method was used for combustion modeling as in section 4.1.2. To reduce the influence of leakage, the channel is patched just before it opens to the outlet port as shown in Figure 50.

The histories of the torque of the first three cycles (Figure) show that the third cycle reaches the periodic operation mode. Table 4-9 lists the power and efficiency in the third cycle.

Table 4-9: Results of the simulation with patching method for the baseline design

Cycle	Power (kW)	Efficiency (%)
3	1.6476	2.21

The geometry of the WDE with the convergent channels is shown in Figure 52. The histories of torque (Figure 53) show that the second cycle reaches the periodic mode. Comparison between Table 4-9 and Table 4-10 shows that the efficiency increases by 81%.

Table 4-10: Results of the WDE with the convergent channels

Cycle	Power (kW)	Efficiency (%)
2	2.4803	3.96

4.4. Effect of the Peak Pressure

4.4.1. 1D Investigation

To investigate the reason for the under-expansion of the exhaust, two cases were tested using the 1D code. The first one is the test case in section 2.3.

Figure 54 shows that the outflow is choked, so the tail of the expansion wave cannot propagate into the channel. The flow is under-expanded.

In the second case, the initial pressure is reduced to 3 bar. Figure 55 shows that in this case

the outflow became subsonic, and the entire expansion wave was confined in the channel. Thus,

reducing the pressure in the channel after the combustion leads to a way to fully expand the gas.

4.4.2. 2D Investigation

To justify the result from the 1D simulation above, two 2D cases were tested using the geometry

of C shape 3. Their peak pressures were 5 atm and 4 atm respectively. Table 4-11 lists the results.

The results show that the efficiency increases as the peak pressure decreases, which is consistent

with the 1D simulation. However, as the peak pressure decreases, the power decreases as well.

Thus, the determination of the peak pressure depends on the priority of the power and efficiency.

Table 4-11: Results of the initial pressure tests

Peak pressure (atm)	7	5	4
Power (kW)	2.0626	1.7403	1.4567
Efficiency (%)	3.89	4.66	5.08

4.4.3. Full Engine Test

C2 channel was used on the full engine test. Figure 56 shows the geometry of the engine. In this

simulation the patching temperature is 2100 K and the pressure was patched accordingly. The

results of the second rotation are shown in Table 4-12.

Table 4-12: Results of the simulation with 2100 K patching temperature for the WDE with C3 channels

Cycle	Power (kW)	Efficiency (%)
2	2.9905	1.94

Then the simulation was re-run with 1200 K of patching temperature and the results the second rotation are shown in Table 4-13. Compared to the previous simulation, the case with a lower pressure and temperature after combustion has a higher efficiency, which is consistent with the 1D and 2D investigation. In practice, the lower combustion pressure can be achieved by filling a lean mixture or partially filling the channel.

Table 4-13: Results of the simulation with 1200 K patching temperature for the WDE with C3 channels

Cycle	Power (kW)	Efficiency (%)
2	1.7735	2.56

4.5. The Effect of the Blade Tip Speed

4.5.1. Single Channel Investigation

According to the energy loss analysis, the most important loss is the significant outgoing kinetic energy. If the rotor is stationary, when the channel opens to the ambience, the burned gas exhausts at a very high velocity due to the pressure difference and all energy is released to the

ambience without being used. As the rotor accelerates, the blade tip speed increases. The relative

velocity of the exhaust gas mainly depends on the pressure ratio of the gas and the ambience. In

the case shown in Figure 57, under the condition that the tangential relative velocity $\vec{w}_\theta$ is to

the opposite of the tip speed $\vec{U}$ and the magnitude of the tip speed U is smaller than that of the

tangential relative velocity w_θ, the magnitude of the tangential absolute velocity c_θ decreases as

the tip speed increases. Since the radial absolute velocity c_r is the radial relative velocity w_r

which does not change with the tip speed, the magnitude of the absolute velocity c decreases as

the tip speed increases. Therefore, the outgoing kinetic energy decreases. For the expansion

process when the inlet is closed, there is no energy coming in, and the outgoing enthalpy depends

only on the pressure ratio and does not change with the tip speed, so a smaller outgoing kinetic

energy means a higher energy extraction and hence a higher efficiency. However, if the

magnitude of the tip speed is greater than that of the tangential relative velocity, the tangential

absolute velocity increases with the tip speed and hence an increasing kinetic energy. Thus, the

performance of the energy extraction increases up to a maximum and then decreases as the tip

speed increases.

Besides, as discussed in section 0, increasing the blade tip speed reduces the undesirable

effect of the gradual opening and benefits the torque generation.

There are two ways to increase the tip speed – increasing the outer diameter and increasing

the rotational speed.

A series of single channel simulations were performed to justify the relationship between

the efficiency and the rotor dimension. The convergent channel was taken for the test. In this test,

the radial distance between the outlet and the inlet remained 5 cm in each case, and three outer radii were tested – 10 cm, 15 cm and 20 cm. Table 4-14 and Figure 58 show that both power and efficiency increase with the channel diameter within the tested range.

Table 4-14: Results of the rotor dimension tests

OR (cm)	10	15	20
IR (cm)	5	10	15
Power (kW)	1.3506	2.1152	2.7754
Efficiency (%)	4.82	7.14	10.32

The C3 channel was taken to examine the relationship between the efficiency and the rotational speed. In this test, five speeds - 1000 RPM, 5000 RPM, 10000RPM, 15000 RPM and 20000 RPM - were tested. The initial temperature and pressure are identical to those in section 4.2. Their results of five rotational speeds are listed in Table 4-15. Figure 59 shows that both power and efficiency increase with the rotational speed within the tested range. Another advantage of high rotational speed is that the opening and closing of the channel is faster, which is favorable to the generation of expansion wave and hammer shock wave.

Table 4-15: Results of the rotational speed tests

RPM	1000	5000	10000	15000	20000
Duration (ms)	0.7305	0.479	0.4515	0.4416	0.4365
Power (kW)	0.0307	0.7642	2.0626	3.5081	4.7749
Efficiency (%)	0.0937	1.53	3.89	6.47	8.71

To adopt a higher rotational speed the channel dimension should be adapted accordingly. The higher rotational speed shortens the time for combustion, which is unfavorable for the completeness of the combustion. For example, if the rotational speed is doubled, the optimistic case is that all times for expansion, scavenging, compression and combustion are halved. However, this is not the real case. Table 4-15 shows that the expansion duration decreases as the rotational speed increases due to the increasing centrifugal force, but the variation is insignificant. From 5000 RPM to 10000 RPM, the rotational speed increases 4 times but the duration decreases only 8.87%. The duration of 1000 RPM is irregularly long because of the gradualness of the outlet opening. Thus, it is reasonable to assume that the wave time (the expansion and compression durations) does not change with the rotational speed. To examine the variation of the scavenging time with the rotational speed, a 1D simulation was performed. The geometry and working conditions are the same as the test case shown in Table 2-1, only with the rotational speed changed to 20000 RPM. From Table 4-16, the scavenging time can be calculated. The time for 10000 RPM is $4.3292 - 1.3340 = 2.9952 \ (\times 10^{-4} \text{s})$, and that for 20000 RPM is $4.0657 - 1.3111 = 2.7546 \ (\times 10^{-4} \text{s})$ which is 8.03 % less than $2.9952 \ (\times 10^{-4} \text{s})$. Consequently, for a doubled

rotational speed the time for combustion is less than half of the original time. To solve this problem, the channel length should be halved so that the wave time and scavenging time can be halved and the time required by complete combustion is halved as well. Therefore, for a given blade tip speed, a rotor with the original outer diameter but half length and double rotational speed can use the same ports timing as the rotor with the original length and rotational speed but a doubled outer diameter. In other words, the dimension of the engine can be scaled without changing the ports timing and the rotational speed should be scaled accordingly. The effect of the scaling on the efficiency will be examined in section 4.6.4.

Table 4-16: Comparison of the ports timing of different rotational speeds

RPM	$t_{IO}(\times 10^{-4}s)$	$t_{OC}(\times 10^{-4}s)$	$t_{IC}(\times 10^{-4}s)$
10000	1.3340	4.3292	6.0538
20000	1.3111	4.0657	5.8655

4.5.2. Full Engine Investigation

To examine if this principle applies for the full engine, a WDE with 20 cm ID and 30 cm OD was created. Figure 60 shows its geometry. Since its perimeter is longer, it can accommodate more channels. In this design there are 30 channels on the rotor.

Comparison between Table 4-17 and Table 4-10 shows clearly that the efficiency increases by 26.5% by enlarging the rotor.

Table 4-17: Results of the WDE with 30 cm OD

Cycle	Power (kW)	Efficiency (%)
2	2.8632	5.01

4.6. Reuse of the Energy from the Exhaust Gas

4.6.1.   Return Channel

Since a significant amount of energy in the exhaust gas is not fully used, the efficiency of the baseline design is much lower than the theoretical value of Humphrey cycle. If the exhaust gas can be inducted back to the channel, some energy from the gas can generate additional power. Adding a return channel serves this purpose.

Figure 61 shows the configuration of a WDE with a return channel. Table 4-18 lists its power and efficiency. Comparing Table 4-10 with Table 4-18, the results show that the efficiency increases by 56.1% by adding a return channel.

Table 4-18: Results of the WDE with a return channel

Cycle	Power (kW)	Efficiency (%)
2	3.9943	6.18

4.6.2. Two-Stage Rotor

When the gas passes through the long return channel, pressure loss occurs in this process. It would be beneficial if the exhaust gas can generate power immediately after leaving the channel. Like a conventional gas turbine, adding a second rotor outside the engine can meet this requirement.

Figure 62 shows the configuration of a two-stage engine. In this design several guide vanes were added to the exit port of the first stage (inner rotor) to deflect the exhaust gas to the second stage (outer rotor). The two rotors are connected to the same shaft. The combustion takes place in the first stage and the second stage is used for energy extraction only.

When the inlet of the turbine blade passage opens to the outlet of the guide vane passage, a compression wave propagates into the turbine passage. Thus, the torque generation mechanism of the external turbine is similar to that of the inner rotor, and 70° was used for the inlet blade angle and 10° for the outlet angle. The power and efficiency of the second rotation are listed in Table 4-19. Comparison between Table 4-10 and Table 4-19 shows that the efficiency increases by 106.8%. Comparing Table 4-18 with Table 4-19, one can find that the efficiency increases by 32.5%. Thus, using an external turbine is a more effective way to improve the efficiency.

Table 4-19: Results of the two-stage engine

Cycle	Power (kW)	Efficiency (%)
2	5.2240	8.19

4.6.3. Configuration of the Guide Vanes and the Turbine Blades

Since the two-stage engine has the highest efficiency so far, more attention is paid to the development of this configuration.

Figure 63 shows that when the blade passage (passage A) first opens to the guide vane passage the compression wave propagates into the blade passage and the pressure gradient is positive. However, as the blade passage (passage B) rotates, its inlet is exposed to a lower pressure region and an expansion wave propagates into the blade passage causing a negative pressure gradient near the inlet generating negative torque. As the blade rotates, the pressure gradient near the inlet turns positive and negative alternately. Thus, the inlet angle smaller than 90° is not always beneficial. Since the blade passages have through-flow in them when they generate torque, the operation of the blades is closer to that of a conventional turbine. Therefore, the conventional turbine geometry may help improve the efficiency.

Figure 64 shows that due to the leakage jet the flow is in the middle of the vane passage and in the next four vane passages, the flow is attached to the pressure surface of the passage and separate from the suction surface.

Based on the above analysis, the guide vanes and the external turbine were modified (second generation engine). The geometry is shown in Figure 65. The inlet blade angle of the turbine was increased to be bigger than 90°, and the blade length was shortened to increase the curvature. More guide vanes were added to narrow down the width of the guide vane passage to avoid the flow separation and vortices. The outlet opening of the guide vane passage was made smaller than the inlet opening to form a nozzle, so that the under-expanded exhaust gas can be

further expanded to the ambient pressure. The inlet and outlet of the turbine are expected to be at

the ambient pressure, and the kinetic energy change provides the power generation. The results

are listed in Table 4-20. It can be seen that the efficiency is 30.7% higher than the original

two-stage design.

Table 4-20: Results of the two-stage engine with a traditional external turbine

Cycle	Power (kW)	Efficiency (%)
2	8.2902	11.01

Figure 66 shows that stationary shock waves are generated when the outlet of the guide

vane passage and the inlet of the blade passage form a converging-diverging nozzle, which

causes a negative pressure gradient near the blade inlet generating positive torque.

Figure 67 shows that when an inner channel (channel A) opens to a guide vane passage

(passage B), the flow follows the guide vanes. However, when the channel wall (wall C) starts

passing the vane passage (passage D), the flow separates from the pressure surface of the passage;

when the inlet of a vane passage (passage E) is closed, the flow stops in the passage. Thus, the

flow is not continuous in the guide vane passages.

4.6.4. Scalability

Section 4.5.1 states that the engine can be scaled without changing the ports timing and the

rotational speed should be scaled accordingly. In this section the second generation engine was

scaled down to 2/3 and the rotational speed was increased to 1.5 times. The results are listed in

Table 4-21. Comparing Table 4-21 and Table 4-20 it can be found that the efficiency maintains

and the power reduces to 2/3, which proves the scalability of the engine.

Table 4-21: Results of the scaled engine

Cycle	Power (kW)	Efficiency (%)
2	5.4813	10.92

CHAPTER 5. METHODS TO PREVENT BACKFIRE

For a WDE, not only does the leakage cause the energy loss, but also jeopardizes the safe operation. Due to the pressure difference between the channels, the burned gas leaks from the high pressure channels to the low pressure channels and the inlet ports. If the speed of the leakage jet is too high, the jet will block the air from the air inlet and consequently destroy the construction of the buffer layer between the burned gas and the fresh mixture and increase the probability of the backfire. Besides, even though the gap is very small (0.3 mm) and the flame cannot propagate through the gap, the leakage jet brings radicals and hot gas into the fuel inlet and causes backfire. Thus, it is necessary to explore the method to avoid the leakage. This is necessary when the premixed mixture is supplied from the fuel inlet. If only air goes through the inlet port and the fuel is directly injected to the channels, backfire would not happen.

5.1. Simulation Methodology

Since the leakage flow is driven by the pressure difference, to provide a fare comparison the heat addition was modeled by patch a high pressure and the according temperature to the channel where the heat is released. In this analysis, 9 bar of the gauge pressure was used for the pressure patching, and the patching temperature was calculated by the following equation

$$T_3 = \frac{\left(9\times10^5\,\text{Pa} + 101325.1\text{Pa}\right)T_2}{p_2} \tag{5.1}$$

The patching pressure is the same for all cases tested in this chapter and the working conditions are the same in all cases in this chapter, listed in Table 5-1. The position of the patching channel

is shown in Figure 68. In the previous simulations, the channel is patched when its outlet is just about to open so that the leakage would not develop much. In this analysis, the channel is patched $1.5T_{ch}$ before its outlet opens to give the leakage sufficient time to develop. However, this patching method has some disadvantages. As the operation proceeds, the hot leakage gas will concentrate on the outlet end of the suction surface. This gas has a very high temperature but is at the same pressure as the rest area of the channel. After the pressure patching, the pressure rise and the temperature rise are the same all over the channel, and the temperature in the hot leakage area reaches a very high level. And then this hot gas leaks to the following channel. After the next patching, its temperature gets higher again. As this process repeats, the temperature of the hot leakage gas gets higher and higher. Its thermodynamic process is shown in Figure 69. For the simulations, the temperature is limited under 5000 K, meaning that whenever the local temperature gets above 5000 K, Fluent forces the temperature to be 5000 K while keeps other variables unchanged. In this way, the temperature is reduced but the pressure does not change, and consequently the density increases in this region, meaning that some additional mass is added to this region. Fortunately, the temperature limiting occurs only near the outlet end of the suction surface, so it does not affect the leakage in the inner gap. However, the efficiency is affected.

Table 5-1: Working conditions of the simulations in CHAPTER 5

$P_{tot,AI}$ (barg)	0.1	$P_{tot,FI}$ (barg)	0.1	P_{GO} (barg)	0	P_{TO} (barg)	0	RPM	7500
$T_{tot,AI}$ (K)	300	$T_{tot,FI}$ (K)	300	T_{GO} (K)	300	T_{TO} (K)	300		

Besides the pressure patching method, the temperature method was used and 2400 K was used for the temperature patching. For the temperature patching method, no additional mass is added. However, the temperature in the channel just before the patching is different in different cases, so after the patching the pressure is different for different cases, which brings difficulty to the comparison.

The third heat addition model is to specify a volumetric heat release rate to an area in the channel by turning on the energy source term for a time period. The area is shown in Figure 70. This area should not overlap with the hot leakage area near the end of the suction surface. Otherwise due to the heat release in the hot leakage area, its temperature would go higher and higher as in the pressure patching method. Moreover, the time for the heat release should be very short. Since the heat release area is open, during the heat release the mass continues flowing out of the area, causing a mass reduction in this area. Due to the constant heat release rate, the specific heat released in this area increases with time and hence an increasing temperature rise per time step. Eventually, the peak temperature will reach an unrealistic high value. In this

analysis, the heat release time was set to one time step. Thus, this method can be seen as an energy patching method. If one channel is filled with the stoichiometric ethane-air mixture at 300 K and 1 atm, the mass of ethane is 1.8194301×10^{-5} kg in the channel. The LHV of ethane is 47.80 MJ/kg, so the heat release is $47.80 \times 10^{6} \times 1.8194301 \times 10^{-5} = 869.7$ J. The volume of the channel is 2.6×10^{-4} m^3, so the volumetric heat release is $869.7/2.6 \times 10^{-4} = 3301909.2$ J/m^3. For the time step equal to 5×10^{-7} s, the volumetric heat release rate is $3301909.2/5 \times 10^{-7} = 6.6 \times 10^{12}$ W/m^3. In this method, the c_p was considered as a function of temperature. The values of c_p at different temperatures at 1 atm are tabulated in Table 5-2. A polynomial equation (Figure 71) obtained from the six order curve fitting was used in Fluent to calculate c_p.

Table 5-2: c_p at different temperatures at 1 atm [19]

T (K)	c_p (kJ/kg·K)	T (K)	c_p (kJ/kg·K)	T (K)	c_p(kJ/kg·K)
260	1005.3036	590	1048.8989	1400	1214.01
270	1005.3897	600	1051.1662	1450	1222.62
280	1005.5906	610	1053.4909	1500	1230.943
290	1005.8489	620	1055.8156	1550	1240.127
300	1006.1933	630	1058.169	1600	1249.024
310	1006.6238	640	1060.5511	1650	1258.495
320	1007.1117	650	1062.9332	1700	1267.966
330	1007.7144	660	1065.344	1750	1277.437
340	1008.3458	670	1067.7548	1800	1287.769
350	1009.092	680	1070.1656	1850	1298.388

Table 5-2 Con't

360	1009.8956	690	1072.5477	1900	1310.442
370	1010.7853	700	1074.9585	1950	1323.357
380	1011.8185	710	1077.3406	2000	1337.994
390	1012.8804	720	1079.7227	2050	1354.353
400	1014.0571	730	1082.1335	2100	1372.147
410	1015.2912	740	1084.5443	2150	1393.672
420	1016.6114	750	1086.9264	2200	1419.789
430	1018.0177	760	1089.2798	2250	1450.785
440	1019.5101	770	1091.6332	2300	1486.373
450	1021.0599	780	1093.9866	2350	1527.127
460	1022.6958	790	1096.34	2400	1573.908
470	1024.3891	800	1098.636	2450	1627.29
480	1026.1398	850	1110.403	2500	1688.134
490	1027.9479	900	1121.022	2550	1756.44
500	1029.8134	950	1131.928	2600	1836.8
510	1031.7363	1000	1141.973	2650	1925.77
520	1033.7453	1050	1151.731	2700	2026.22
530	1035.783	1100	1161.202	2750	2138.15
540	1037.8781	1150	1170.386	2800	2258.69
550	1040.0306	1200	1179.283	2850	2396.45
560	1042.1831	1250	1188.18	2900	2542.82
570	1044.393	1300	1197.077	2950	2697.8
580	1046.6316	1350	1205.687	3000	2858.52

To evaluate the effectiveness of each design, first a qualitative analysis will be performed by

examining the temperature contours and then a quantitative judgment will be done by comparing the mass flow rates through the inlets with the no prevention design. If the mass flow rate is higher than the no prevention design, the simulation using the energy patching method will be performed to investigate the effect of the backfire prevention feature on the engine efficiency.

5.2. Various Backfire Prevention Designs

5.2.1. No prevention design

To compare different backfire prevention designs, a no prevention design was tested without any prevention feature. The geometry of the no prevention design is shown in Figure 68.

During the third operation cycle, the operation reaches the periodic mode. From the temperature contour at the end of the third cycle shown in Figure 72, it can be seen that some hot gas exists in the air inlet blocking the flow and the air layer fails to be created between the exhaust gas and the mixture coming from the fuel inlet; some hot leakage gas exists at the inlet corner of the channel that is about to close. The results from three patching method are listed in Table 5-3.

5.2.2. Plan A: U channel

Two U channels were added next to the fuel inlet and the air inlet respectively. The configuration is shown in Figure 73. The idea of this feature is to redirect a part of the leakage jet to counteract with the left of the jet. When the leakage jet passes the inlet of the U channel, a part of is expected to flow through the channel. The jet out of the channel outlet and the jet passing

over the channel inlet are in different directions. When they merge, the direction of the merged jet is expected to be along the channel walls instead of being in the circumferential direction. In this way, the leakage flows into the rotor channels without causing a backfire in the fuel inlet or blocking the inflow from the air inlet.

The temperature contour is shown in Figure 74. Compared with Figure 72, the leakage prevention is not improved. The air inlet is still blocked and some hot gas still exists at the corner of the fuel inlet. From Table 5-3, the mass flow rate decreases by 0.3398% in the pressure patching simulation and increases by 1.812% in the temperature patching simulation. In either case, the backfire prevention is ineffective.

From the velocity vector plot sequence of the left U channel during one channel period (Figure), the idea is realized when the channel wall is between the two arms of the U channel and the left and the right arms are exposed to the high and lower pressure channels respectively. When they are exposed to the same channel, the leakage jet neglects the U channel and passes over it.

From the velocity vector plot sequence of the right U channel during one channel period (Figure), the same scenario happened to the right U channel.

Since this design is ineffective, the energy patching simulation was not performed to compare the efficiency change.

5.2.3. Plan B: modified U channel

If the distance between two arms of the U channel is greater than the channel inlet width,

the arms are always exposed to the different channels so that the inlet is always at a higher pressure than the outlet. In this way the leakage gas can always flows through the U channel. The U channel was modified based on this idea. The geometry of the modified U channel (MU channel) is shown in Figure 77.

The vector plot sequence (Figure) shows that the leakage gas flows through the left MU channel continuously and the merged flow is in the direction of the outlet wall, which justifies the idea of the MU channel. However, the backflow into the fuel inlet is observed as well.

The vector plot sequence (Figure) shows that the leakage gas flows through the right MU channel continuously and the merged flow is in the direction of the outlet wall. However, when the jet out of the outlet impacts on the rotor channel wall, a part of it is deflected and goes into the air inlet.

The temperature contour is shown in Figure 80. Compared with the previous designs, the leakage to the air inlet does not change much, but that to the fuel inlet is more severe. From Table 5-3, the mass flow rate decreases by 21.11% in the pressure patching simulation and decreases by 10.92% in the temperature patching simulation. In either case, the leakage is worse.

From the pressure contour (Figure 81), it is found that the gauge pressure in the left MU channel is between 0.855 bar and 0.765 bar which is much higher than that in the left U channel which is between 0.270 bar and 0.225 bar. The gauge pressure in the right MU channel (0.135 ~ 0.180 bar) is higher than that in the right U channel (0.045 ~ 0.090 bar). This is because the inlets of the MU channels are connected to the regions at higher pressure. Although this makes the leakage continuously flows through the channels, the high pressure merged flow causes more hot

gas to go into the inlets.

Since this design is ineffective, the energy patching simulation was not performed to compare the efficiency change.

5.2.4. Plan D: leakage pipe

In this design, the leakage jets on both sides of the inlets are taken away and re-injected to the turbine to generate power. The configuration of a WDE with the leakage pipes is shown in Figure 82.

The temperature contour is shown in Figure 83. It is observed that there is no hot gas in the air inlet and a thin air layer is created behind the exhaust gas in the rotor channel; the hot gas located at the corner of the fuel inlet and near the inlet of the rotor channel just closed is much less than the no prevention design, which qualitatively prove the effectiveness of the leakage pipes. From Table 5-3, the mass flow rate increases by 17.17% in the pressure patching simulation and increases by 17.25% in the temperature patching simulation, which quantitatively justifies this design. Then an energy patching simulation was performed to examine the effect of the leakage pipes on the engine efficiency. However, even though the mass flow rate increases by 12.01%, the efficiency decreases by 1.88%.

5.2.5. Plan E: jagged housing wall

In this design, some grooves are cut on the inner housing wall on both sides of the inlets to bring more resistance to the leakage flow. The geometry is shown in Figure 84. The width of the groove is 1.1 mm, the left wall is radial and the right wall has an angle of 30° with respect to the

periphery. There are 13 grooves on each side of the inlets.

From the temperature contour shown in Figure 85 it can be seen that the hot leakage prevention is more effective than the leakage pipe design. From Table 5-3, the mass flow rate increases by 19.25% in the pressure patching simulation and increases by 17.26% in the temperature patching simulation. According to the result from the energy patching simulation, the mass flow rate increases by 16.56% and the efficiency by 20.7%. Among all the backfire prevention designs, the engine with the jagged housing wall has the highest mass flow rate and the highest efficiency.

Table 5-3: Results of various backfire prevention designs

		No prevention	Leakage pipe	Jagged wall	U channel	MU channel
Pressure patching	$\dot{m}_{mean}$ (kg/s)	0.7357	0.8620	0.8773	0.7332	0.5804
	$\dot{m}_{mean}$ increment (%)	0	17.17	19.25	-0.3398	-21.11
Temperature patching	$\dot{m}_{mean}$ (kg/s)	0.7671	0.8994	0.8995	0.7810	0.6833
	$\dot{m}_{mean}$ increment (%)	0	17.25	17.26	1.812	-10.92
	$P_{patching}$ (barg)	7.759	8.246	8.891	7.802	6.652
Energy patching	$\dot{m}_{mean}$ (kg/s)	0.7658	0.8578	0.8926		
	$\dot{m}_{mean}$ increment (%)	0	12.01	16.56		
	power (kW)	27.47	26.93	33.19	-	
	Efficiency (%)	2.13	2.09	2.57		
	Efficiency increment (%)	0	-1.88	20.7		

CHAPTER 6. CONCLUSIONS AND FUTURE WORK

6.1.Summery and Conclusions

The principle of the WDE is described. Thermodynamic analysis of the WDE is performed on a single channel and a full rotor. Through the single channel analysis, the general forms of the net work extracted from the flow and the thermal efficiency are obtained in terms of the mass-average properties. The results of the full rotor analysis are identical to those of the single channel analysis. The analysis shows that under some certain conditions, the thermal efficiency of the WDE can be equal to the Humphrey cycle efficiency. Thus, the mass-average flow can be idealized as a Humphrey cycle.

A 1D numerical code is created using the TVDM scheme to predict the ports timing. The wave diagram is obtained from the 1D code. The results from the 1D code and Fluent 2D simulation show a good consistency between them.

The necessary geometric adjustments for a given rotor and working conditions are introduced.

The energy loss of the WDE is examined by a 2D simulation of a single channel. The results show that the two sources of loss are the significant outgoing kinetic energy and the under-expansion of the burned gas.

The torque generation mechanism in the expansion process is investigated. For the WDE channel, the torque is generated by the traveling expansion wave in the channel. The relationship

between the blade angle and the pressure gradient is obtained. Through the tests of various channel shapes, it is discovered that smaller outlet opening of the channel leads to a longer expansion process and hence a higher efficiency. The mechanism of the torque oscillation was examined by the analysis of the pressure profiles. The analysis yields the conclusion that the channel outlet should be at the outer radius. The convergent channel is considered as the best channel shape and is implemented on a full WDE to improve the efficiency. With the convergent channel the efficiency increases from 2.2% to 3.3%.

The effects of the peak pressure, the rotor dimension and the rotational speed on the engine efficiency are investigated by the single channel simulations. The results show that a lower peak pressure has a higher efficiency but a lower power. Whether to use a low peak pressure depends on the priority of the power and efficiency. Bigger rotor dimension and higher rotational speed can increase the efficiency by increasing the channel tip speed and consequently reducing the outgoing velocity. The results are tested on the full engine for validation.

Two methods are proposed to reuse the energy from the exhaust gas – utilizing a return channel and incorporating an external turbine. Preliminary investigation into the guide vanes and the external turbine blades are performed. Incorporating an external turbine, the efficiency increases to 11%.

To prevent the backfire, several plans are examined. By qualitative and quantitative analysis, the best backfire prevention design is determined to be the jagged housing wall.

6.2.Suggestions for Future Work

The 1D code does not take into account any losses and 2D effect, such as the leakage, the heat loss, the gradual opening and closing, the channel curvature and the variation of the channel cross section area. In the future, the governing equation will be sophisticated to consider these effects. In the current code, the outflow B.C. uses a simple extrapolation method. More advanced outflow B.C. will be adopted.

In the channel shape investigation, only the expansion process is considered. However, the shape best for the expansion may not be good for the scavenging and compression. In the future, the channel performance for the full operation cycle will be studied. Moreover, more complex shapes will be proposed to enhance the energy extraction performance.

Since the WDE with the external turbine has the best efficiency so far, more research will be focused on the optimization of this design. The characteristics of the internal flow should be investigated in detail. For example, due to the unsteady nature, the outlet condition of the channel varies with time and consequently the inlet conditions of different nozzles are different from each other. Since the nozzle passages are of the same shape, the nozzle outlet conditions are different. Thus, as the blade passes the nozzles, its inlet sees different conditions. Therefore, the blades operate on the off-design conditions for some time during one rotational cycle. In the future, the nozzle passages should be redesigned to have different geometries such that the nozzle outlets are at the identical condition.

The working range of the backfire prevention features should be examined. Combination of

various features may be more effective, which is of interest. Since the leakage is a very important loss for wave engines, the research on the seal methods will continue, not only to avoid the backfire but also to reduce the energy loss.

Since the efficiency of Humphrey cycle increases with the precompression ratio, methods to enhance the precompression by the shock wave will be studied. Since the hammer shock wave is very weak, a second shock wave can be generated by sending the burned gas back to the channel with the mixture (Figure 86).

Besides, a critical factor is the flame speed. If the combustion takes a long time, the WDE has to operate at low rotational speeds, which decreases the efficiency. More advance methods to accelerate the combustion should be utilized. One of them is to use EGR to ignite the mixture.

In the future, with the high performance computers, 3D simulations can be carried out to provide more realistic information.

This work concentrates on the numerical investigations only. Experiments should be done to validate the conclusions of the numerical analysis.

APPENDIX

APPENDIX
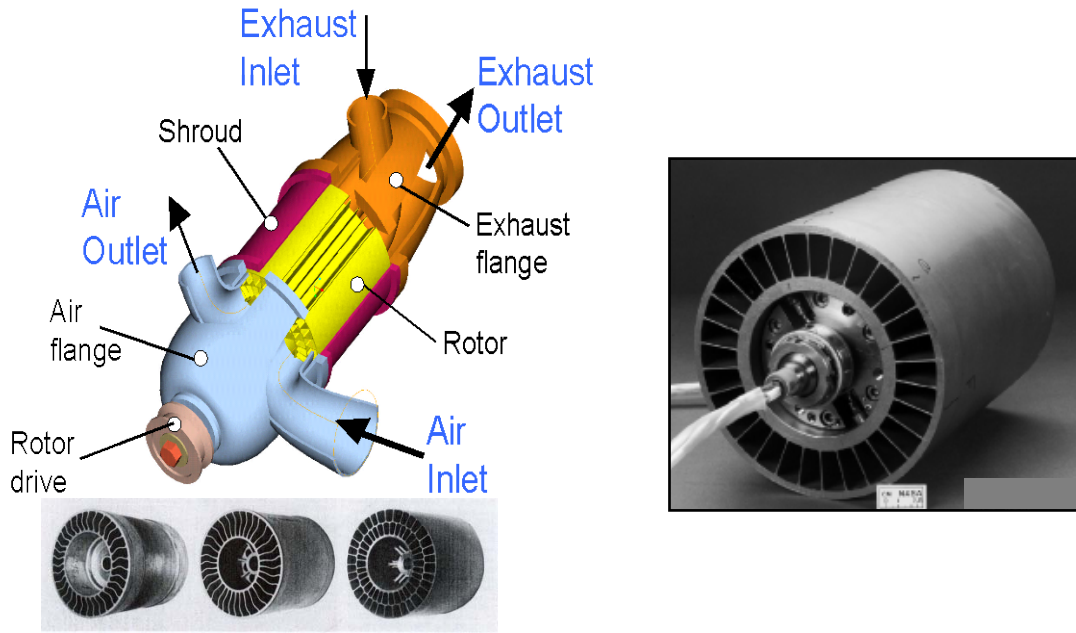
Figure 1: Schematic model of a wave rotor inside the pressure wave supercharger (PWS) with its development stages (soldered, cast with single of channels, cast with double row of channels) and actual NASA four port wave rotor drum (right). For interpretation of the references to color in this and all other figures, the reader is referred to the electronic version of this dissertation.
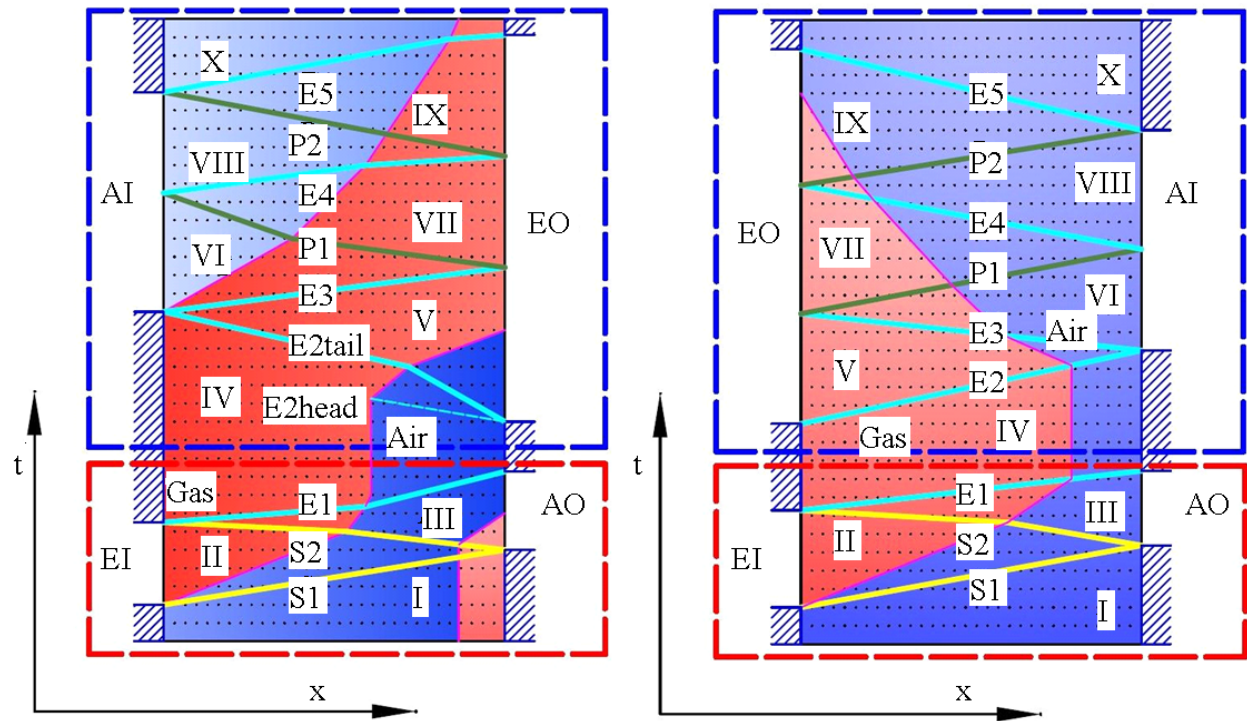
Figure 2: Porting and flow scheme for a through-flow (left) and reverse flow wave rotor (taken from [55])
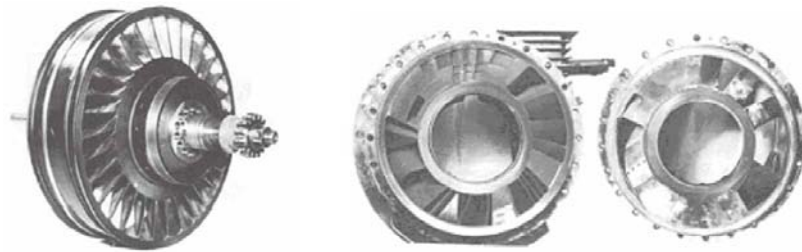
Figure 3: Assembly of successfully working wave engine with wave rotor (left) and rear and front stator plates [3]
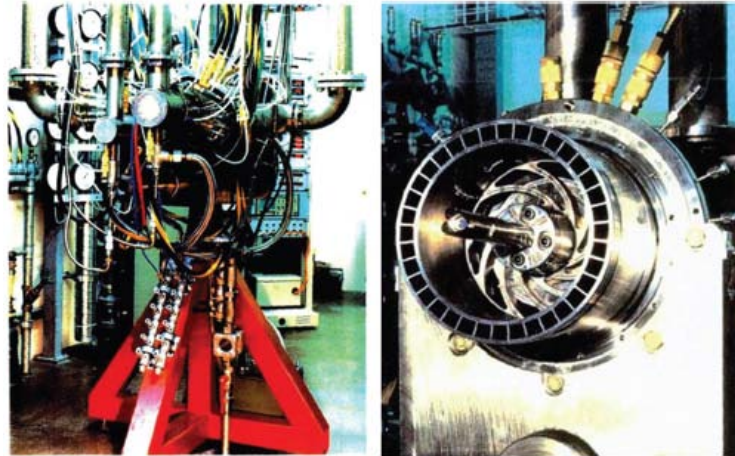
Figure 4: ABB test rig (left) and wave rotor combustor cross section (right) [4]
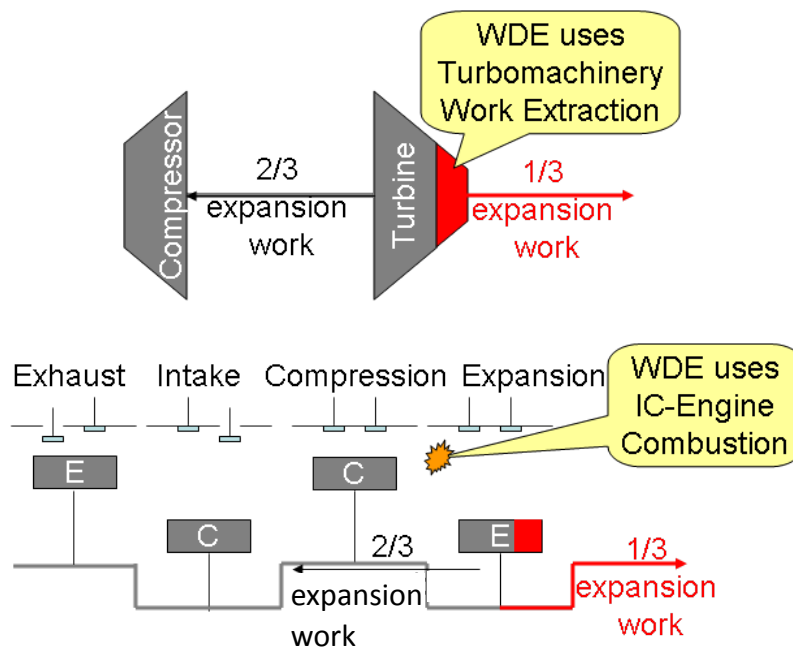
Figure 5: By using shockwaves for internal work transmission, the Wave Disk Engine virtually eliminates the hardware (shown in gray) in gas turbines and internal combustion engines that serve to transmit expansion work internally to perform the needed inlet gas compression.
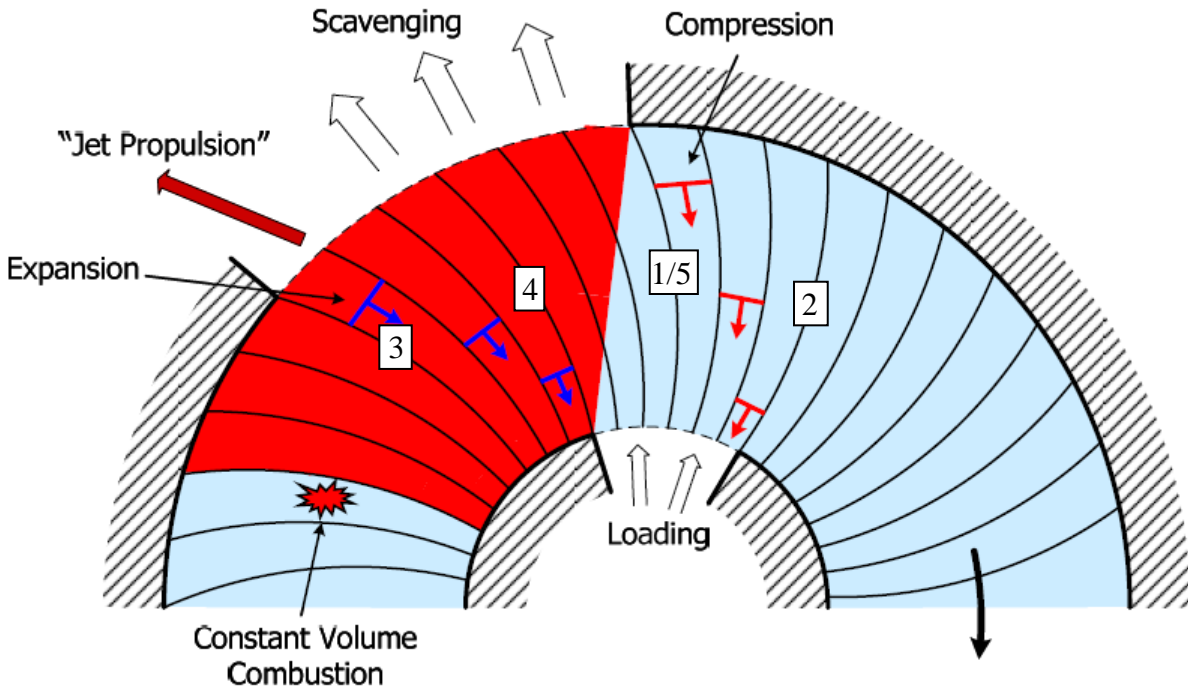
Figure 6: Schematic of an internal combustion WDE
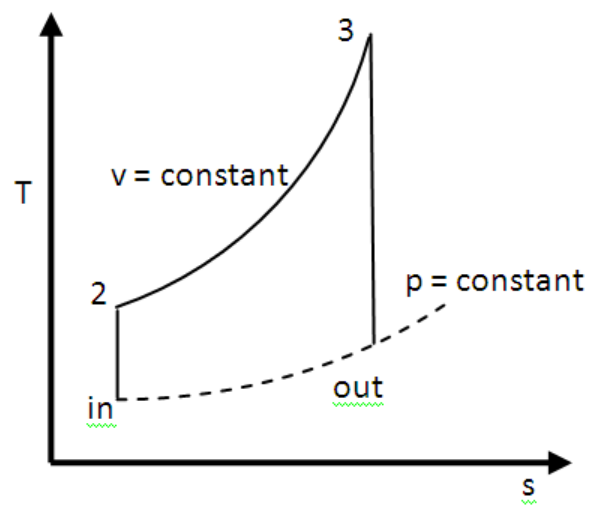
Figure 7: T-s diagram of the mass-average flow in a WDE
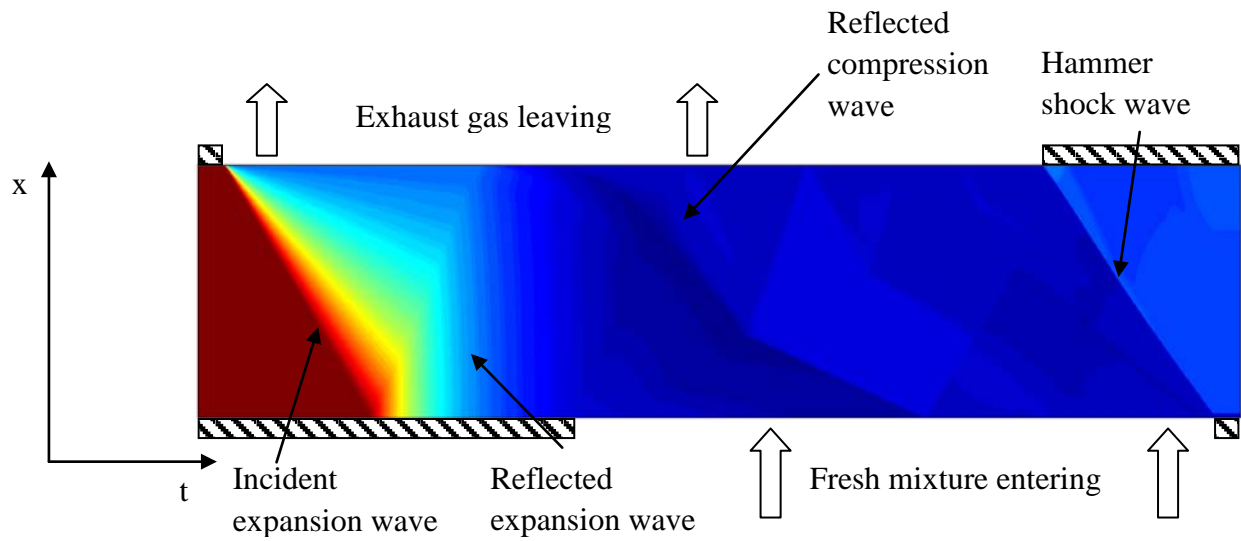
(a) Pressure contour
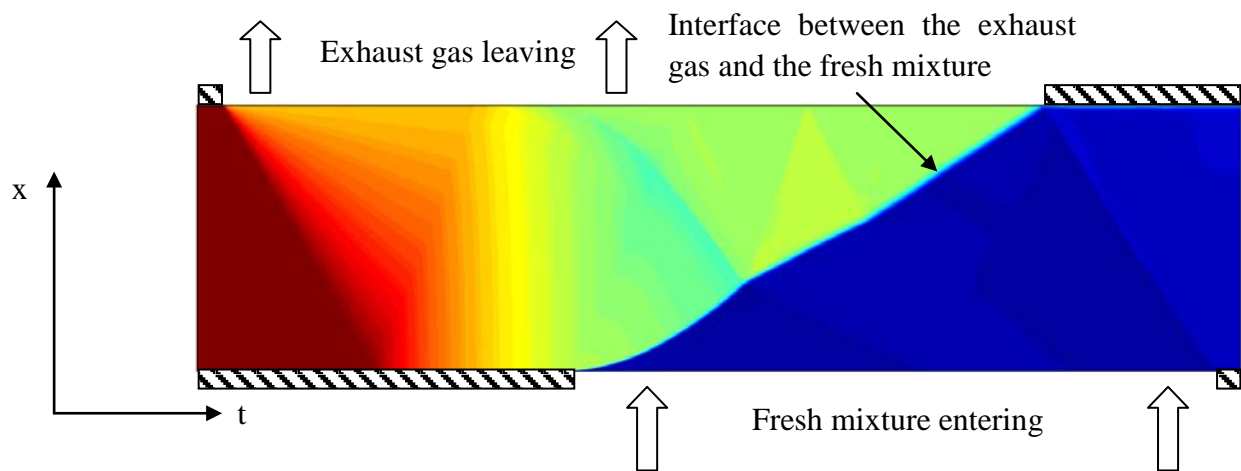
(b) Temperature contour

Figure 8: Wave diagram obtained from the TVDM scheme

88
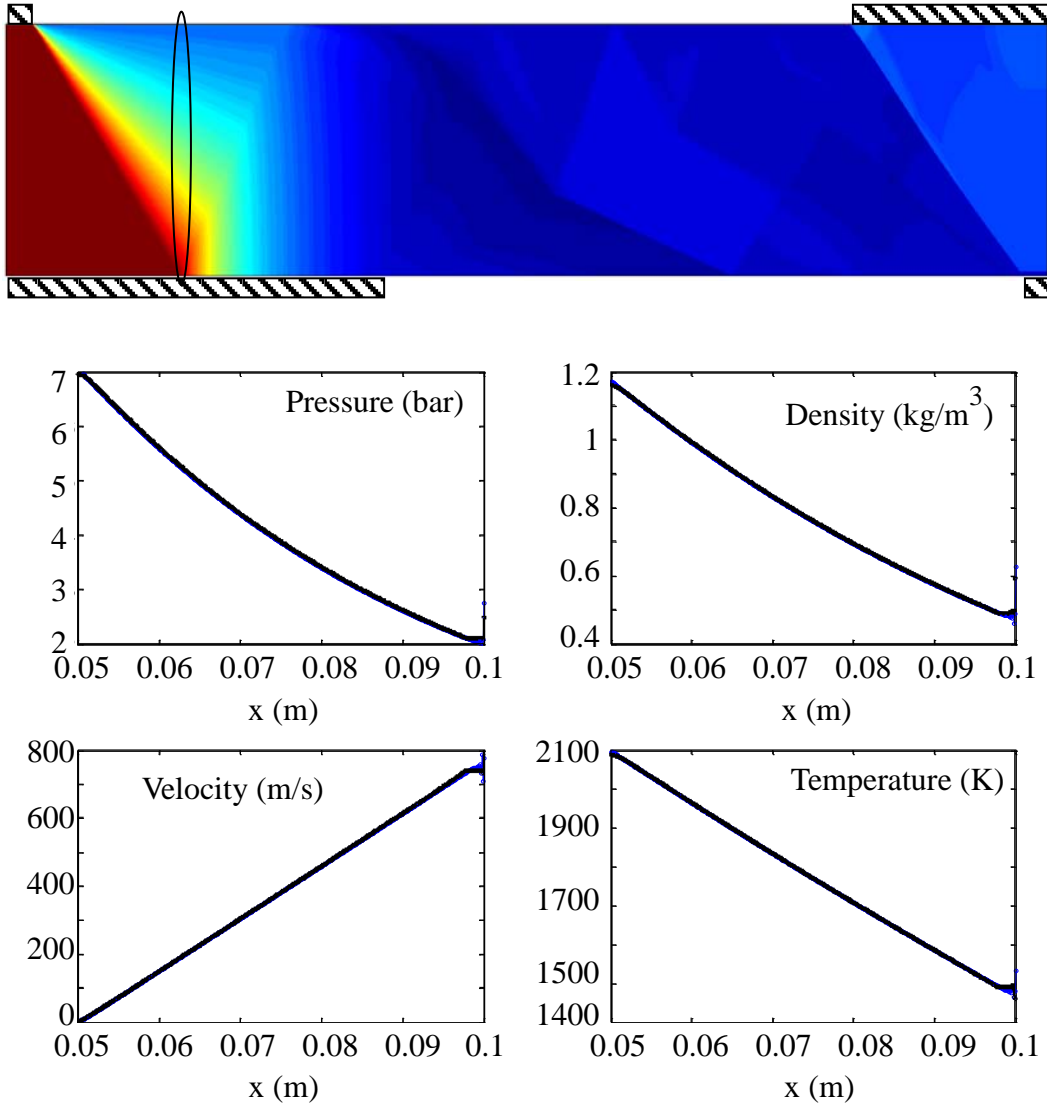
Figure 9: Profiles of pressure, density, velocity and temperature for TVDM scheme (black) and GT scheme (blue) at 5.44e-5 s and its corresponding location in the wave diagram
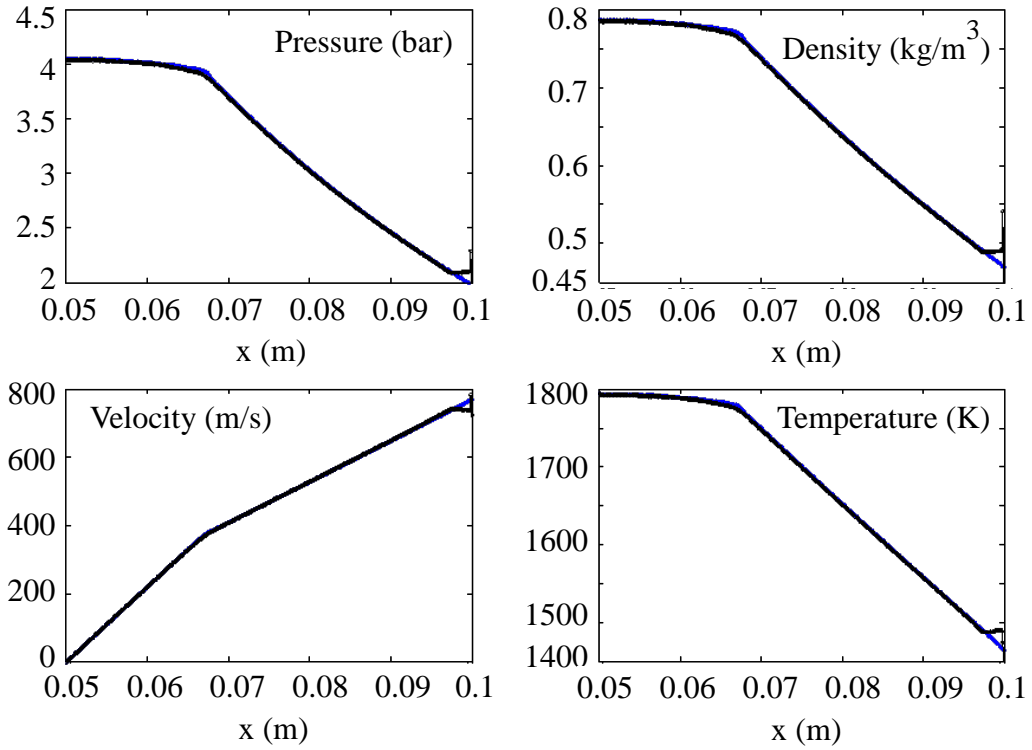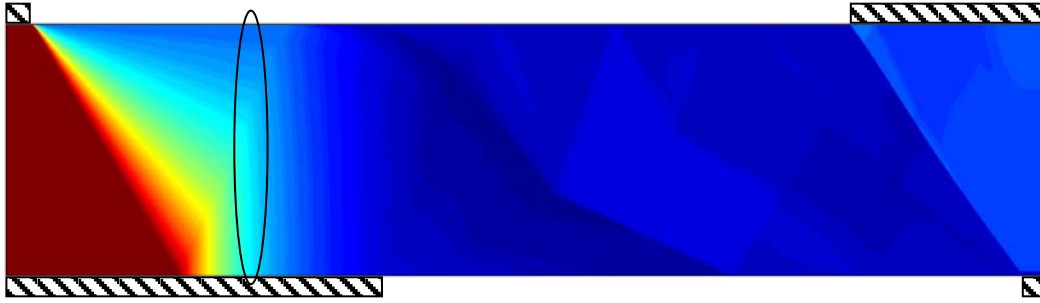
Figure 10: The profiles of pressure, density, velocity and temperature from GT scheme (blue) and TVDM scheme (black) at 7e-5 s and its corresponding location in the wave diagram
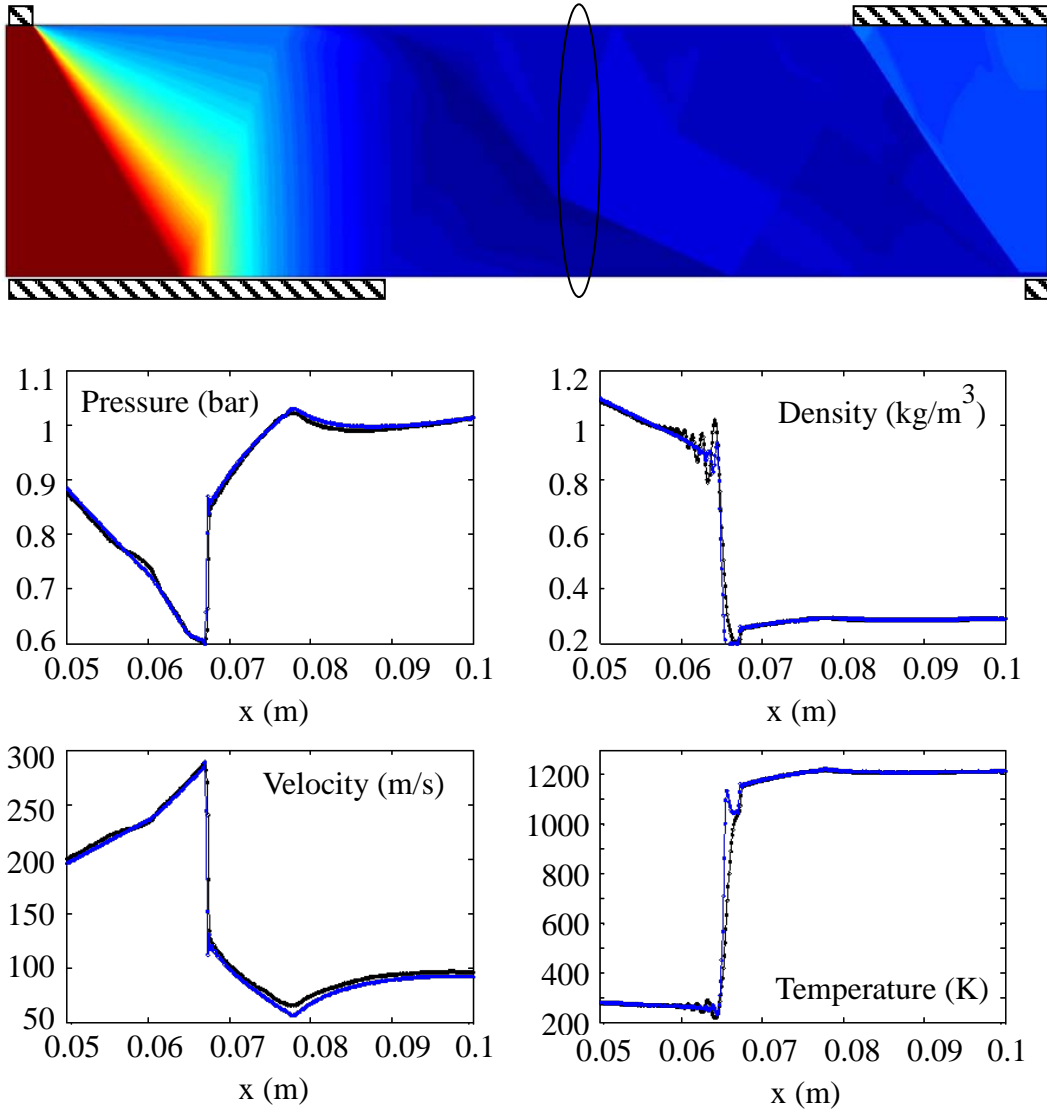
Figure 11: Profiles of pressure, density, velocity and temperature from (b) GT scheme (blue) and TVDM scheme (black) at 2.3e-4 s and its corresponding location in the wave diagram (a)
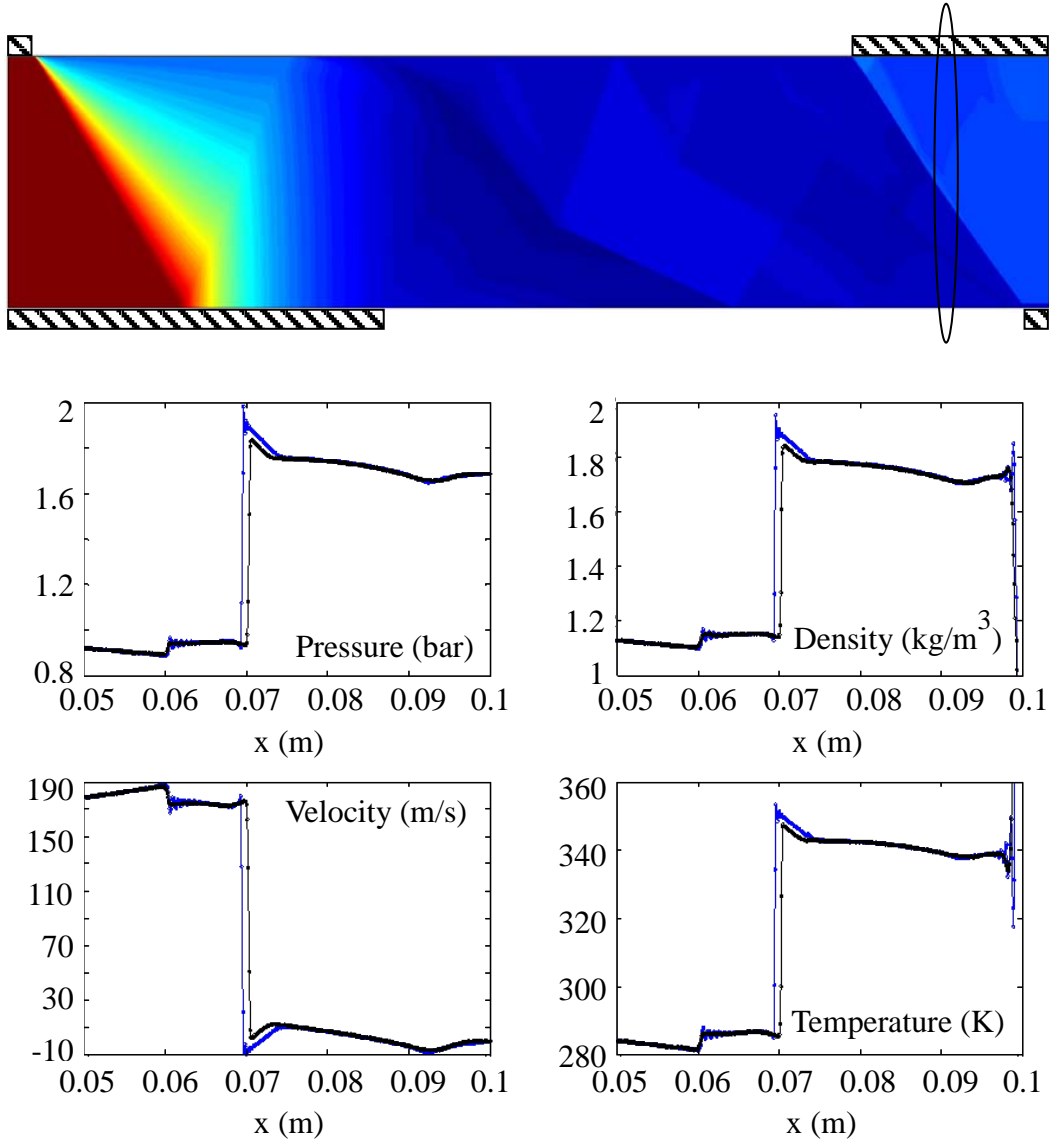
Figure 12: Profiles of pressure, density, velocity and temperature from (b) GT scheme (blue) and TVDM scheme (black) at 5.33e-4 s and its corresponding location in the wave diagram (a)
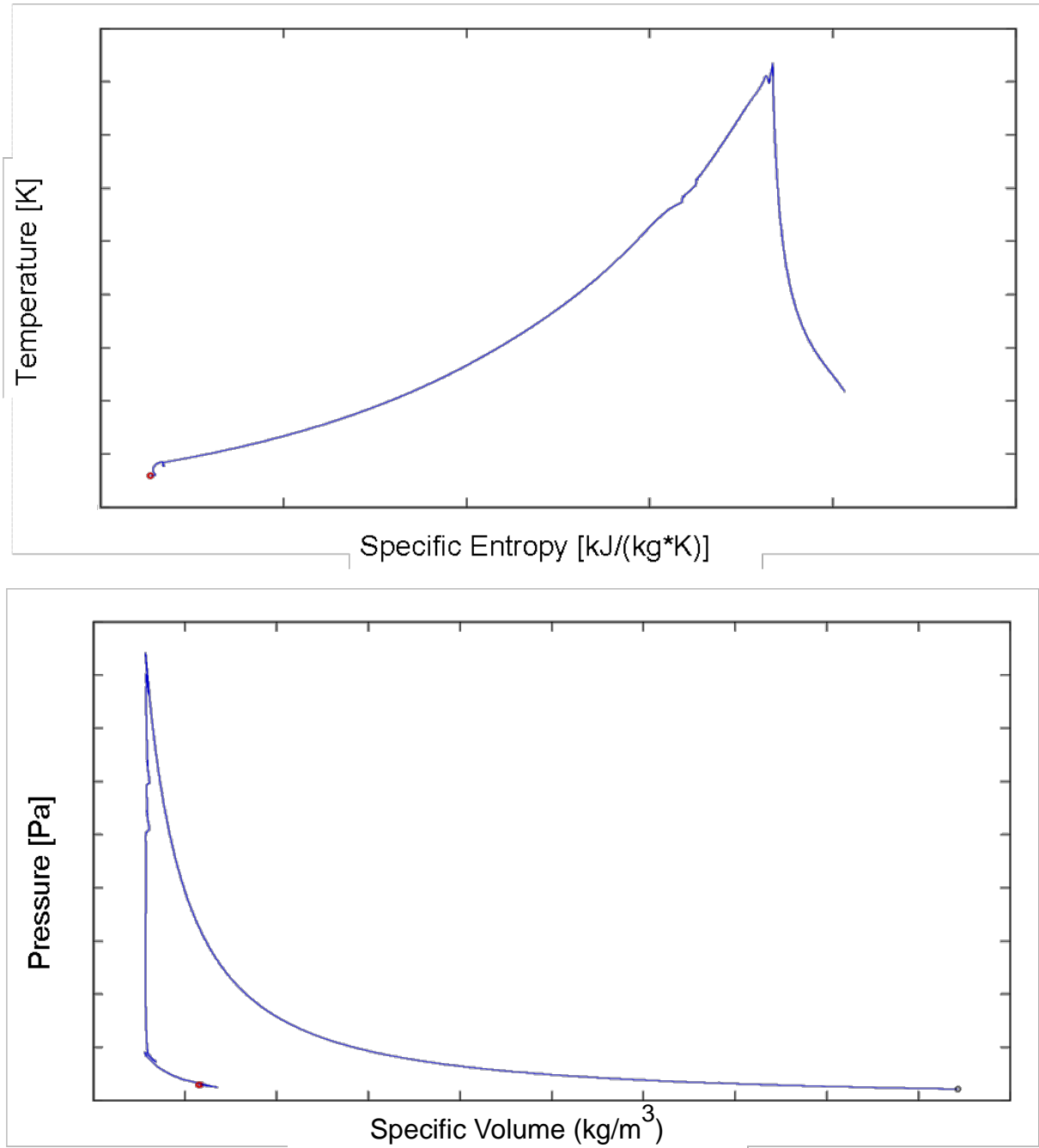
Figure 13: T-s diagram (upper) and p-v diagram (lower) for one fluid particle
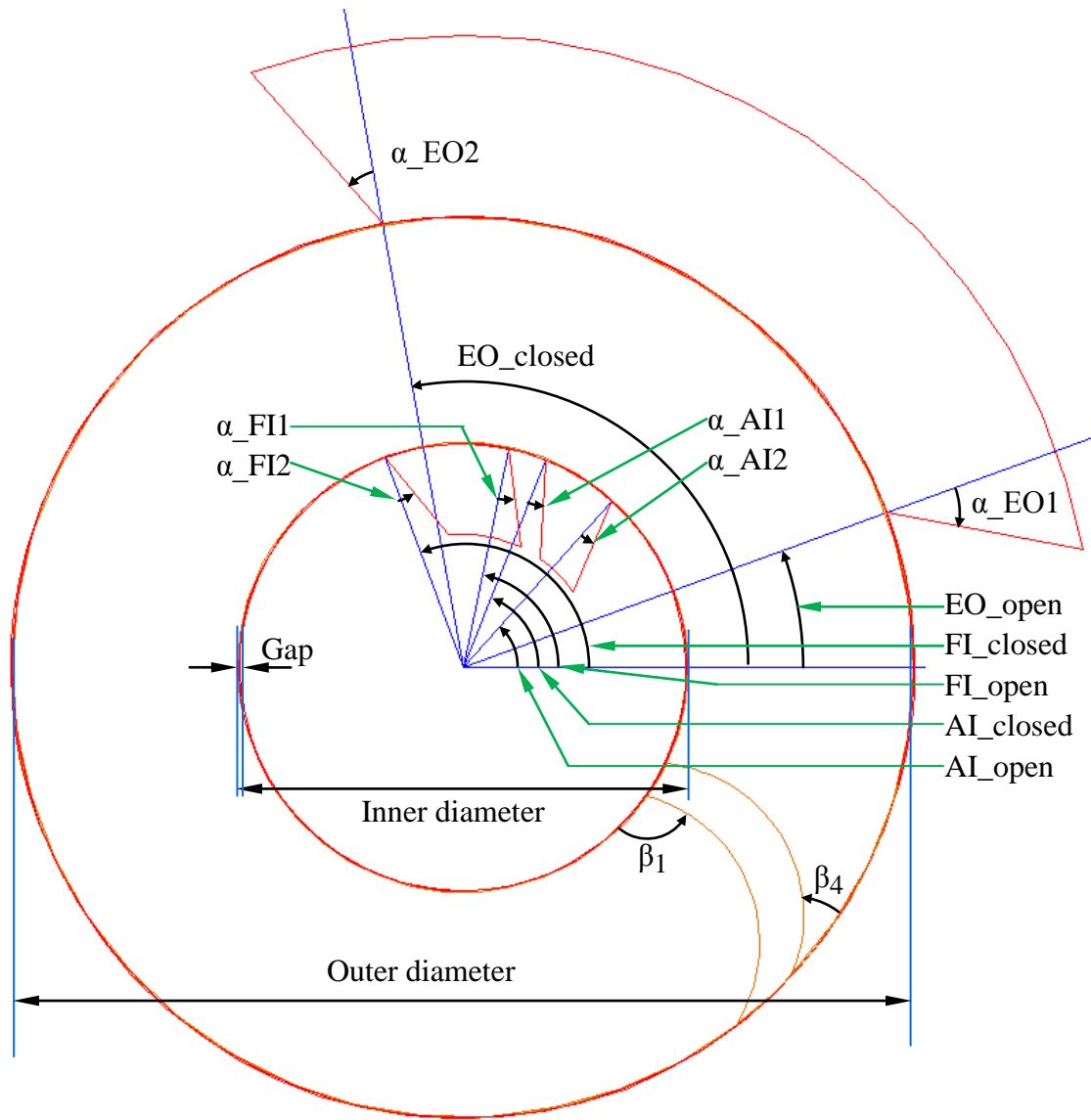
Figure 14: Geometric parameters of a WDE
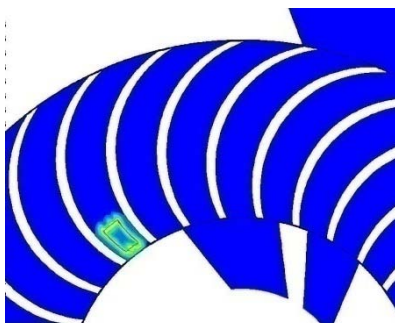
Figure 15: Heater for ignition
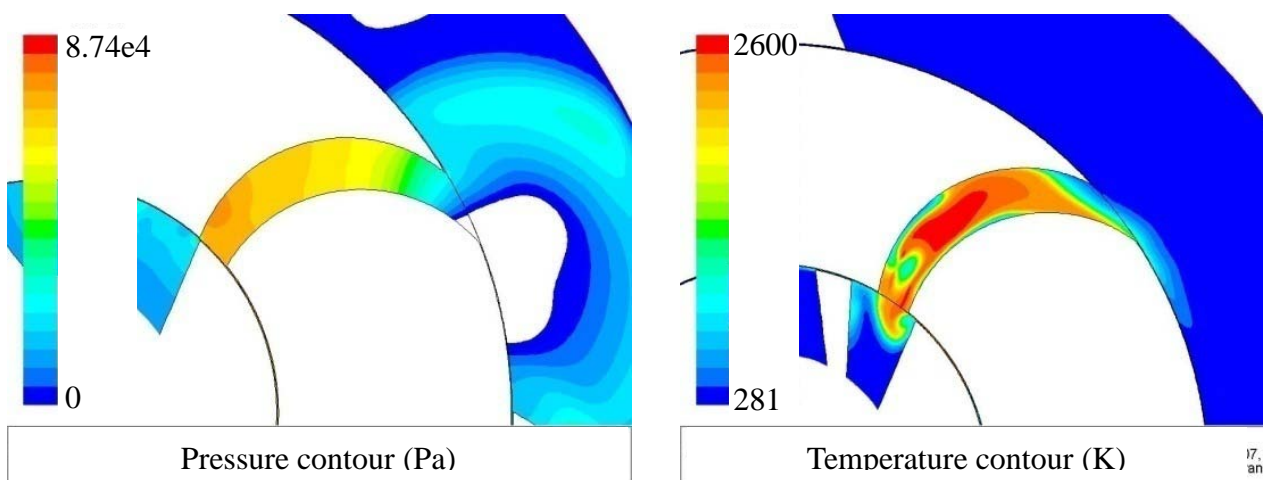
Figure 16: Backflow into the air inlet

(a)

(b)
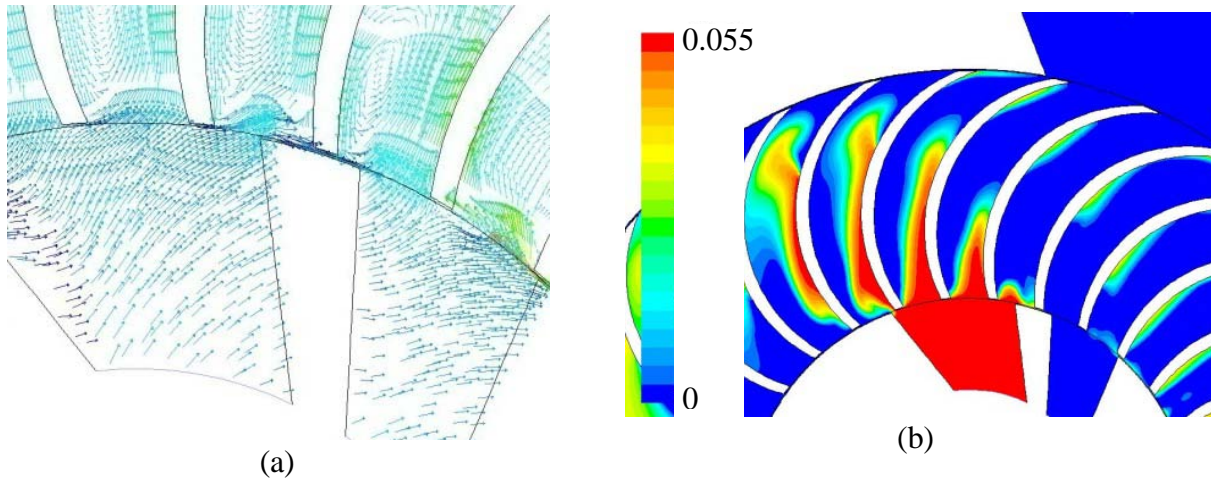
Figure 17: Relative velocity vector plot (a) and contour of mass fraction of methane (b)

(a)

(b)
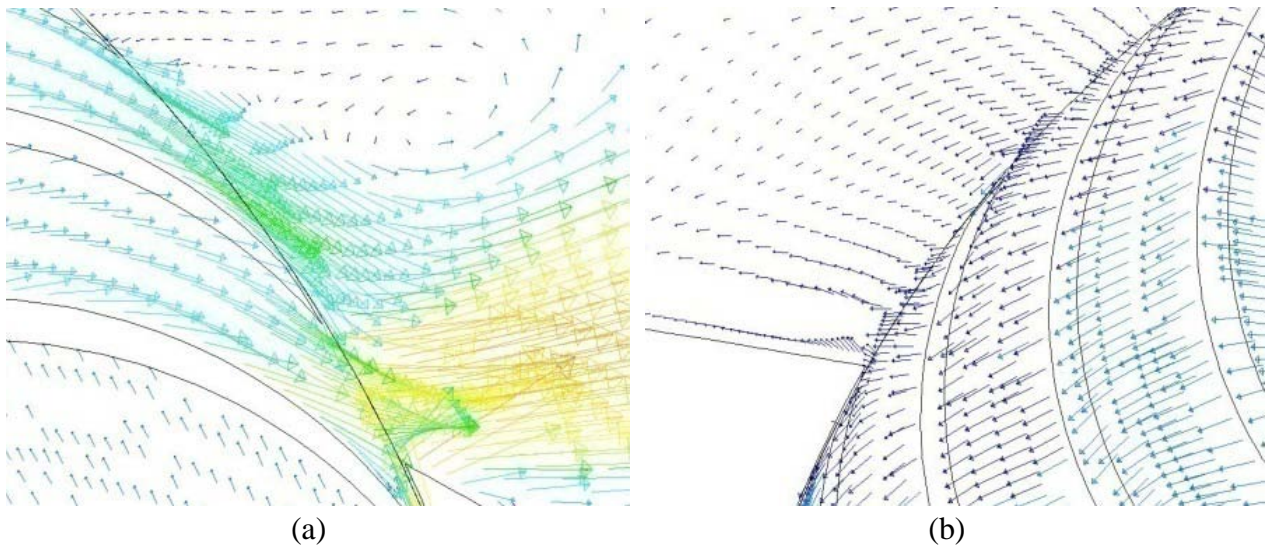
Figure 18: Absolute velocity vector plot near the inlet (a) and outlet (b)
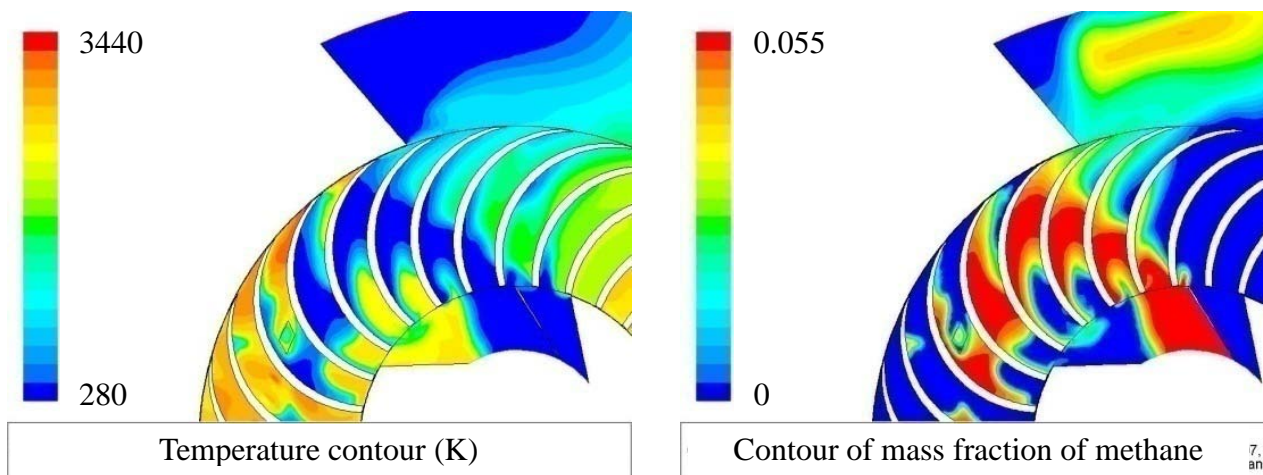
Figure 19: Backfire into the fuel inlet

0.055	
0	
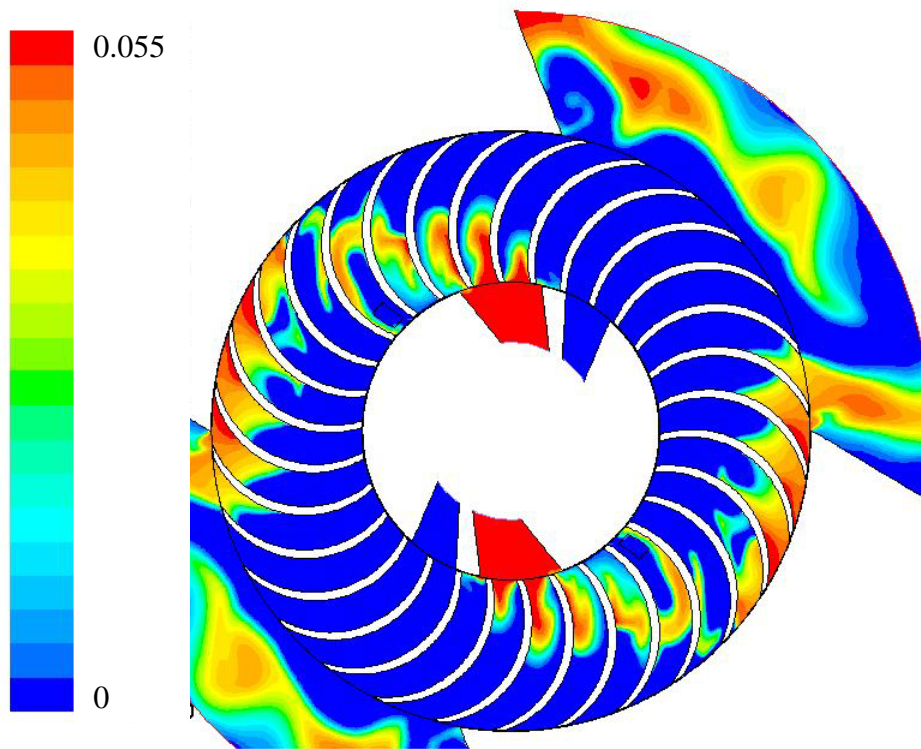
Contour of mass fraction of methane

Figure 20: Incomplete combustion

(a)   (b)

(c)
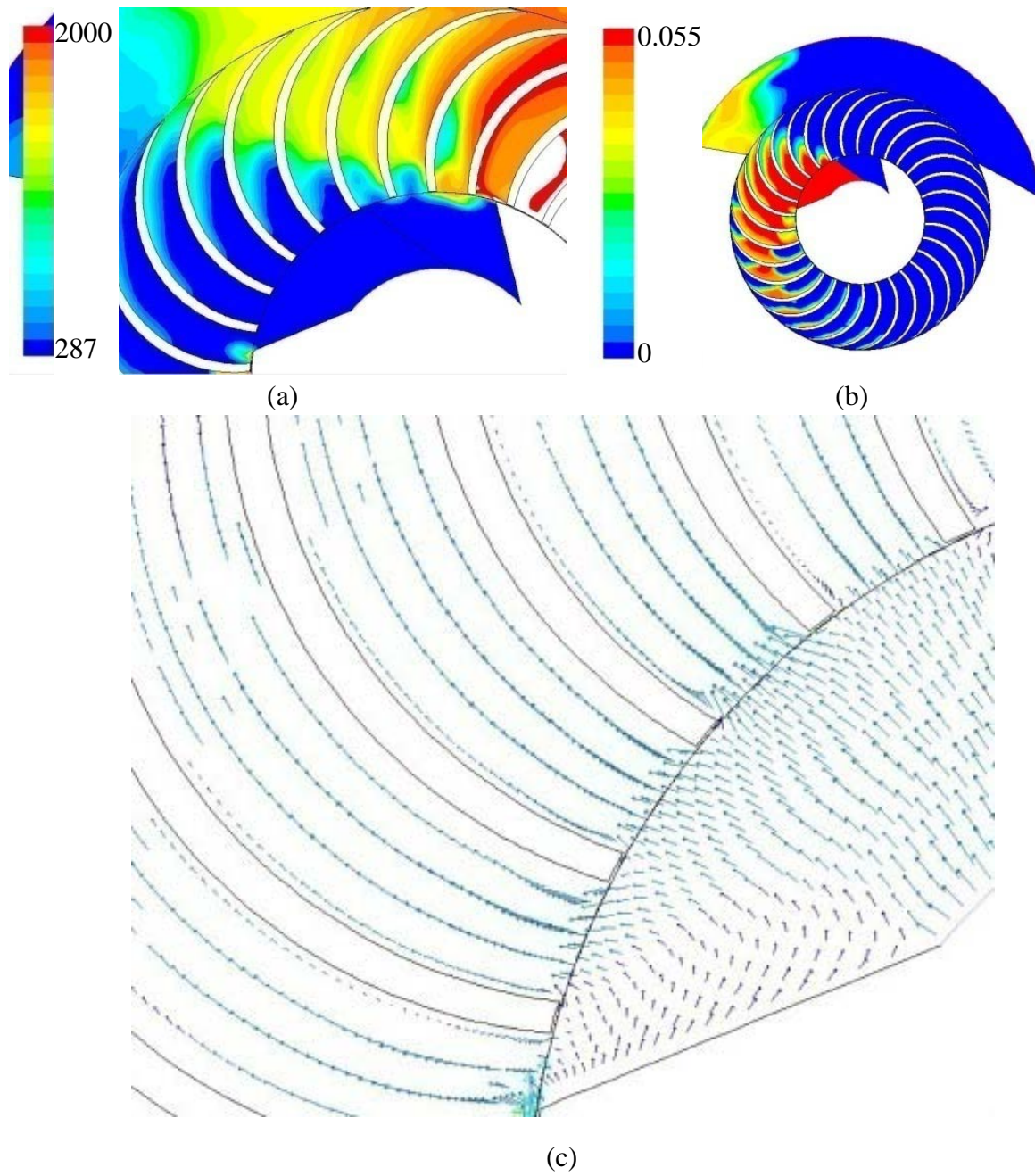
Figure 21: (a) temperature contour, (b) mass fraction of methane contour and (c) relative velocity vector plot for the baseline design
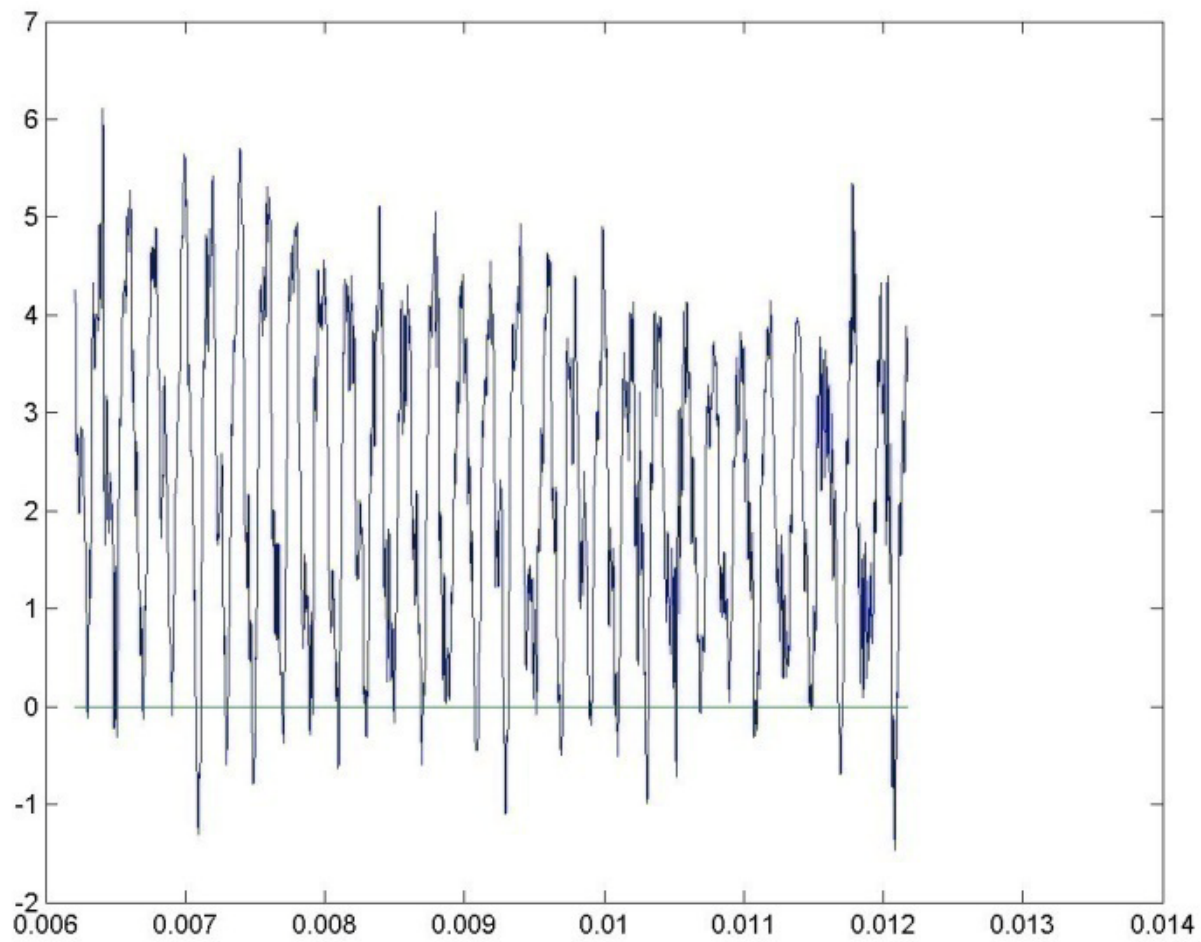
Figure 22: Power history in the second cycle
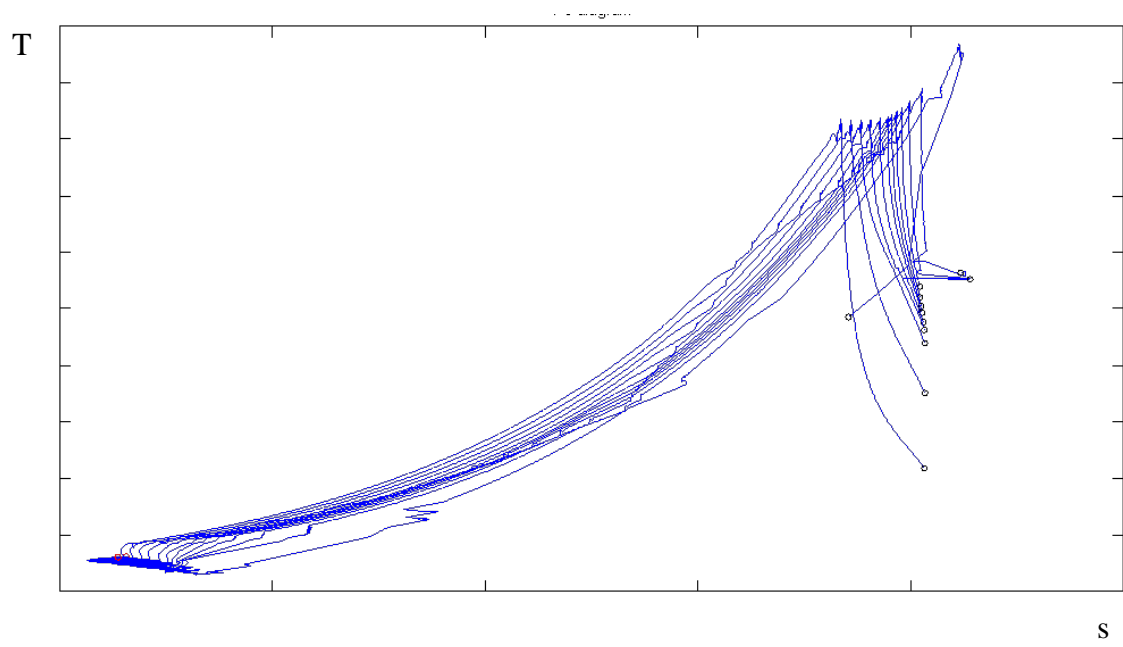
Figure 23: T-s diagrams of 10 particles in the channel
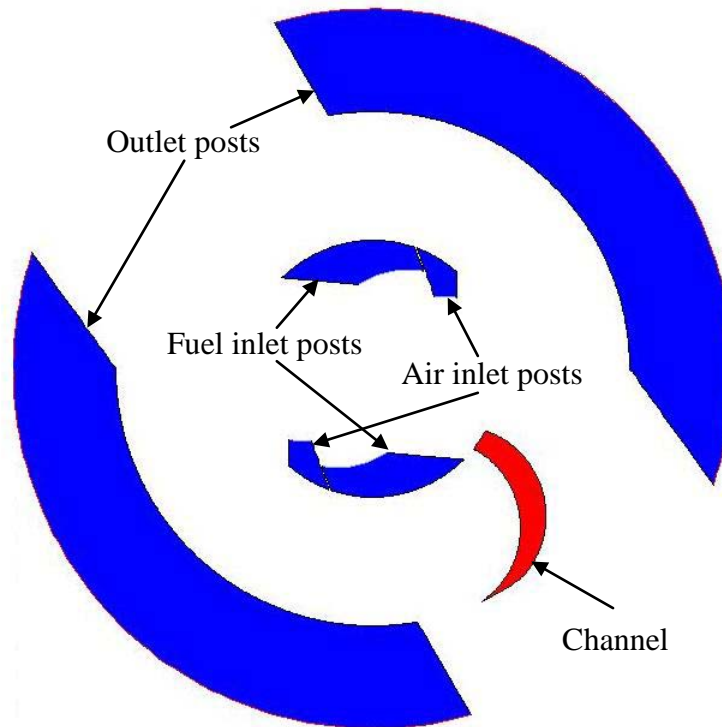
Figure 24: Geometry for the 2D investigation
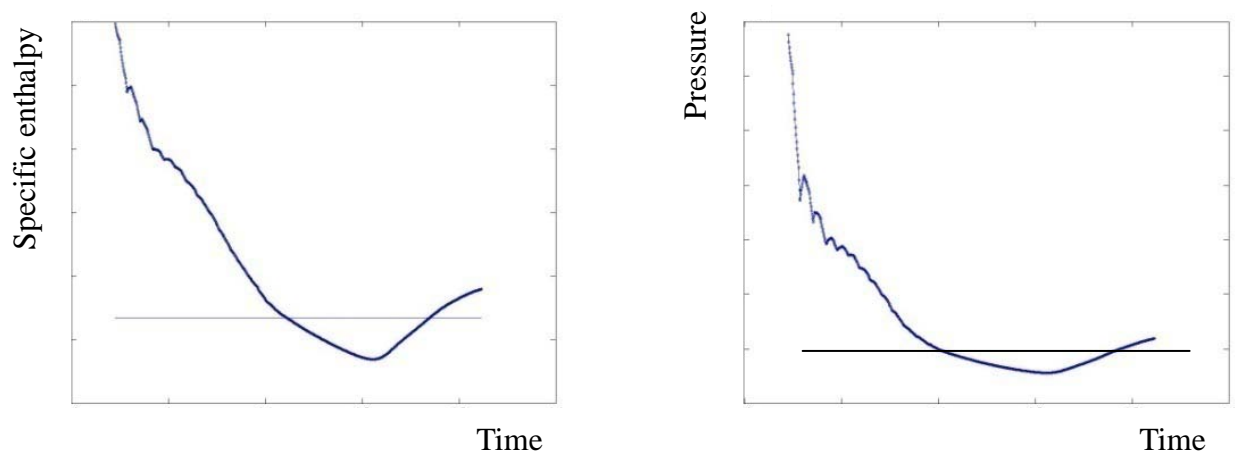
Figure 25: Histories of the outlet enthalpy (left) and outlet pressure (right) of the 2D simulation
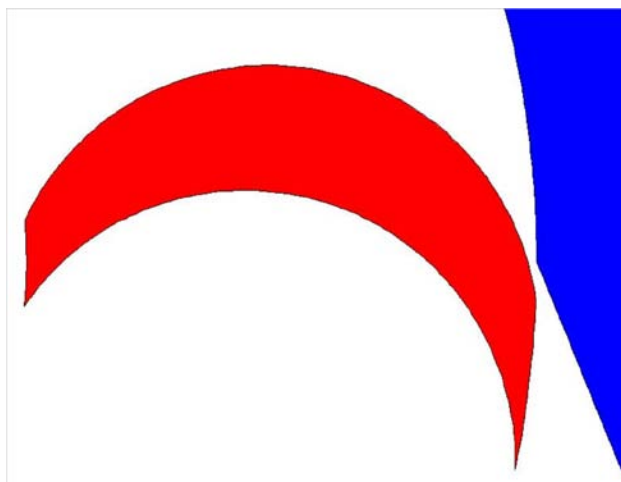
Figure 26: Geometry of the C2 channel

8.55e-3

-1.63e+3
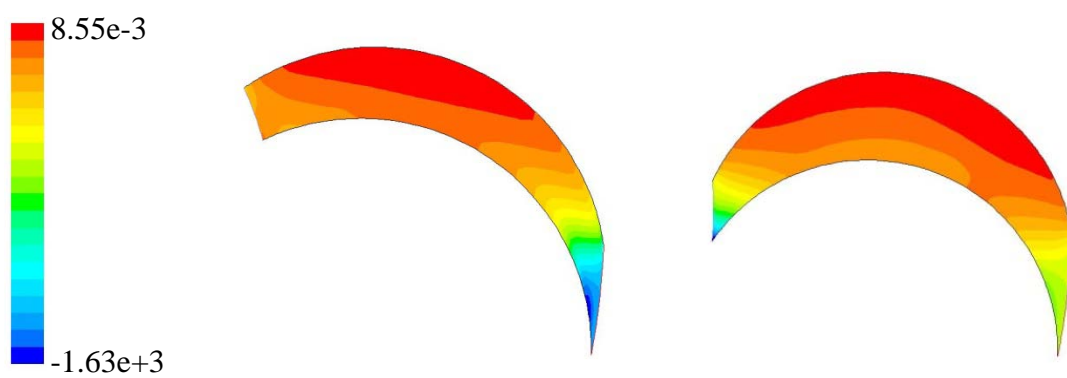
Figure 27: Pressure contours (Pa) in the curved channels
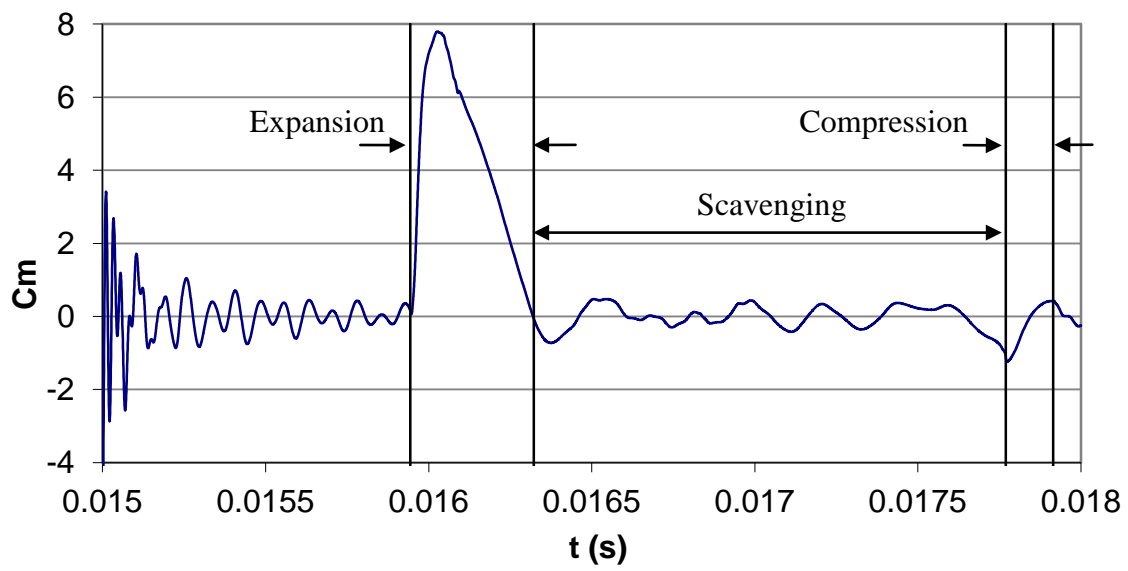
Figure 28: History of the moment coefficient on the channel walls
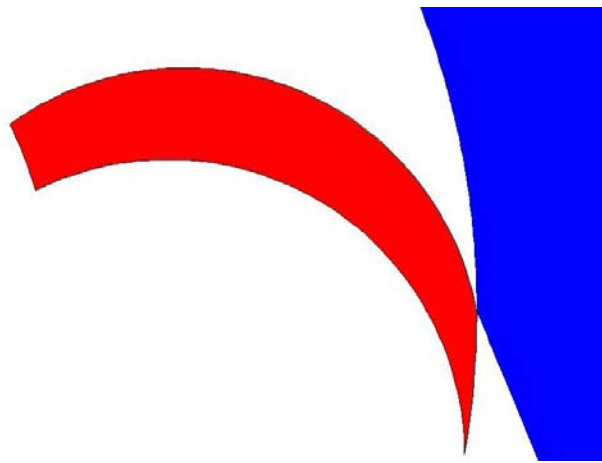
Figure 29: Geometry of the baseline shape
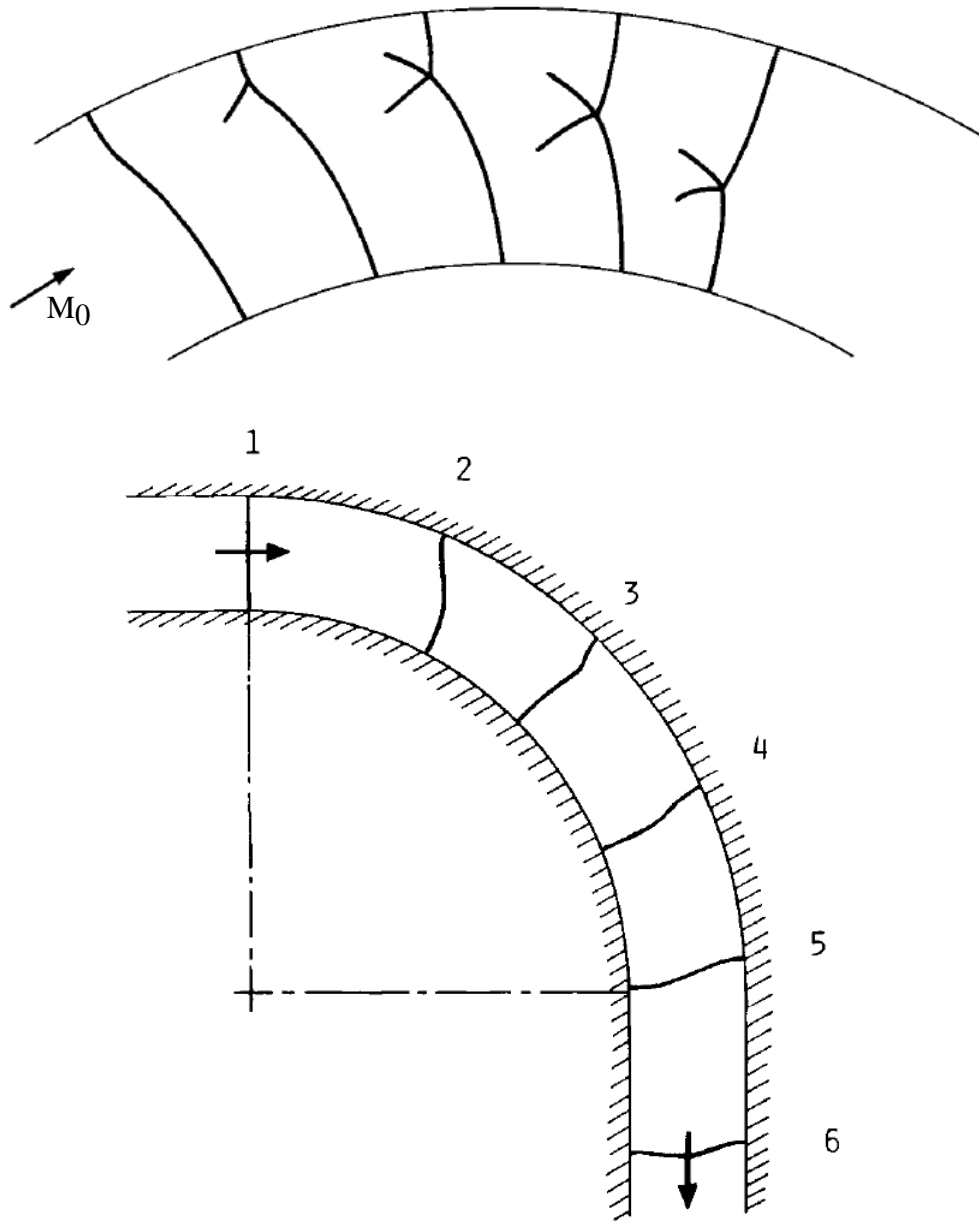
Figure 30: Profiles of a shock wave (top) and a planar acoustic wave (bottom) through a two-dimensional right-angle bend, numbers 1 - 6 are representative wave front configurations within the bend (Edwards et al [12], Kentfield [23])

(1)   (2)

(3)   (4)

(5)   (6)
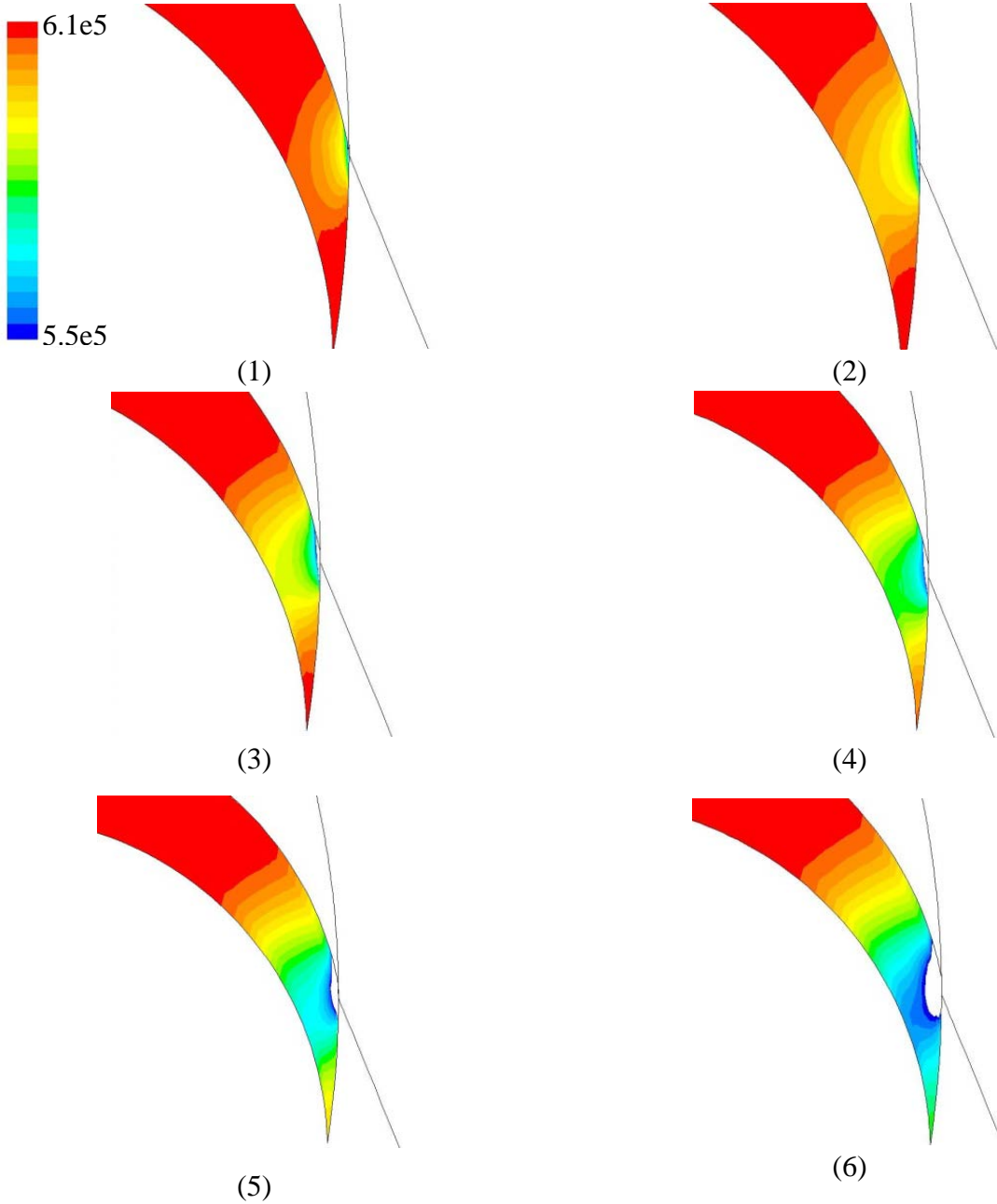
Figure 31: Sequence of the pressure contours when the channel just opens
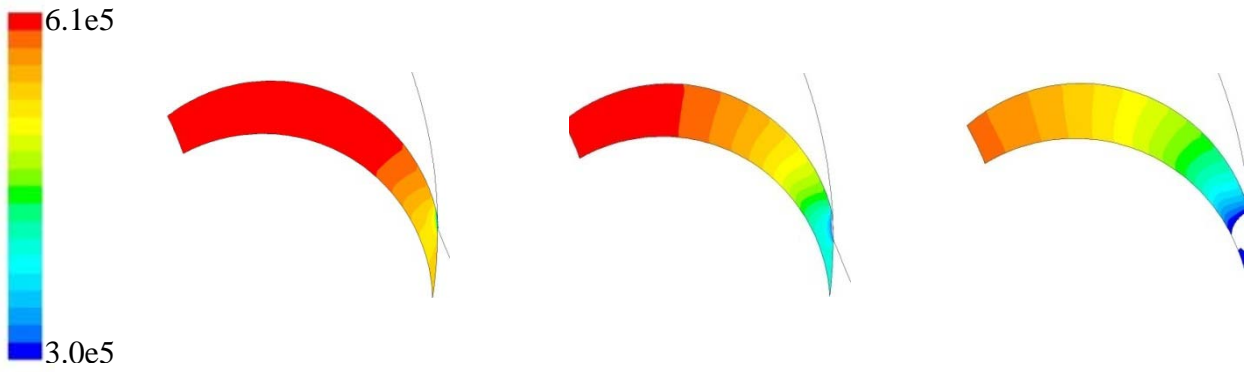
Figure 32: Sequence of the pressure contours during the incident expansion wave propagates

(1)

(2)

(3)

(4)
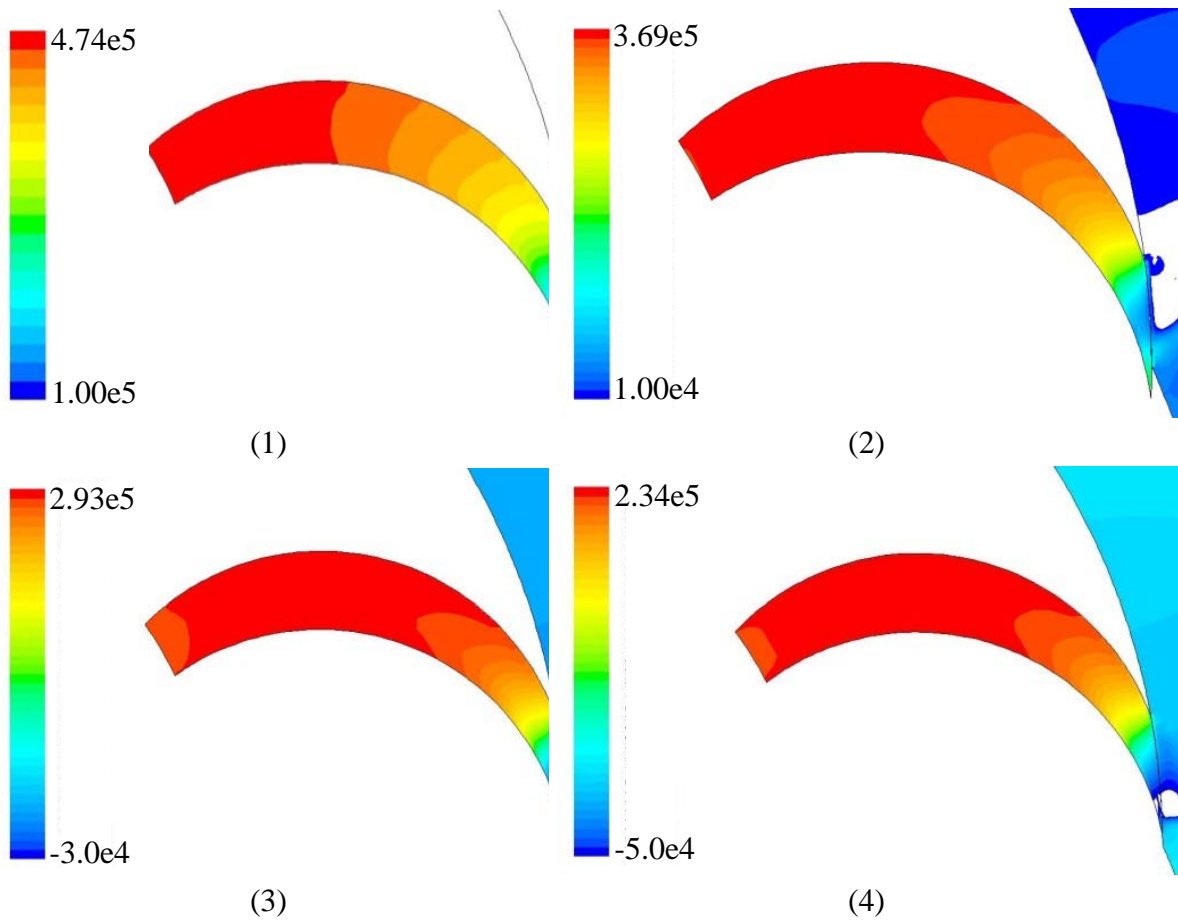
Figure 33: Sequence of the pressure contours when the reflecting wave interferes with the incident wave
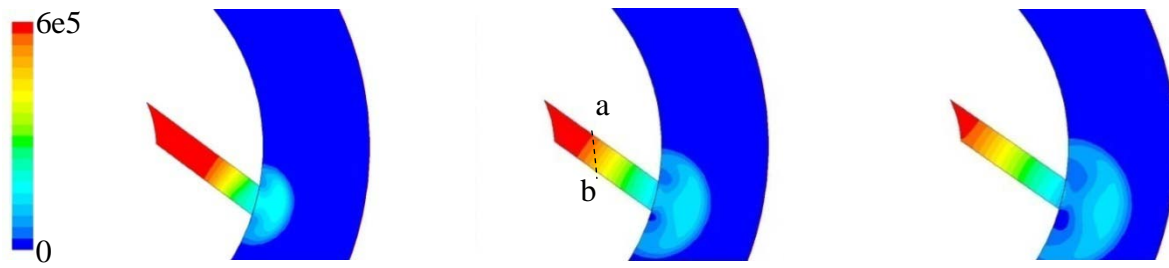
Figure 34: Pressure contours as the expansion wave propagates in a straight channel
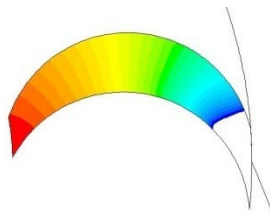
Figure 35: Pressure contour of the C2 channel
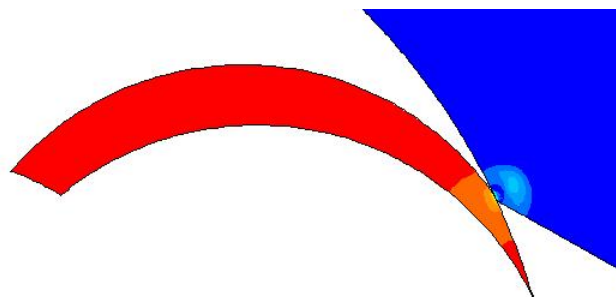
Figure 36: Geometry of the C3 channel
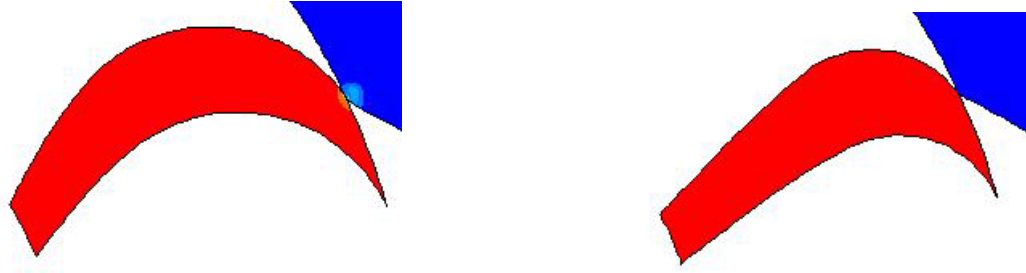
Figure 37: Geometries of J1 (left) and J2 (right) channels
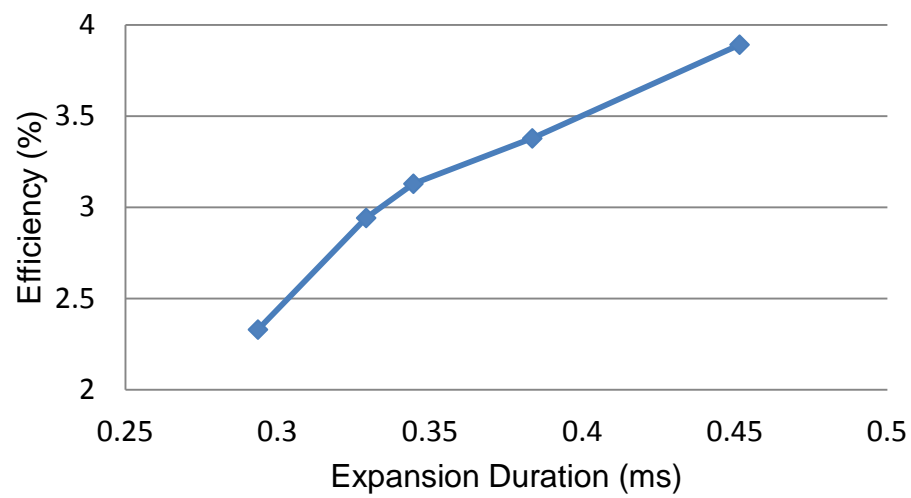
Figure 38: Efficiency vs. expansion duration for C1, C2, C3, J1 and J2 channels
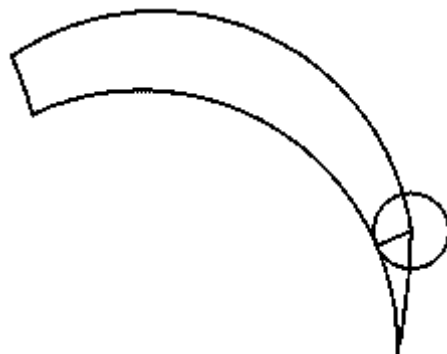
Figure 39: Outlet opening (circle radius)
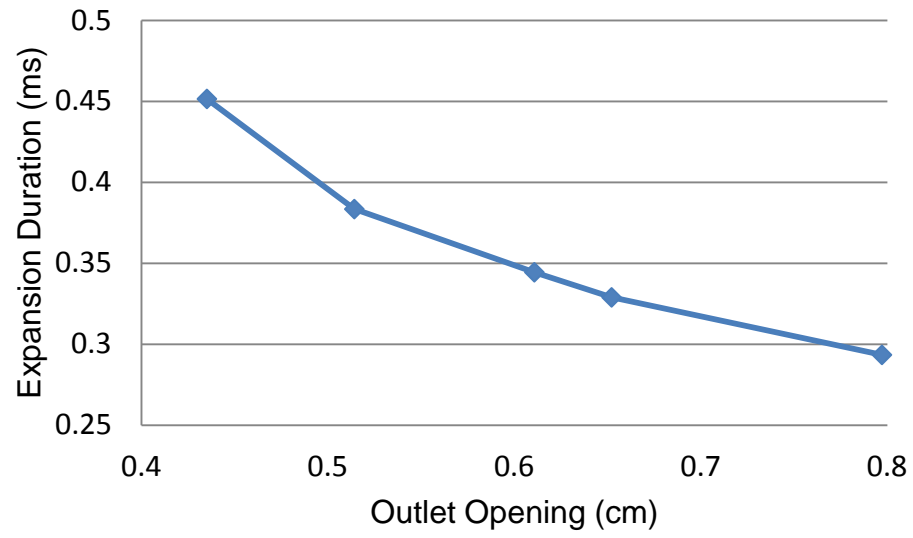
Figure 40: Expansion duration vs. outlet opening
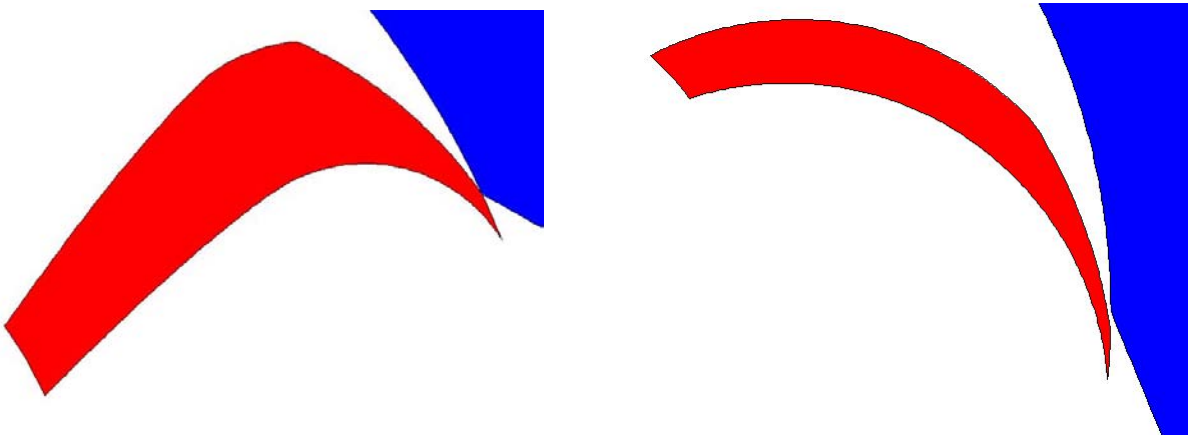
Figure 41: Geometries of the MJ2(left) and MC3(right) channels
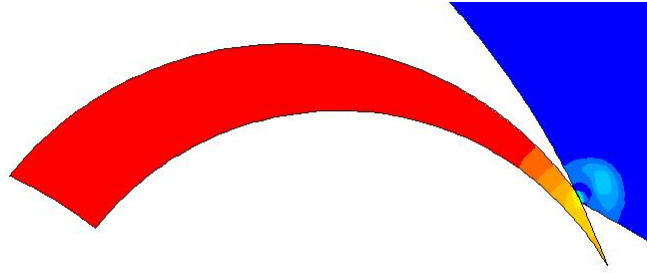
Figure 42: Geometry of the convergent channel
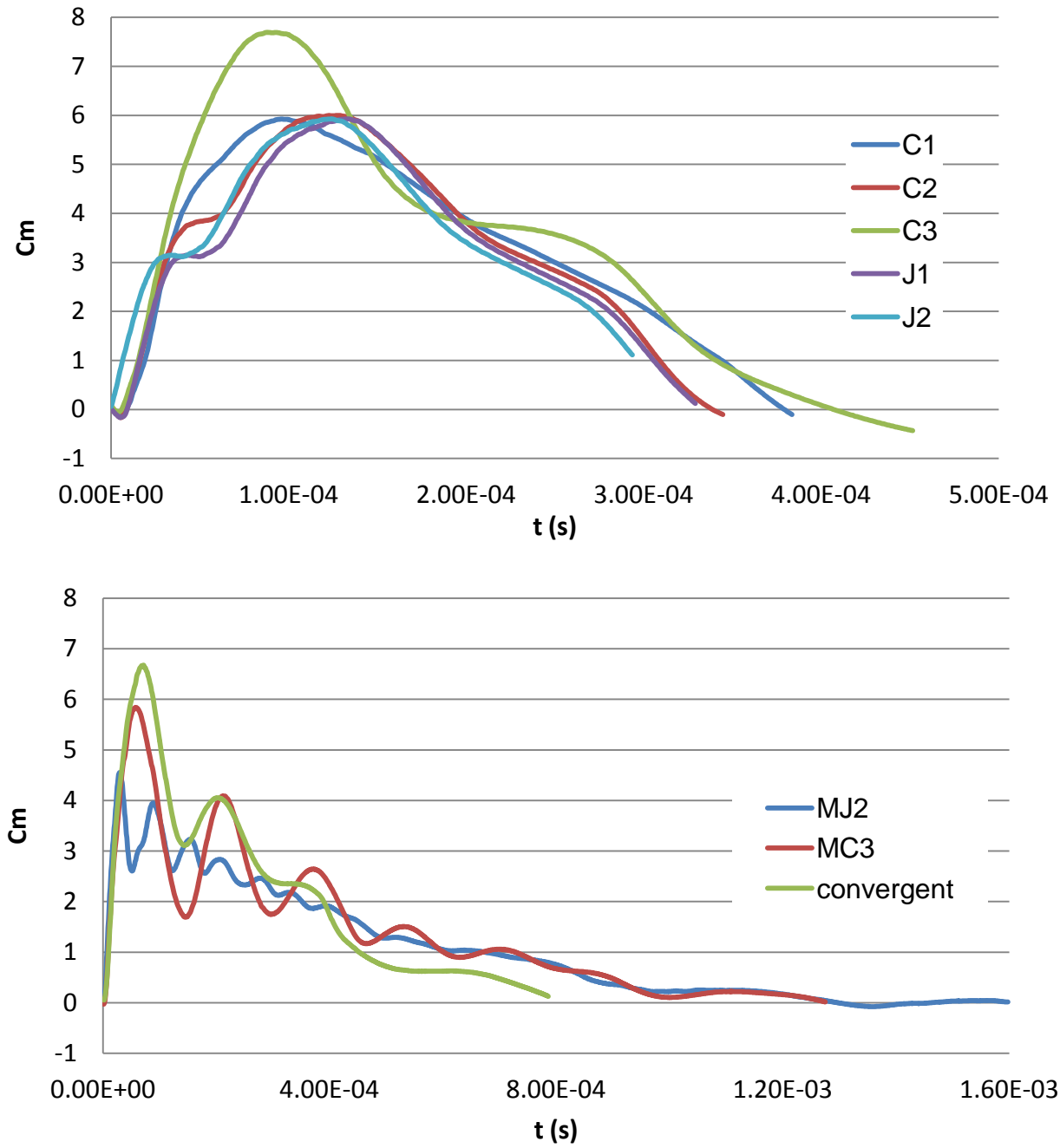
Figure 43: Torque histories of five short expansion cases (upper) and three long expansion cases (lower)
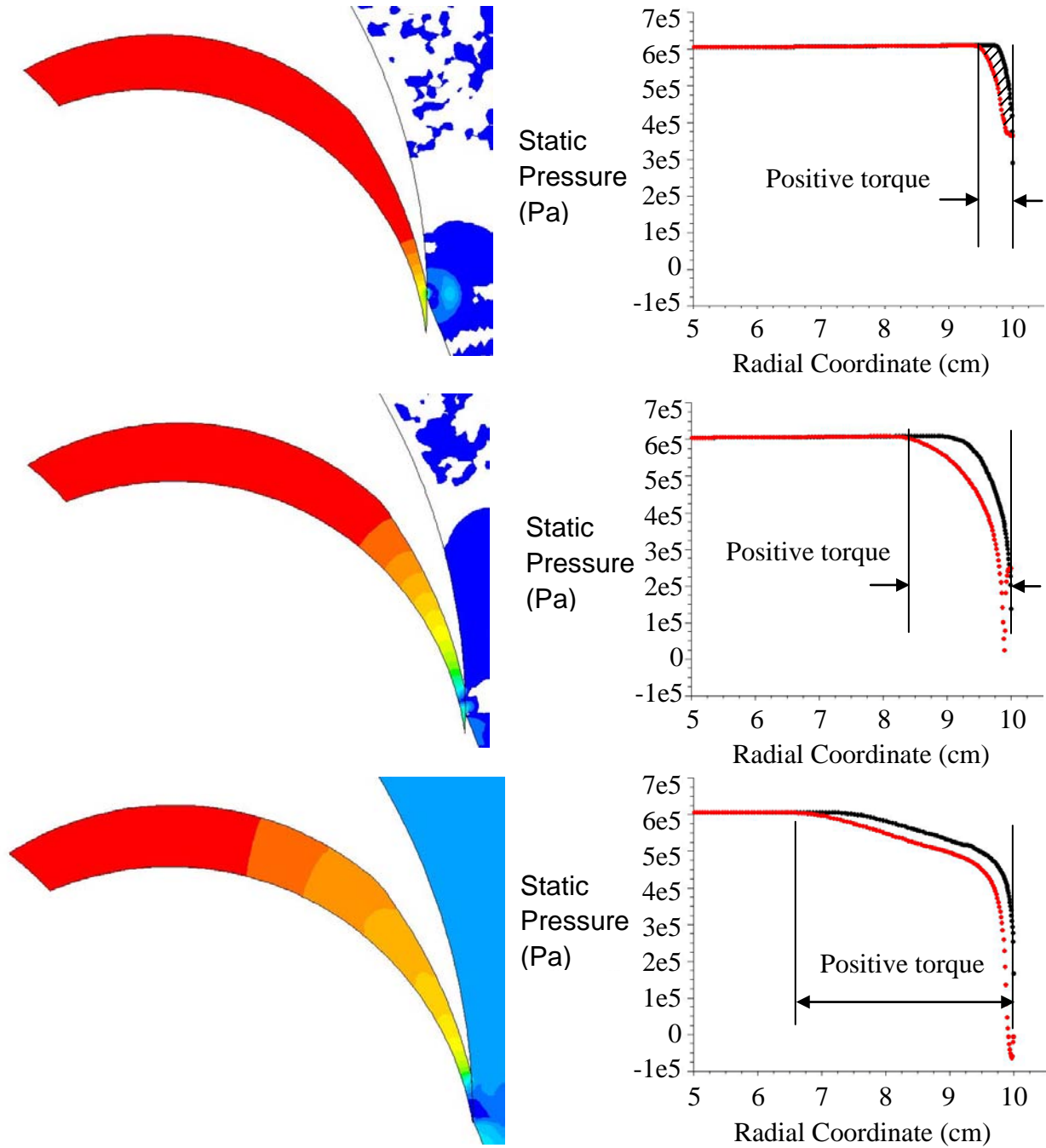
Figure 44: Sequences of the pressure contour (left)and the pressure distribution (right) on the pressure surface (black) and suction surface (red) showing the propagation of the incident expansion wave
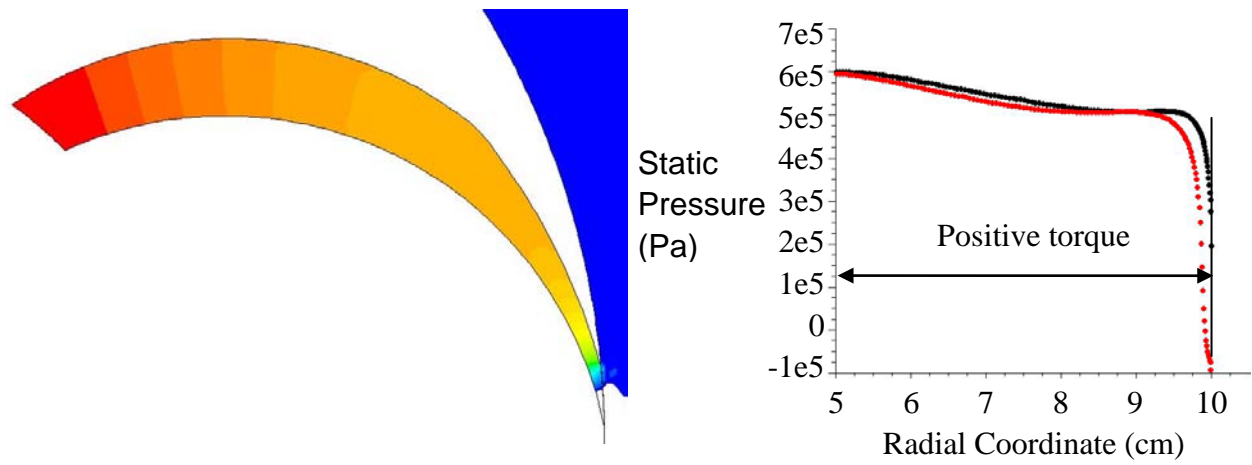
Figure 44 Con't
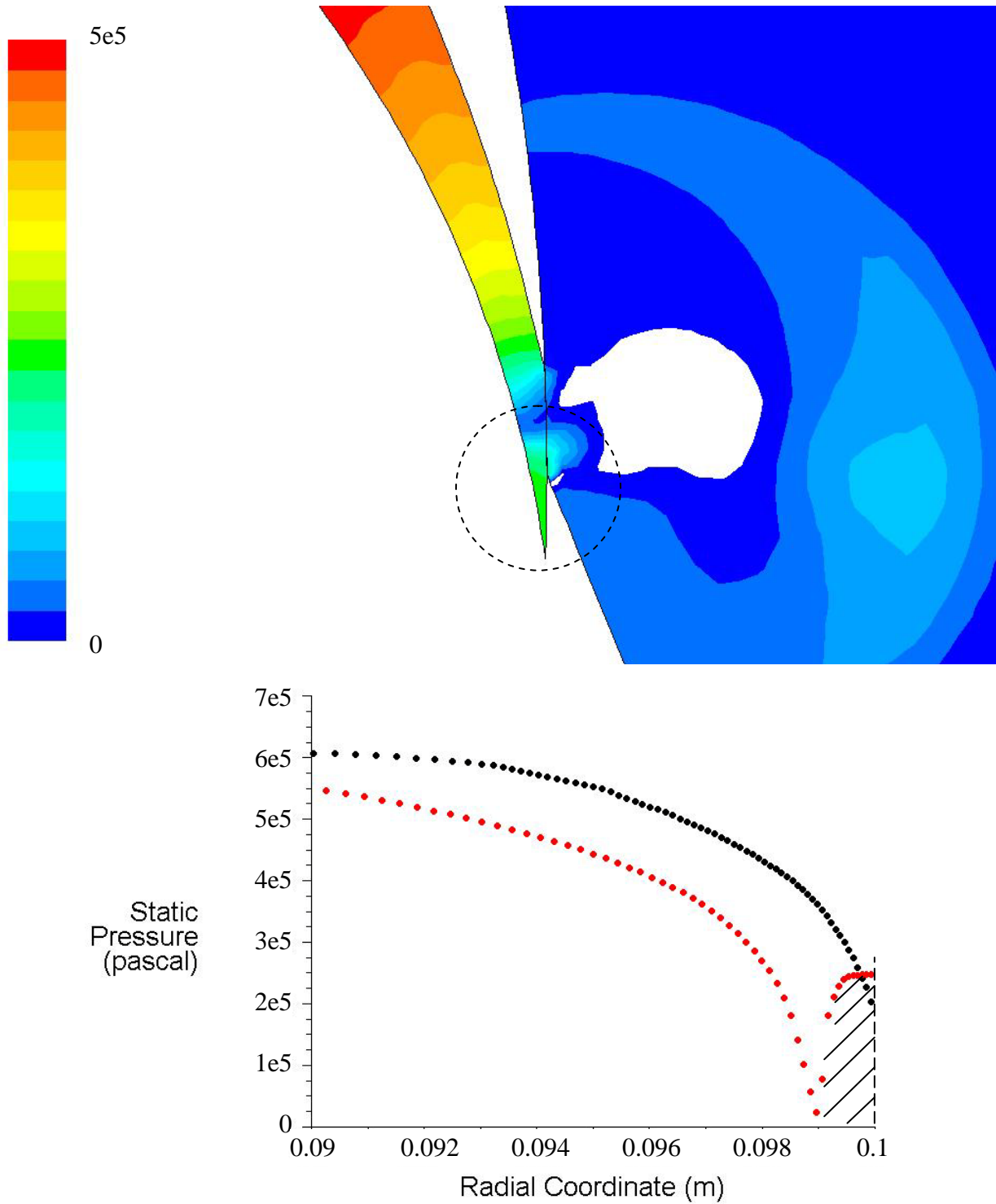
Figure 45: Pressure contour (top) and pressure profiles (bottom) near the trailing edge of the channel walls when the channel outlet is not fully open
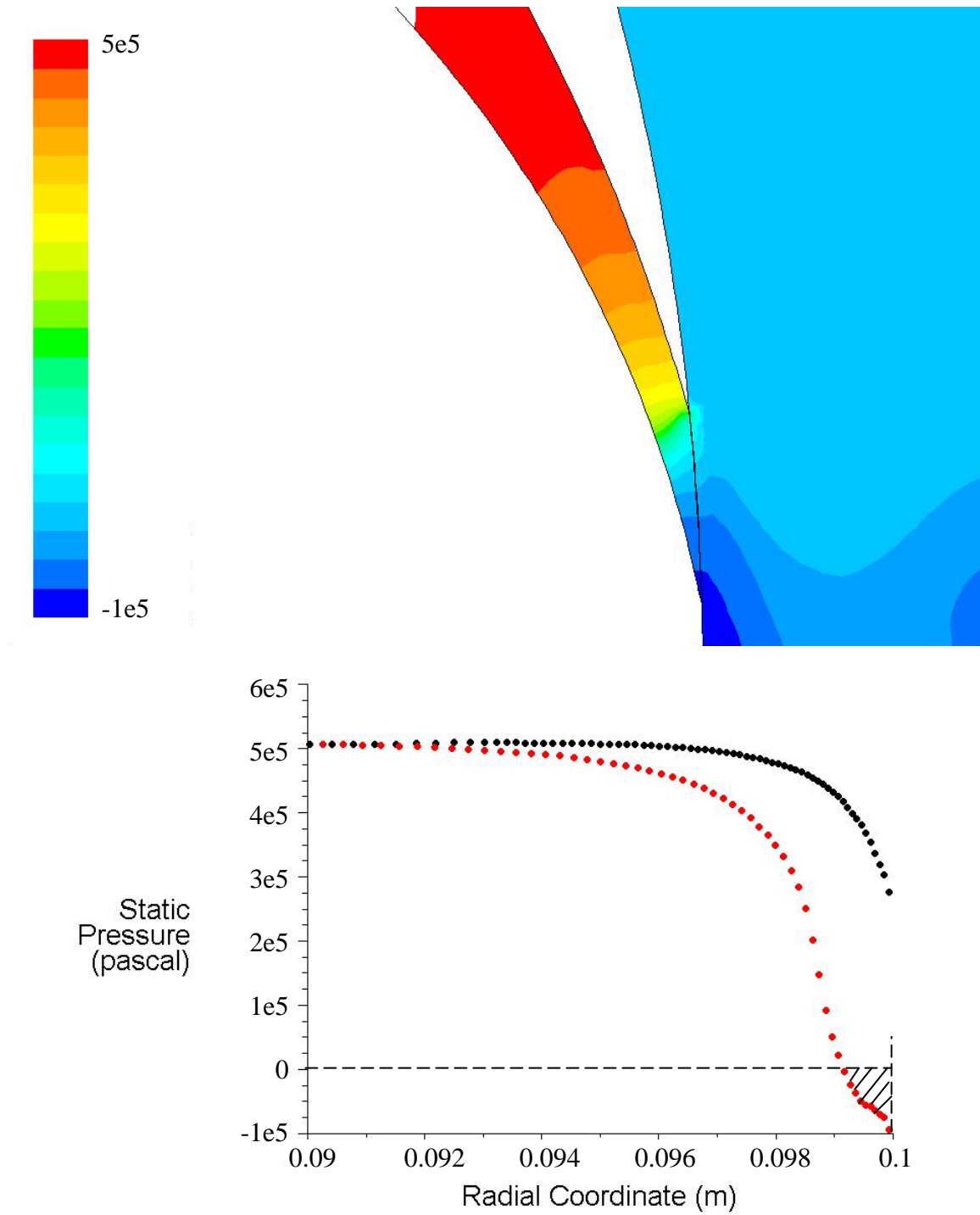
Figure 46: Pressure contour (top), pressure profiles (middle) and Mach number contour near the trailing edge when the channel outlet is fully open
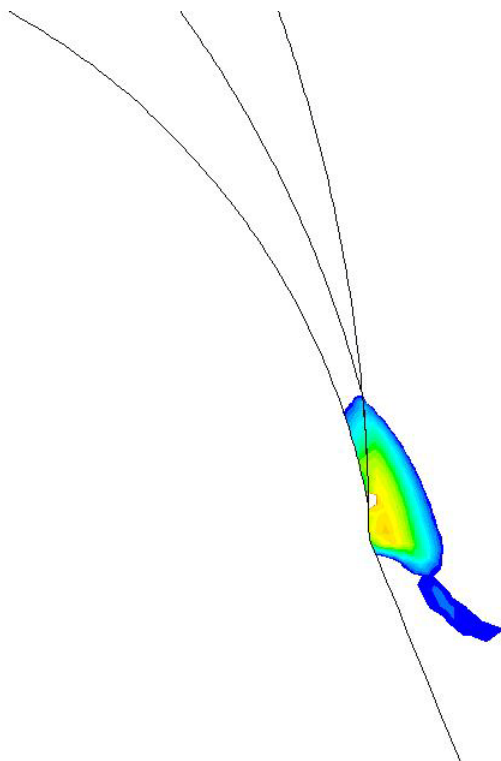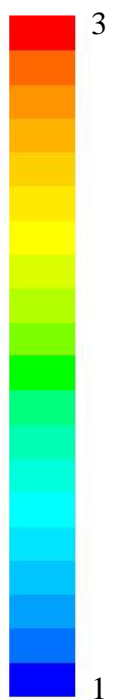
Figure 46 Con't
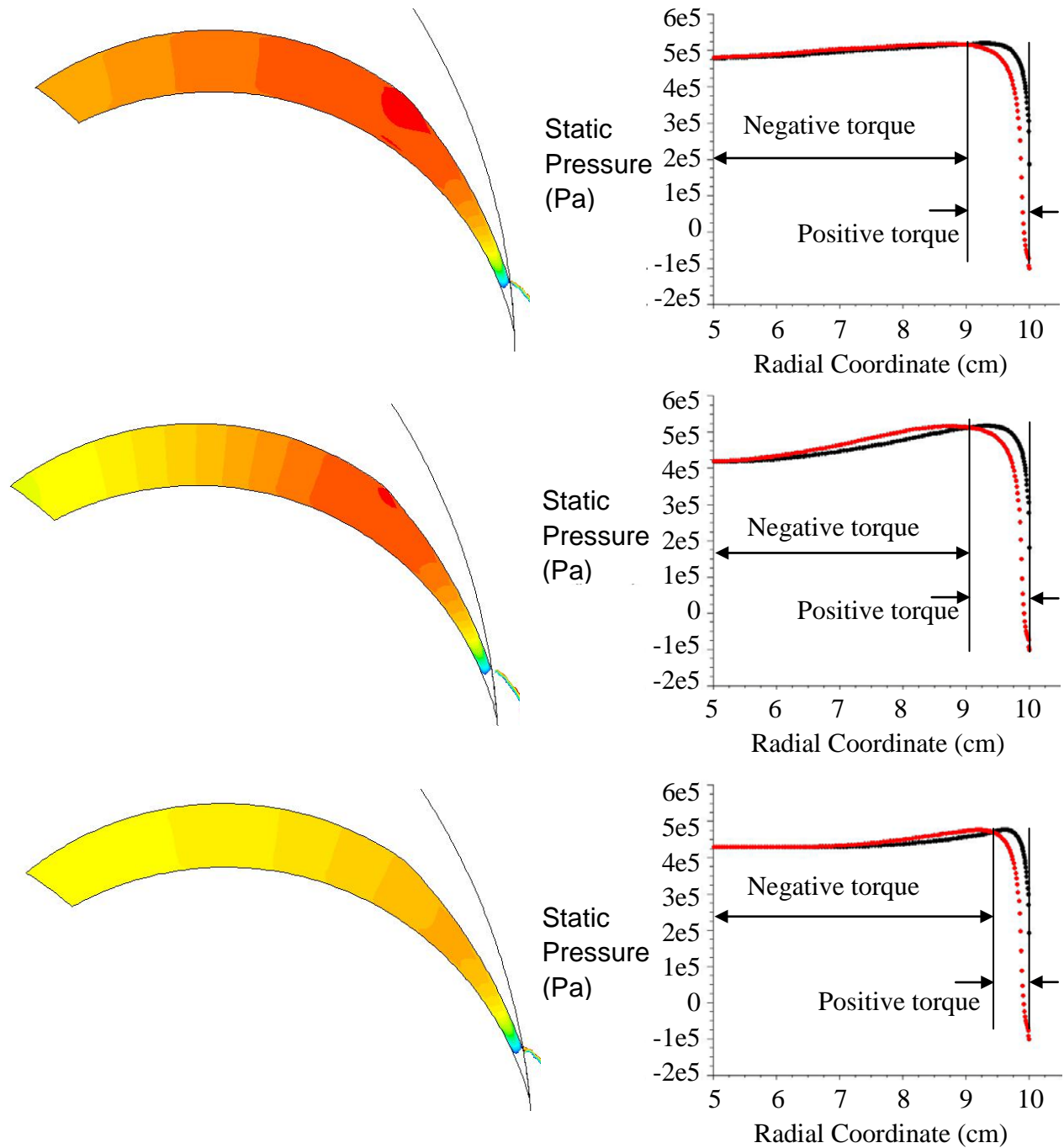
Figure 47: Sequences of the pressure contour (left)and the pressure distribution (right) on the pressure surface (black) and suction surface (red) showing the propagation of the reflected expansion wave
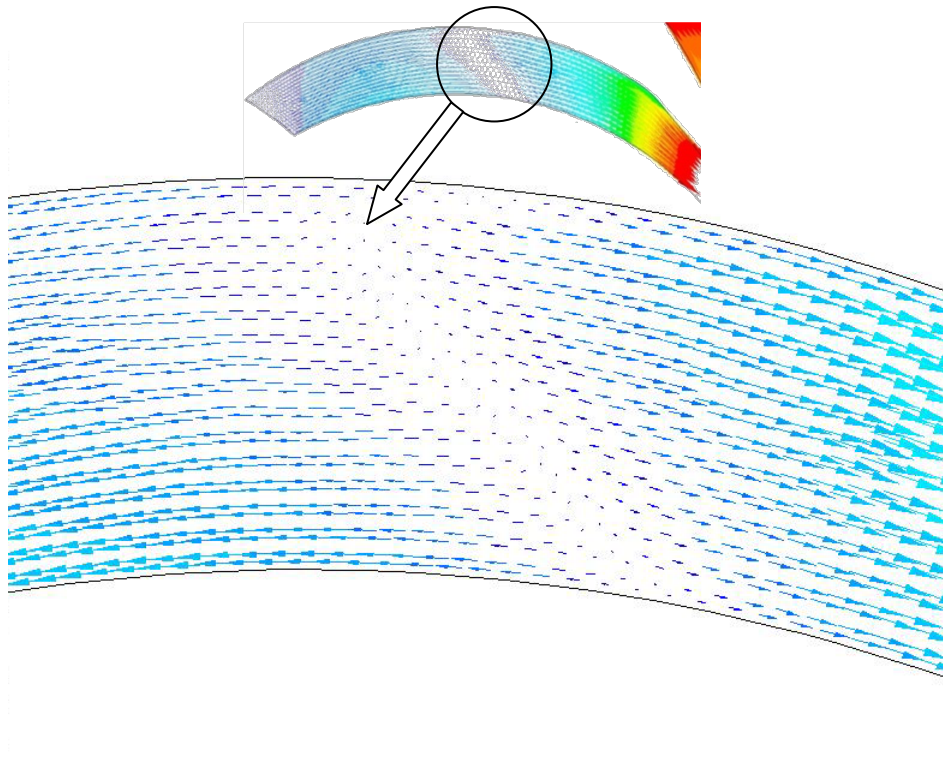
Figure 48: Relative velocity vectors showing the back flow near the inlet end
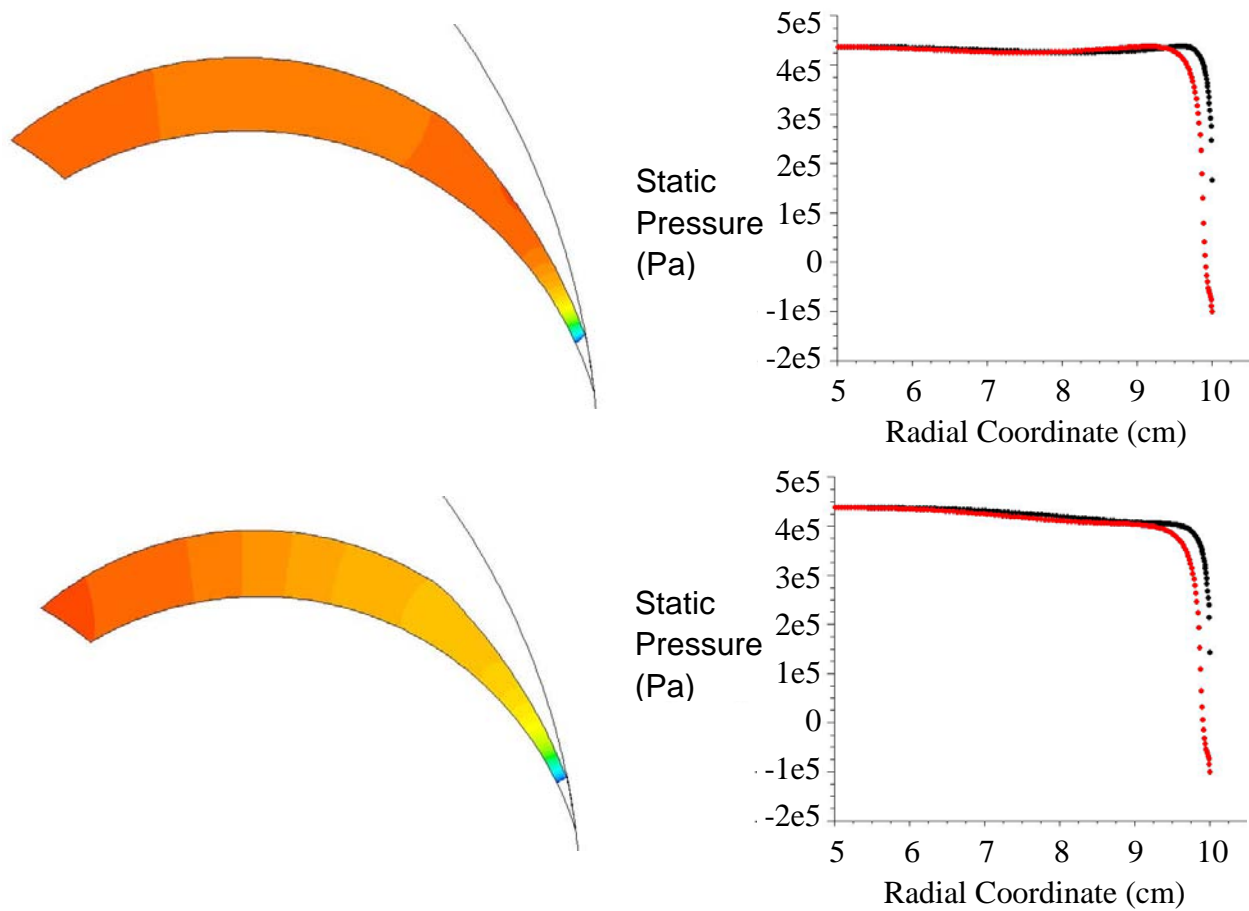
Figure 49: Sequences of the pressure contour (left)and the pressure distribution (right) on the pressure surface (black) and suction surface (red) showing the positive pressure gradient caused by the back flow near the inlet
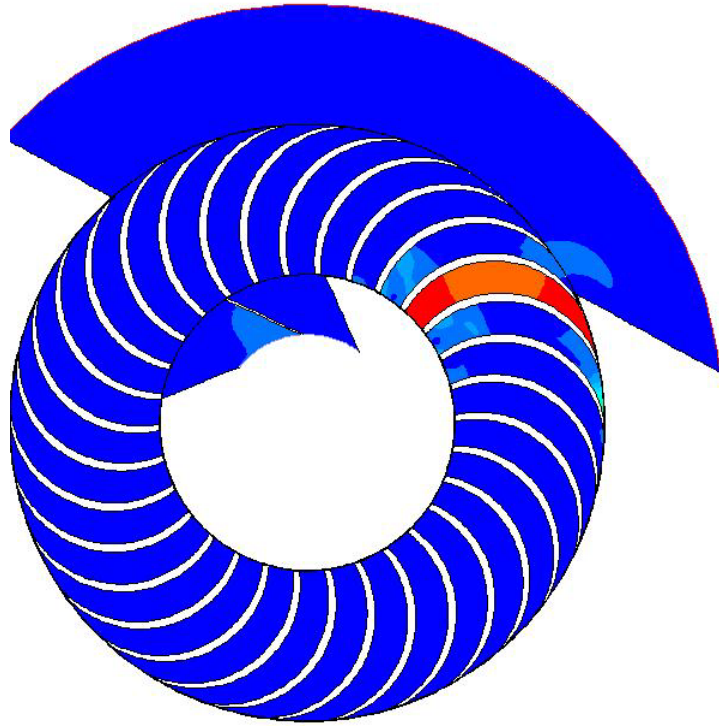
Figure 50: Pressure contour in the beginning of the simulation
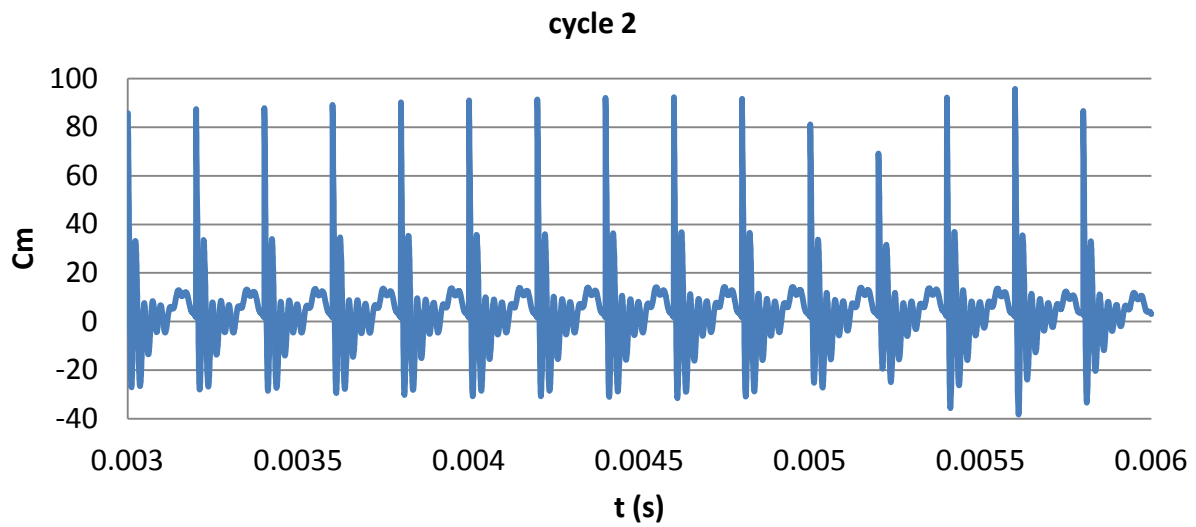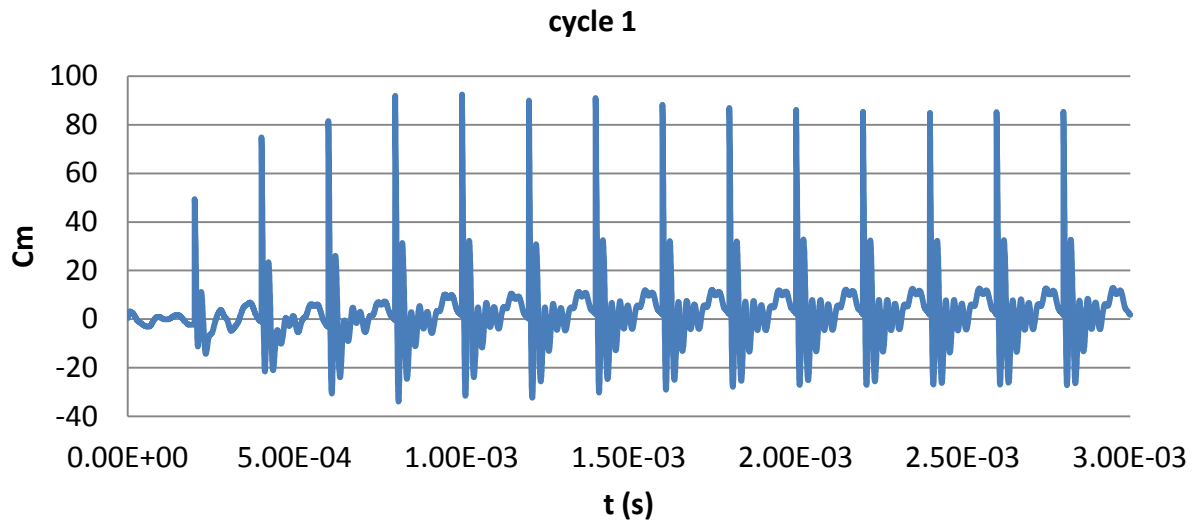
Figure 51: Torque histories of the first three cycles
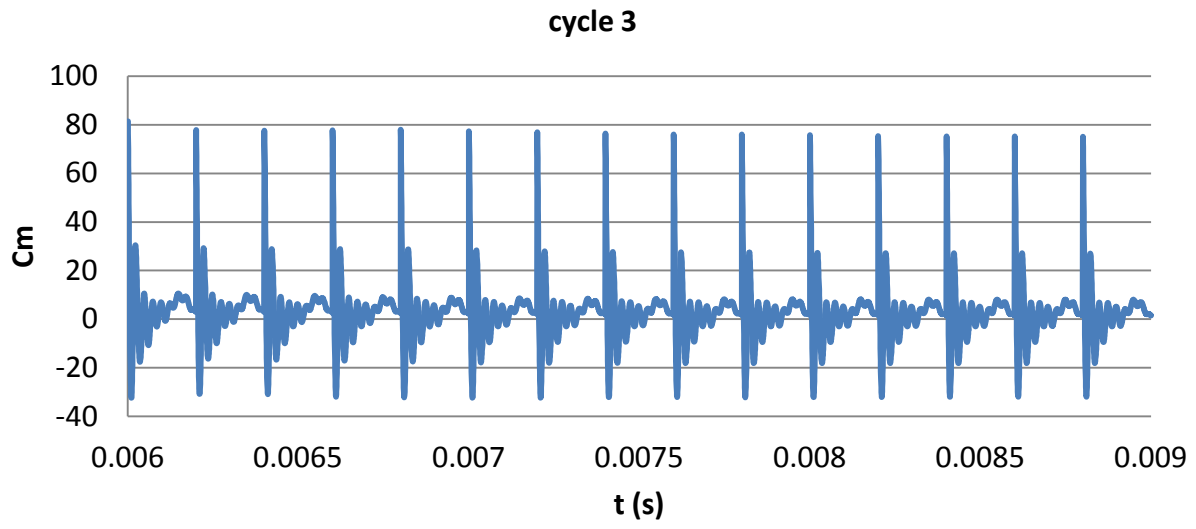
cycle 3

Figure 51 Con't
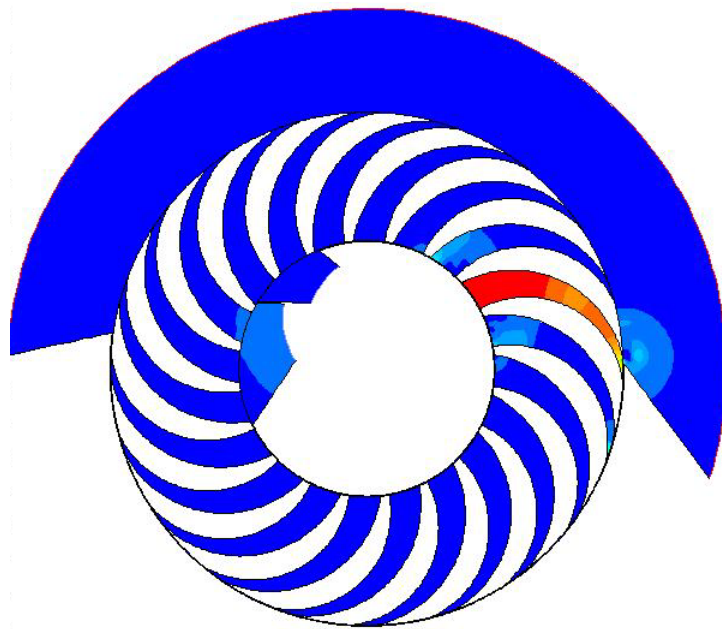
Figure 52: Geometry of the single rotor engine with convergent channels
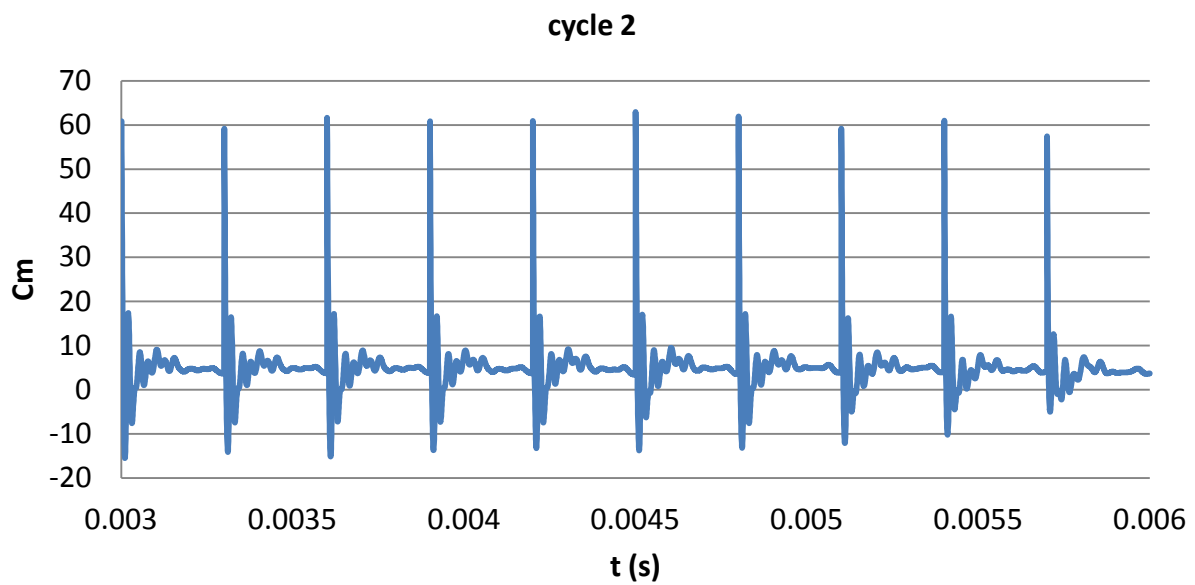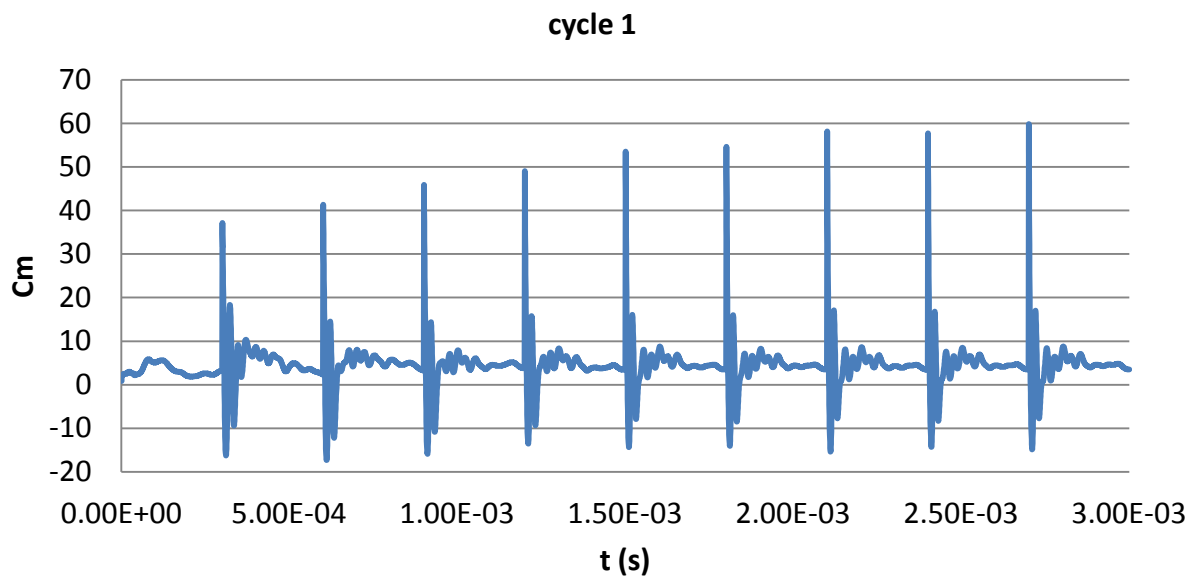
Figure 53: Histories of torque of the first two cycles
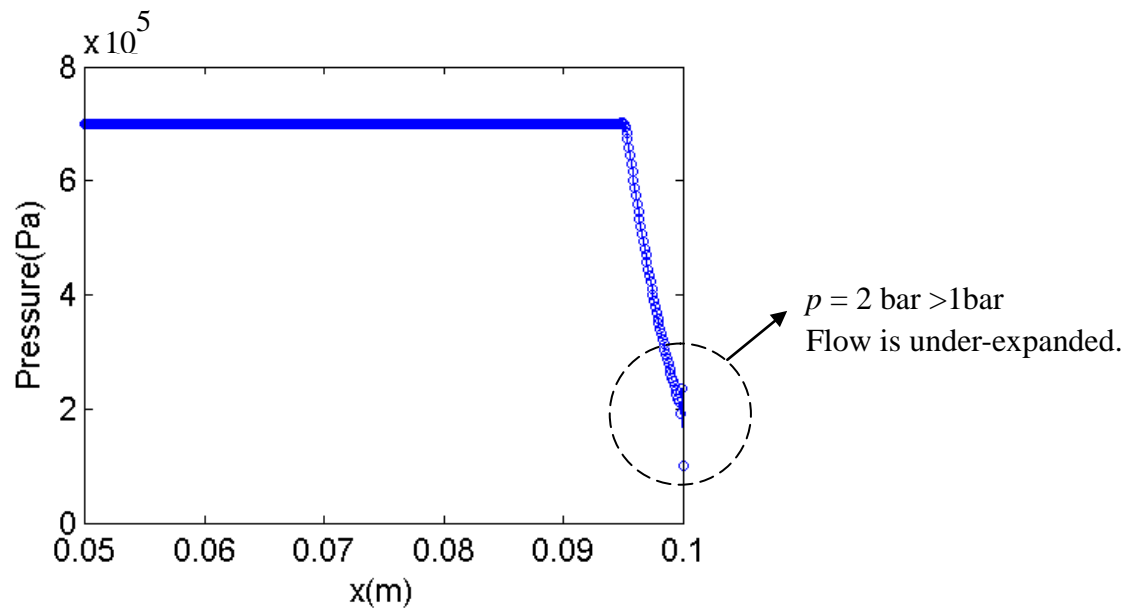
Figure 54: Profile of pressure in case 1 when the incident expansion propagates
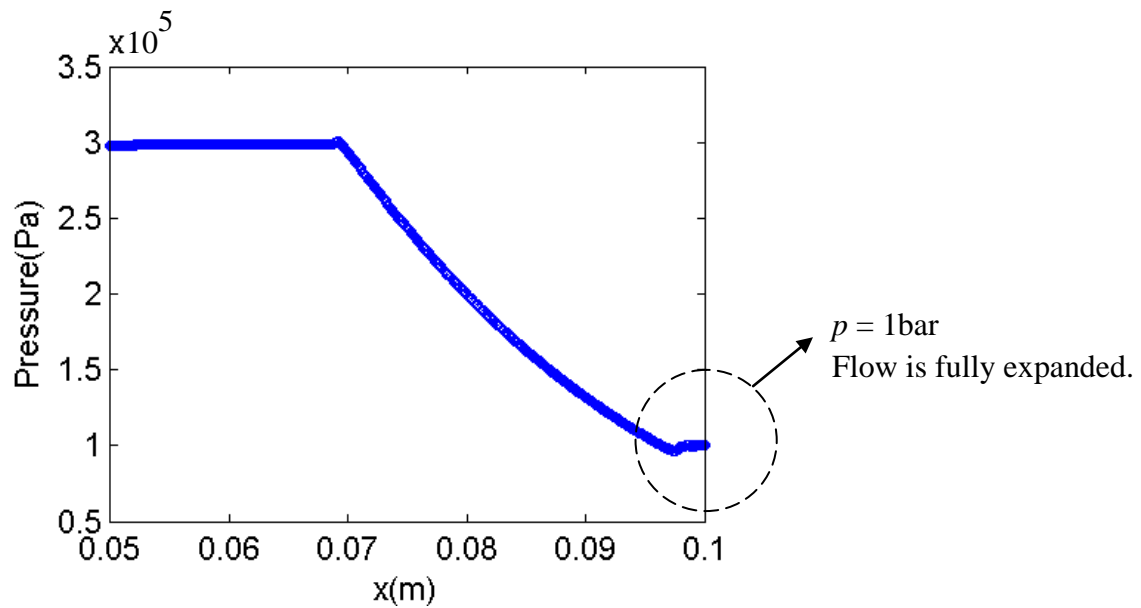
Figure 55: Profile of pressure in case 2 when the incident expansion propagates
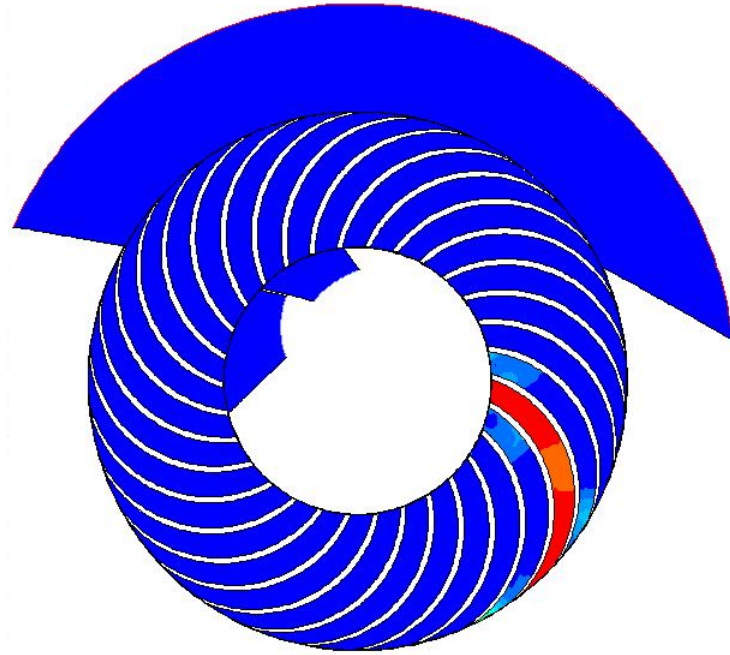
Figure 56: WDE with C3 channels
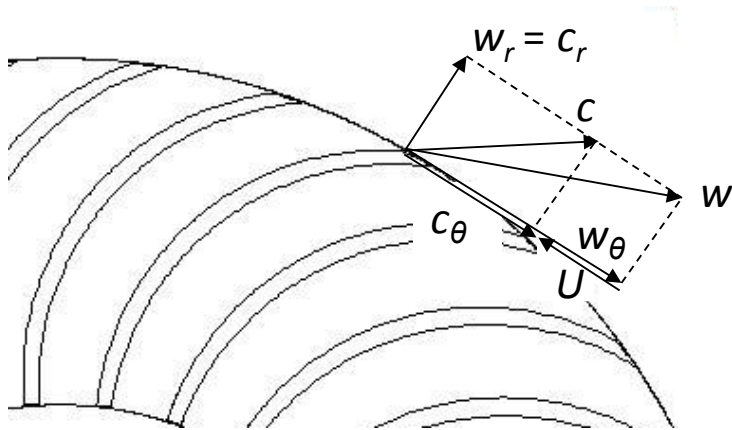
Figure 57: Velocity triangle at the trailing edge of a channel wall
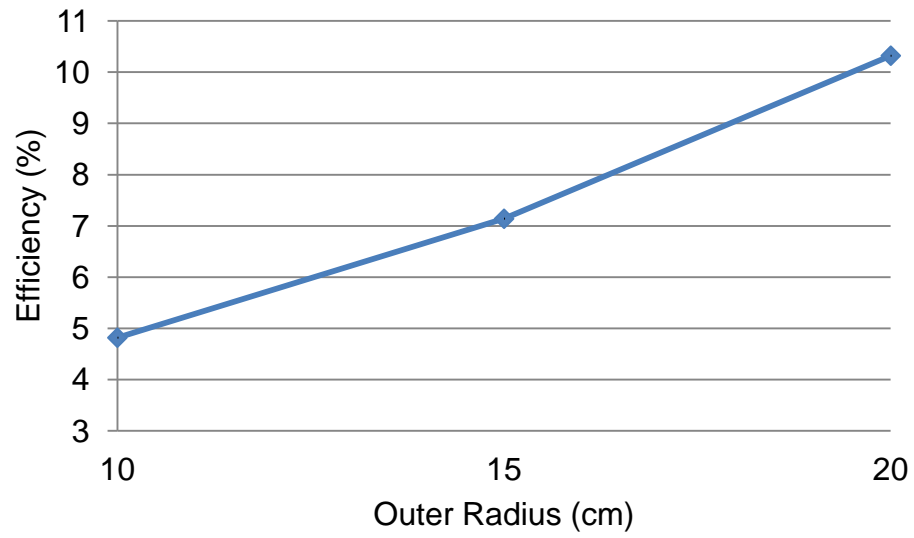
Figure 58: Efficiency vs. outer radius
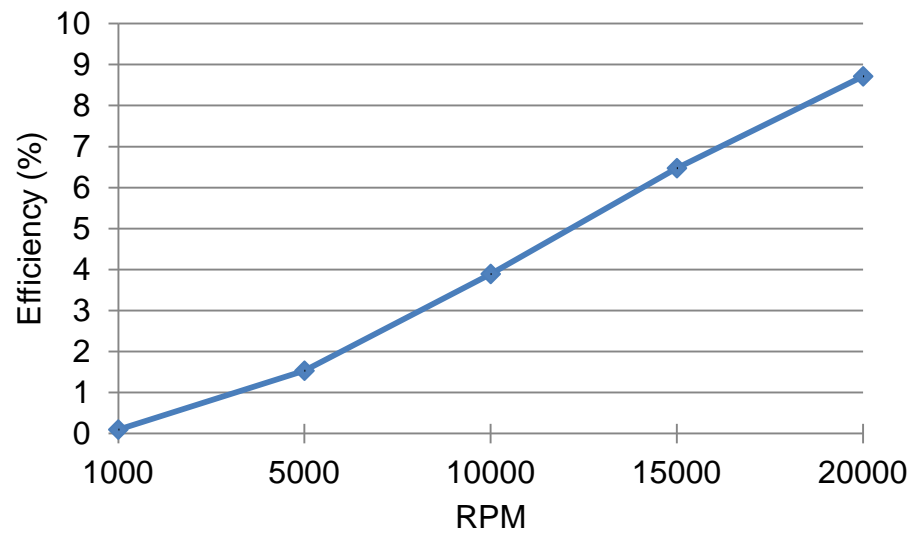
Figure 59: Efficiency vs. RPM
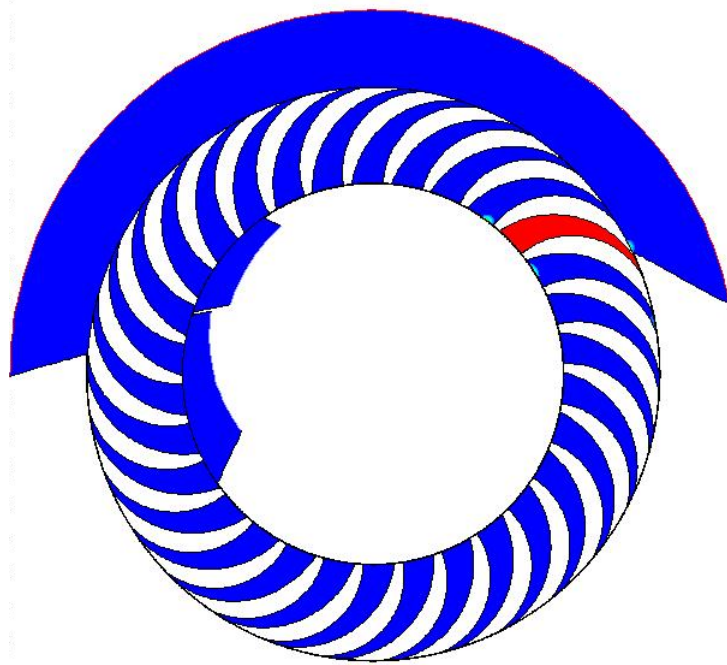
Figure 60: Geometry of the engine with 30 cm OD
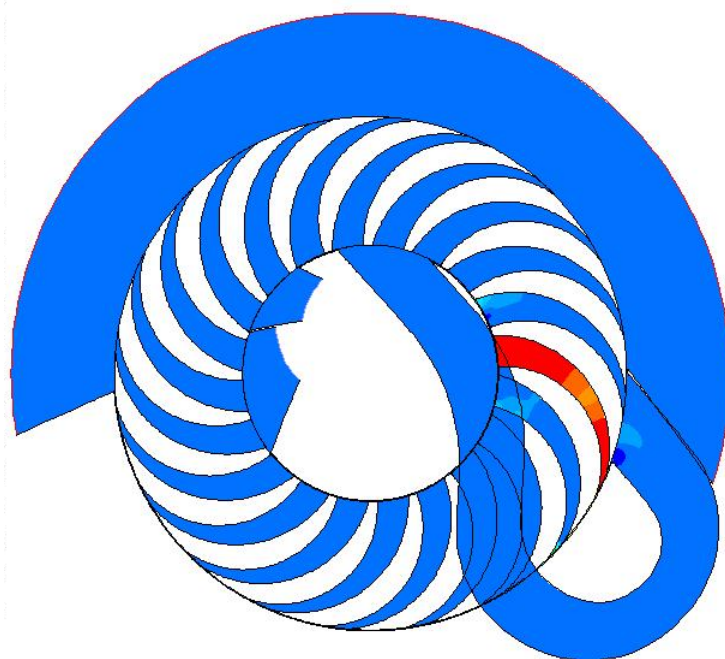
Figure 61: WDE with a return channel
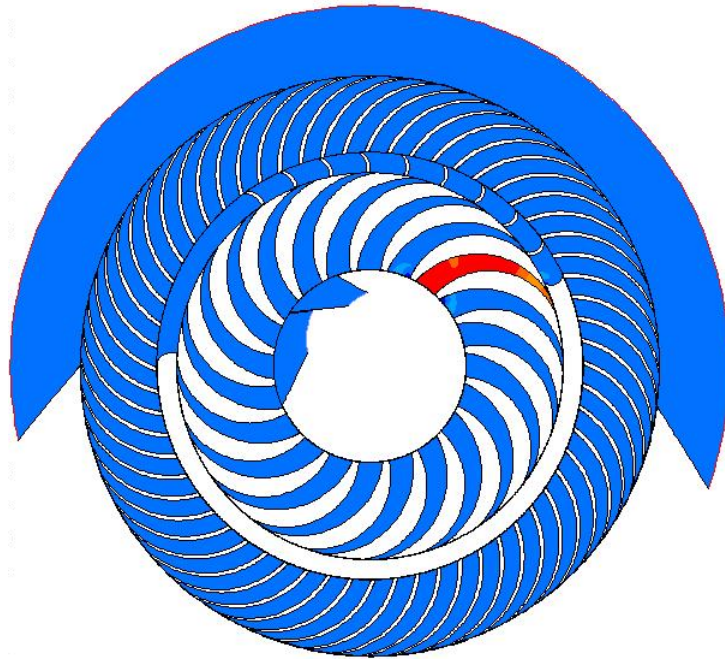
Figure 62: Configuration of a two-stage engine
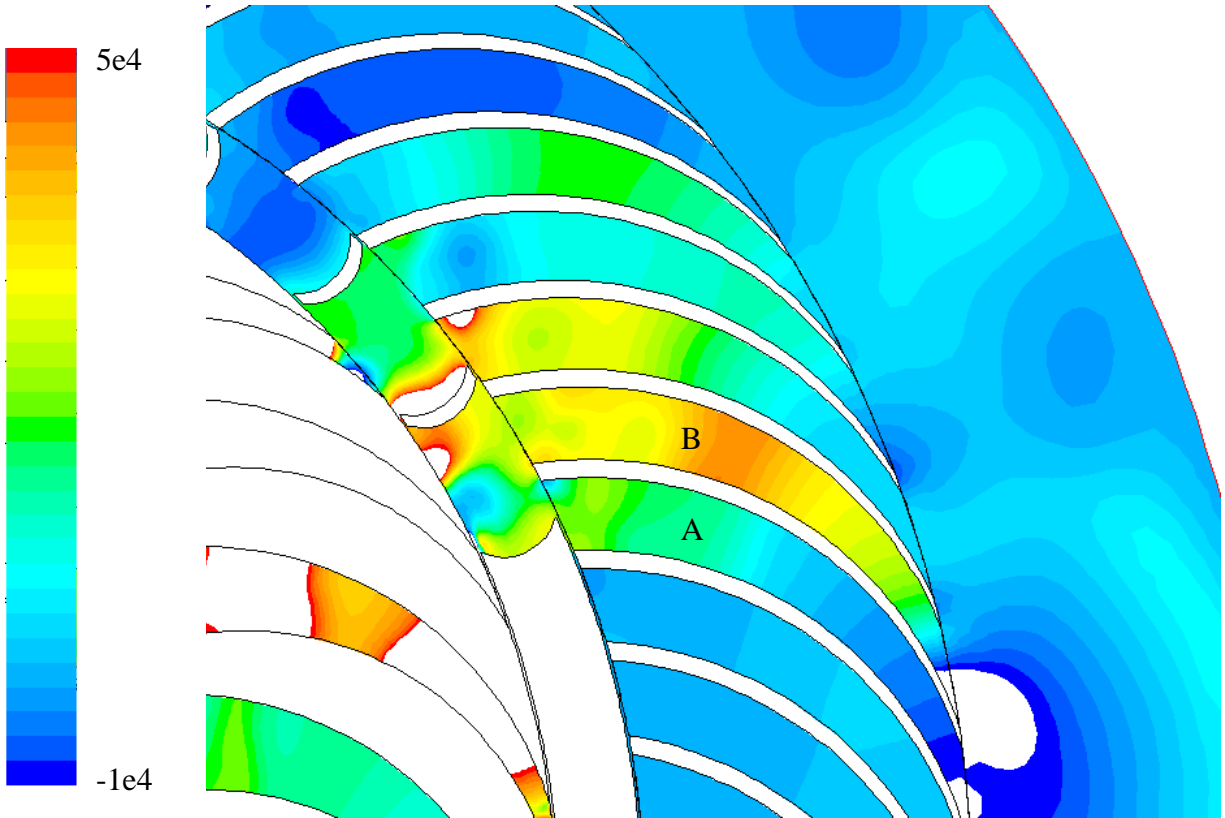
Figure 63: Pressure contour in the external turbine
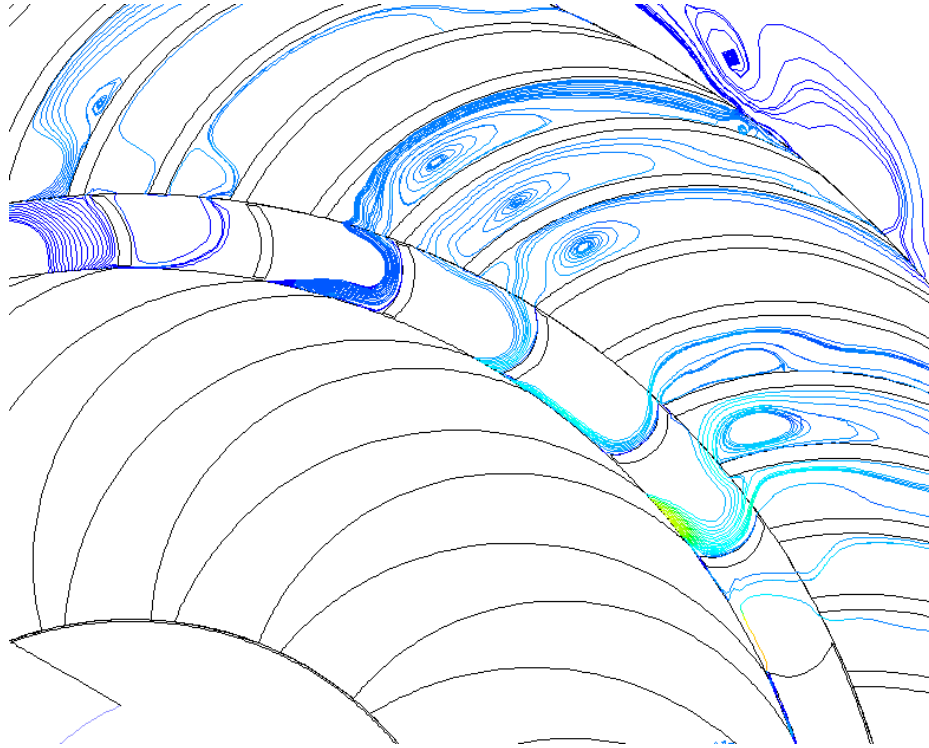
Figure 64: Streamlines in the guide vane passage
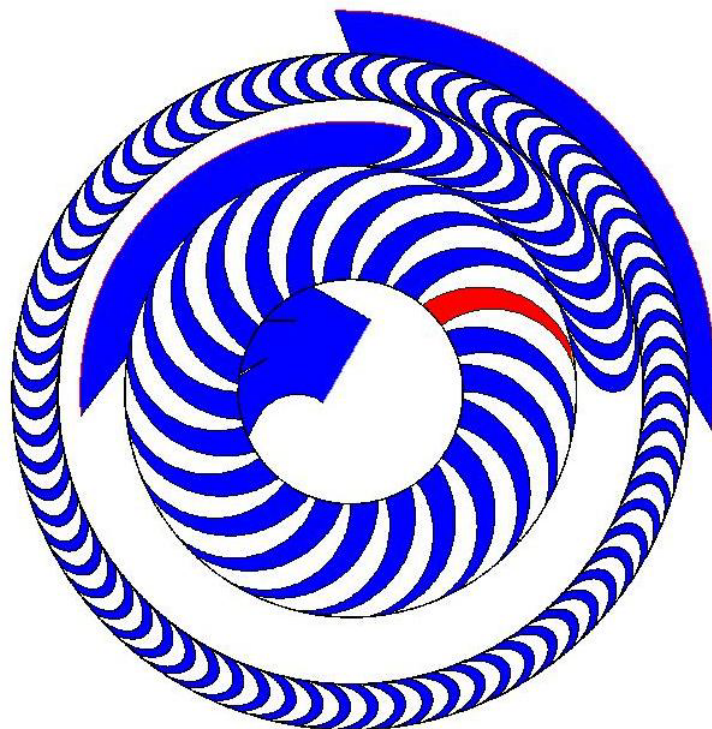
Figure 65: Configuration of a second generation engine
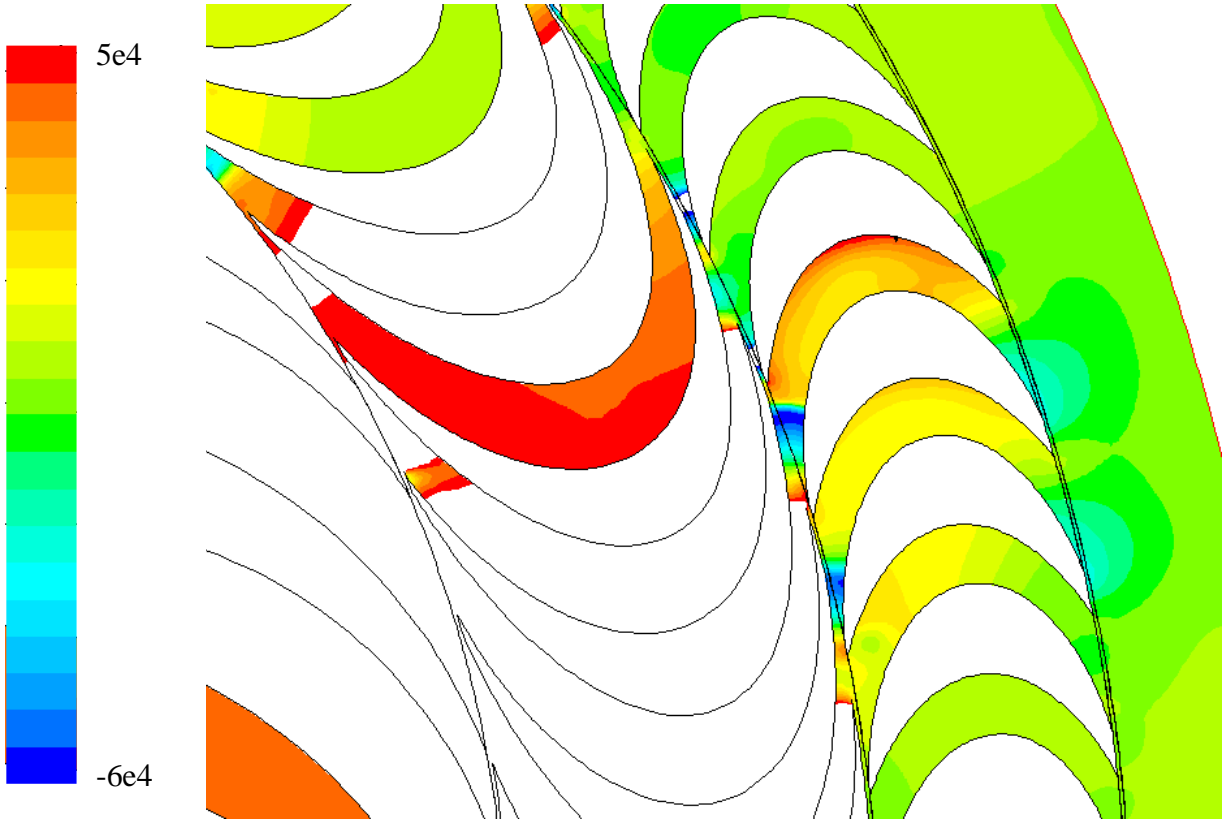
Figure 66: Pressure contour in the blade passages of the second generation engine
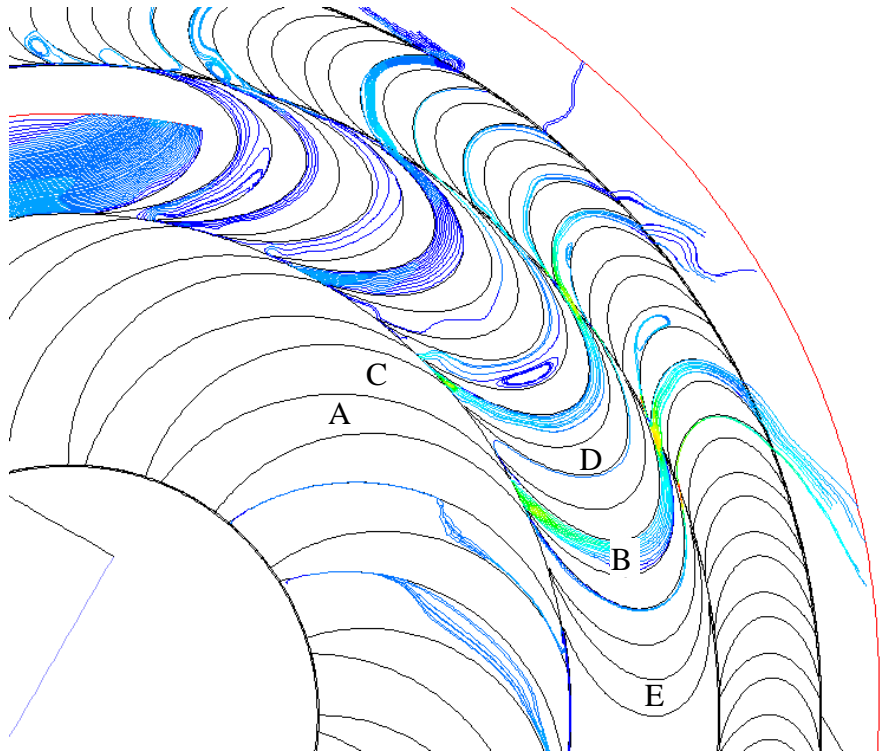
Figure 67: Streamlines in the guide vane passage of the second generation engine
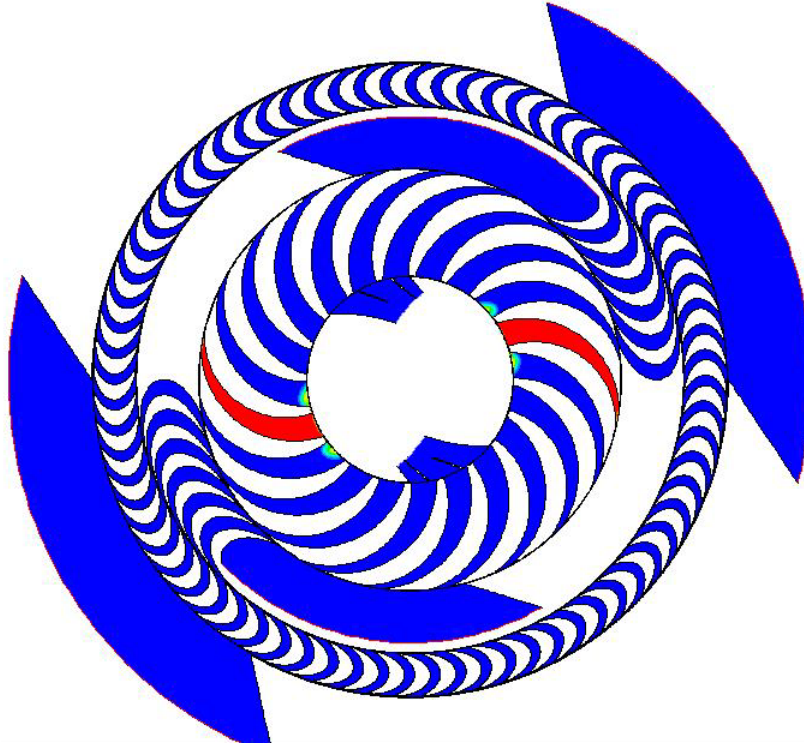
Figure 68: Temperature contour of the no prevention design at 2e-5 s
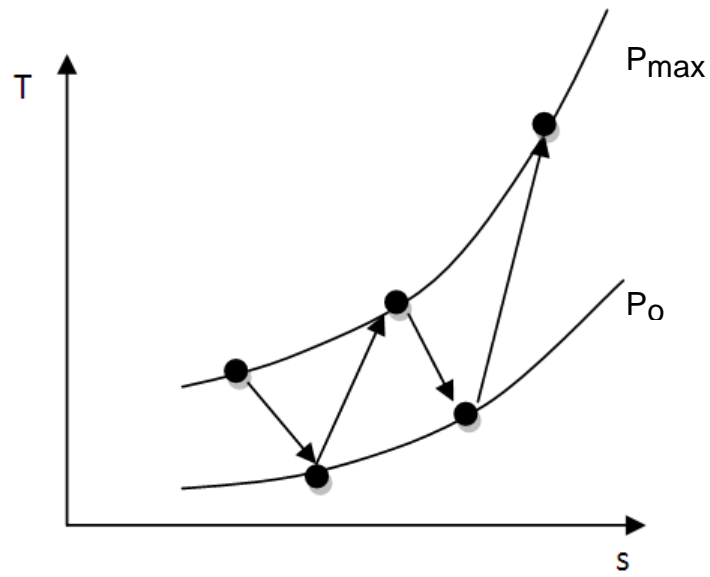
Figure 69: Thermodynamic process of the hot leakage gas
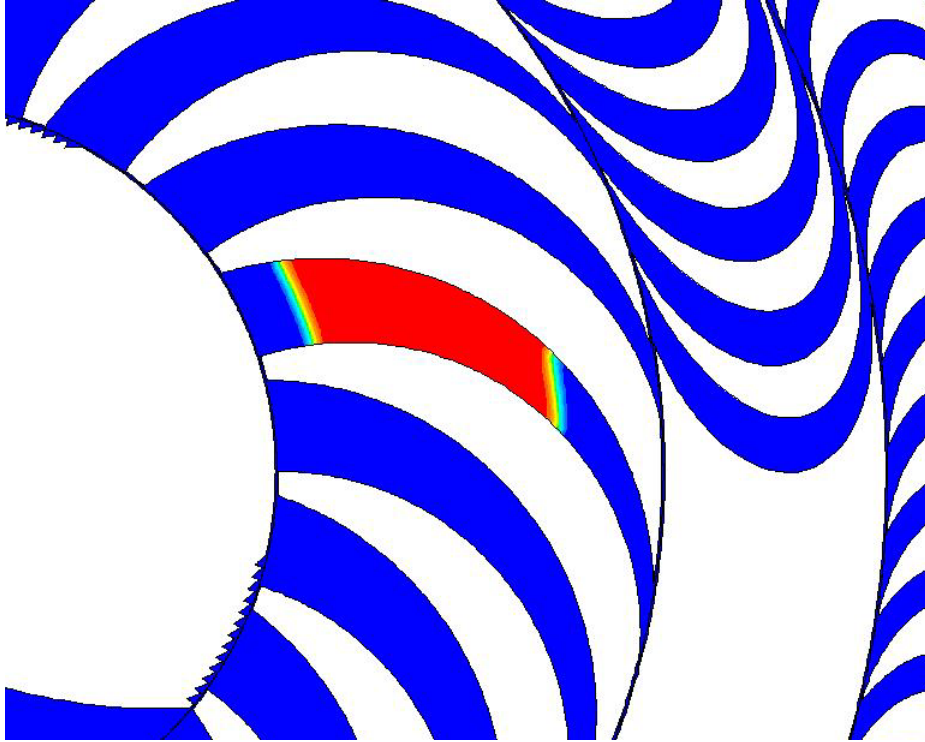
Figure 70: Energy patching area (red area)
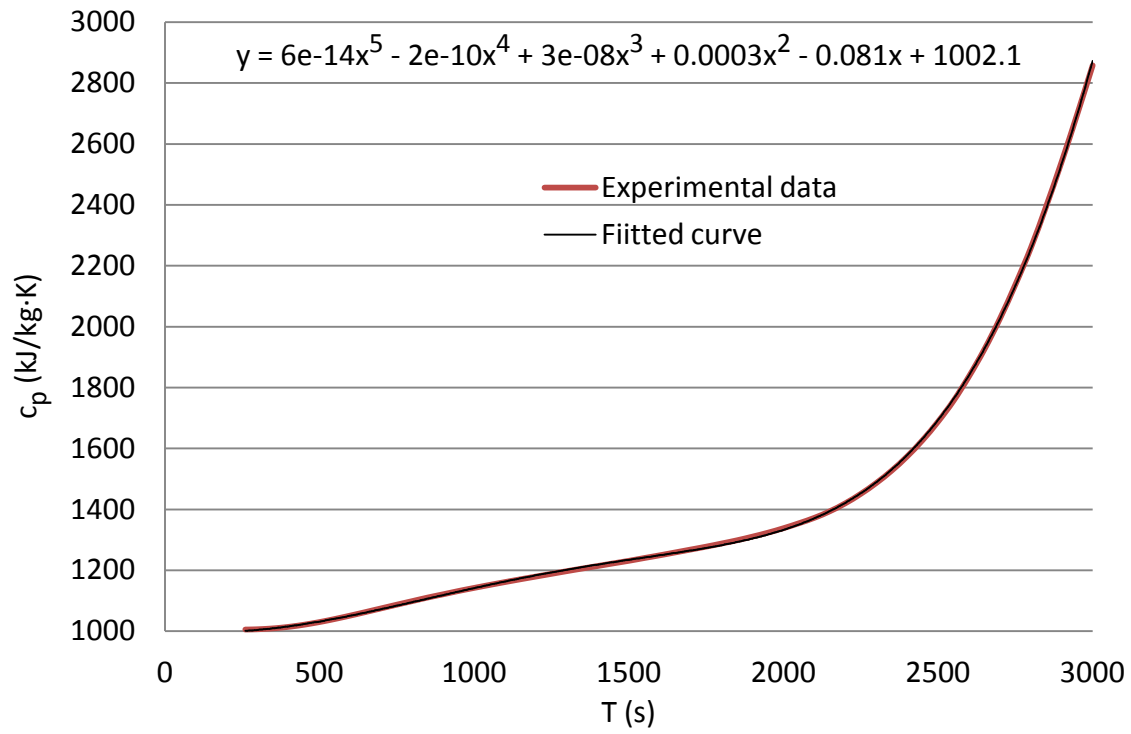
Figure 71: Variation of c_p with T of the experimental data and the fitted curve

The equation shown in the figure:

$$y = 6e\text{-}14x^5 - 2e\text{-}10x^4 + 3e\text{-}08x^3 + 0.0003x^2 - 0.081x + 1002.1$$
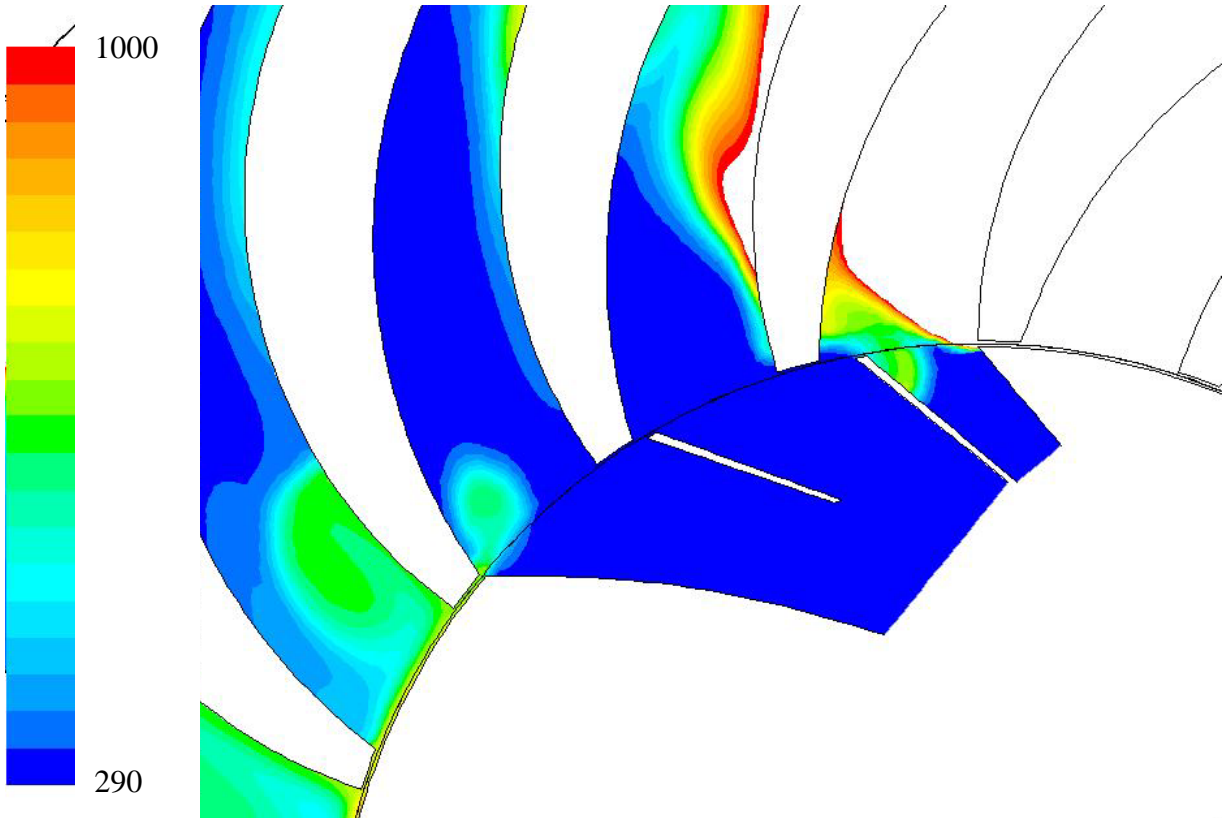
Figure 72: Temperature contour at the end of the third cycle from the pressure patching method for the no prevention design
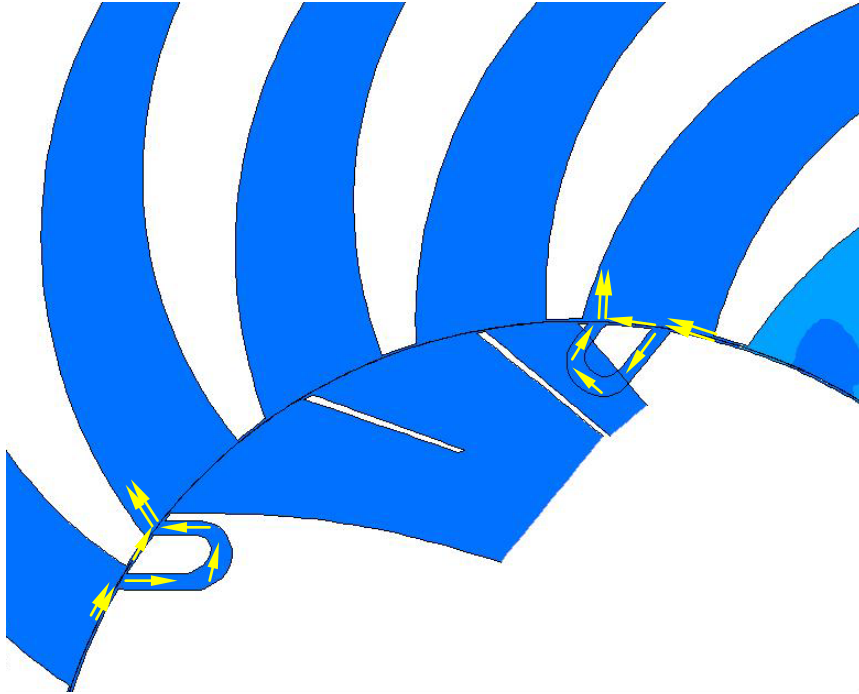
Figure 73: Idea of the U channel
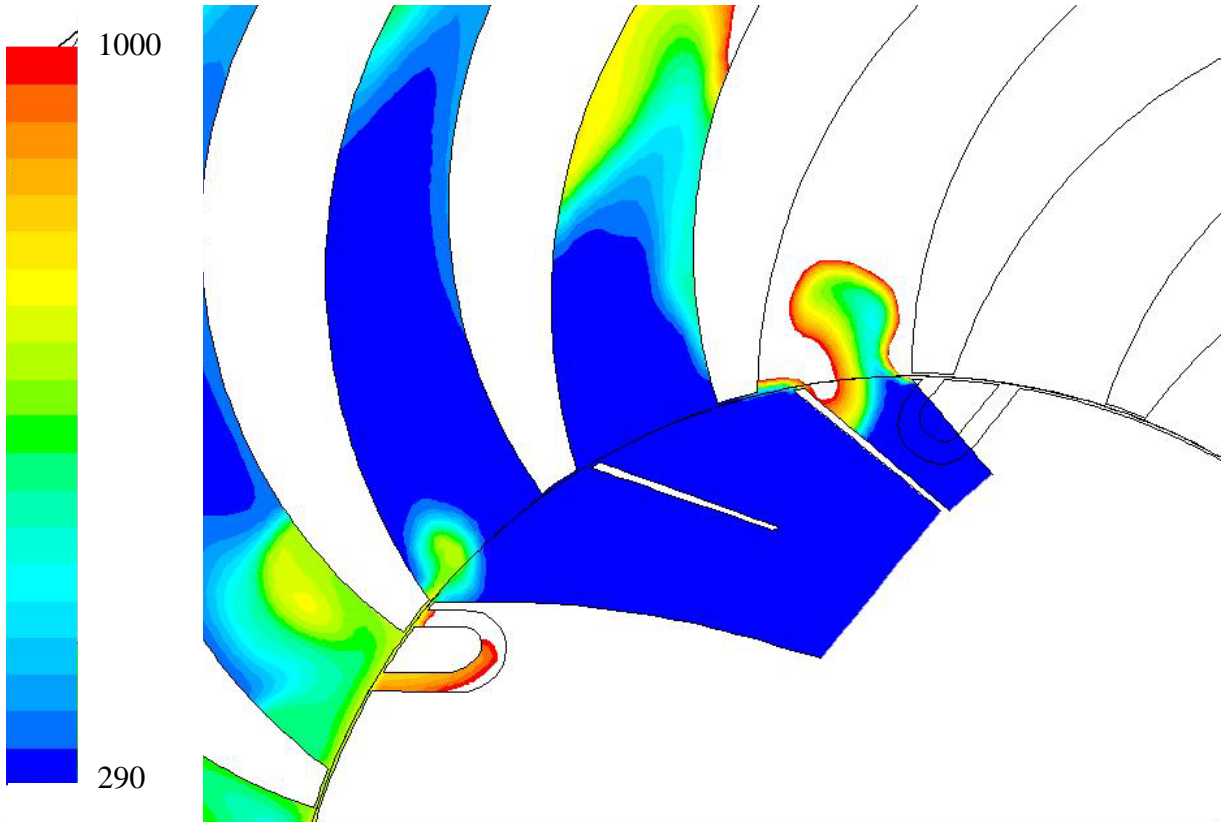
Figure 74: Temperature contour at the end of the third cycle from the pressure patching method for the U channel design

(1)   (2)
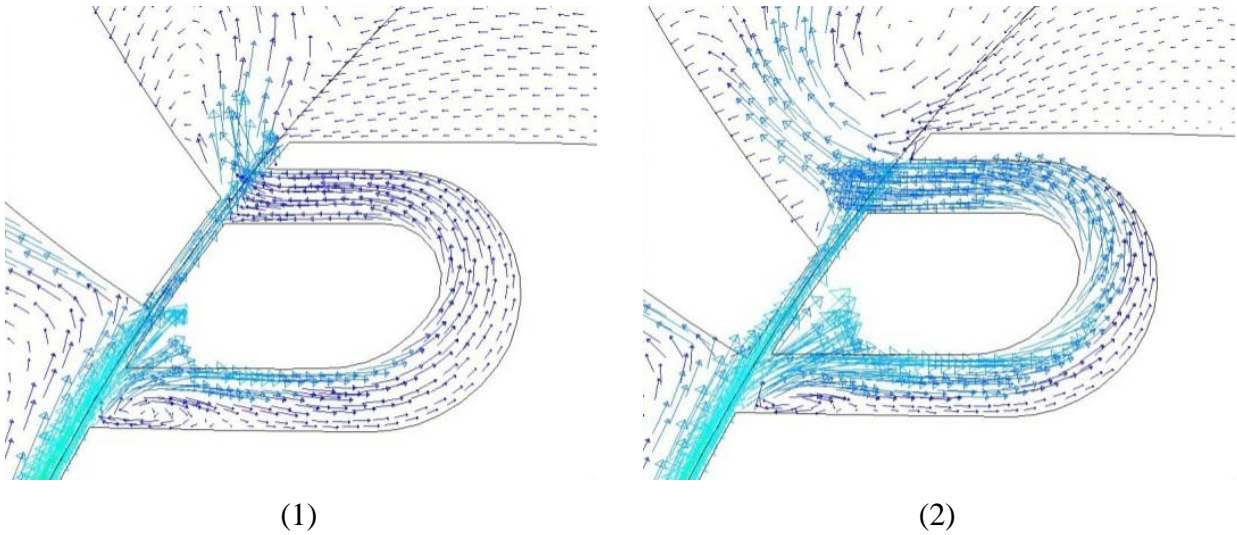
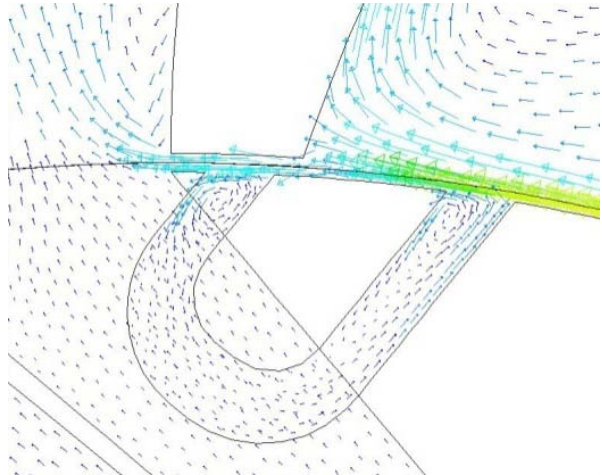Figure 75: Velocity vector plot sequence of the left U channel during one channel period
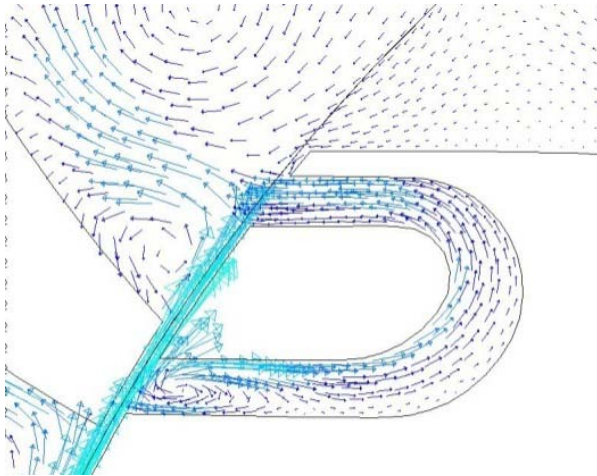
(3)
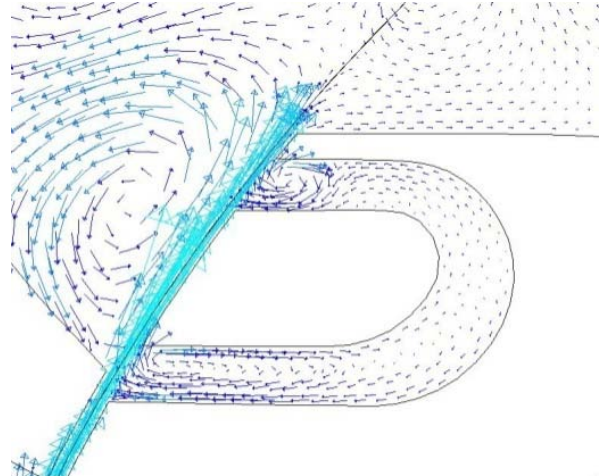
(4)
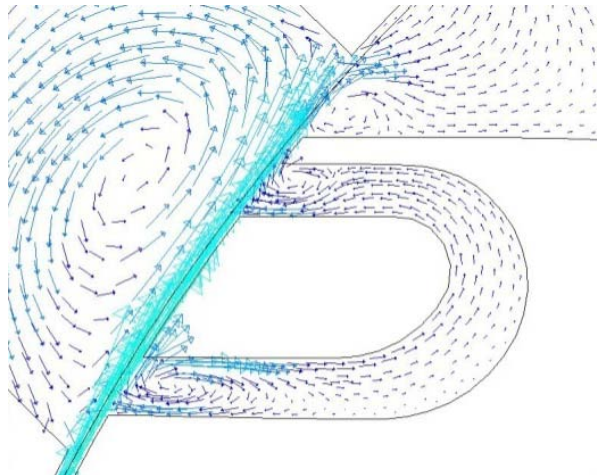
(5)

(6)

(7)

(8)

Figure 75 Con't
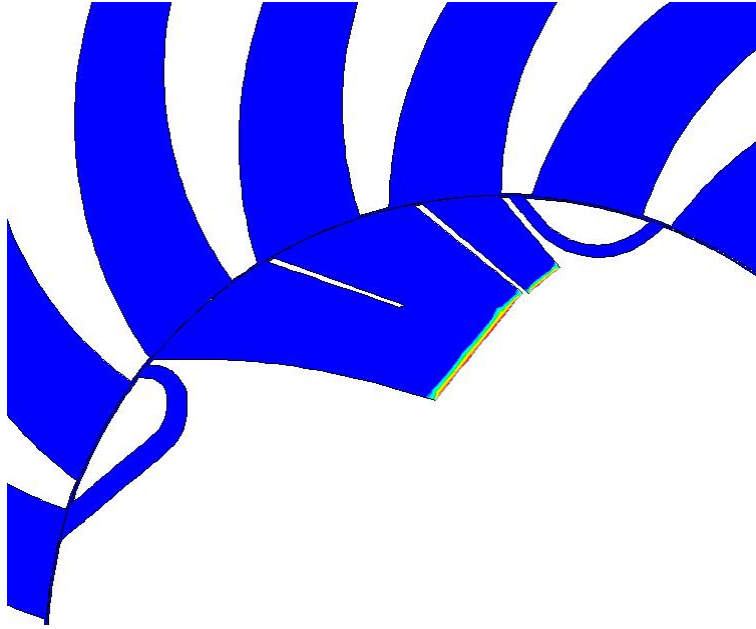
<div align="center">(1)</div>

<div align="center">(2)</div>

<div align="center">(3)</div>

<div align="center">(4)</div>
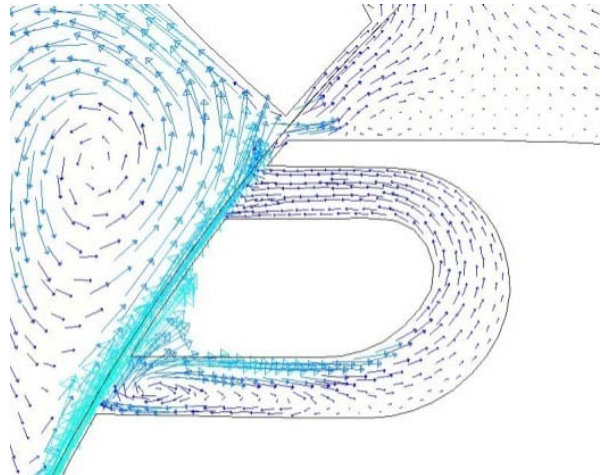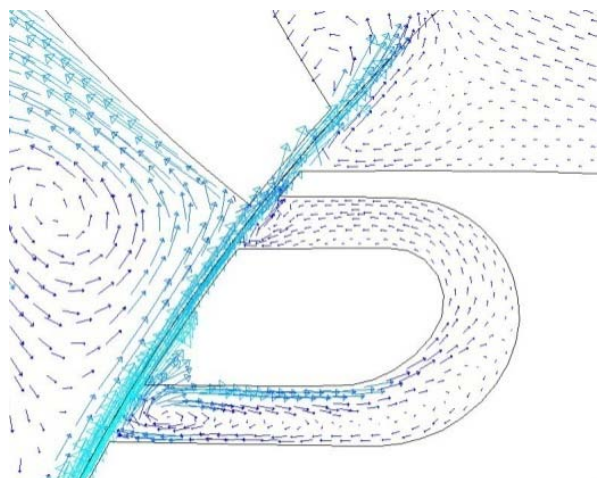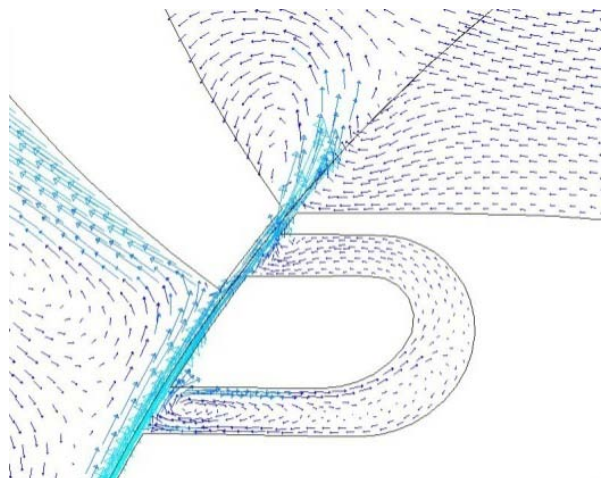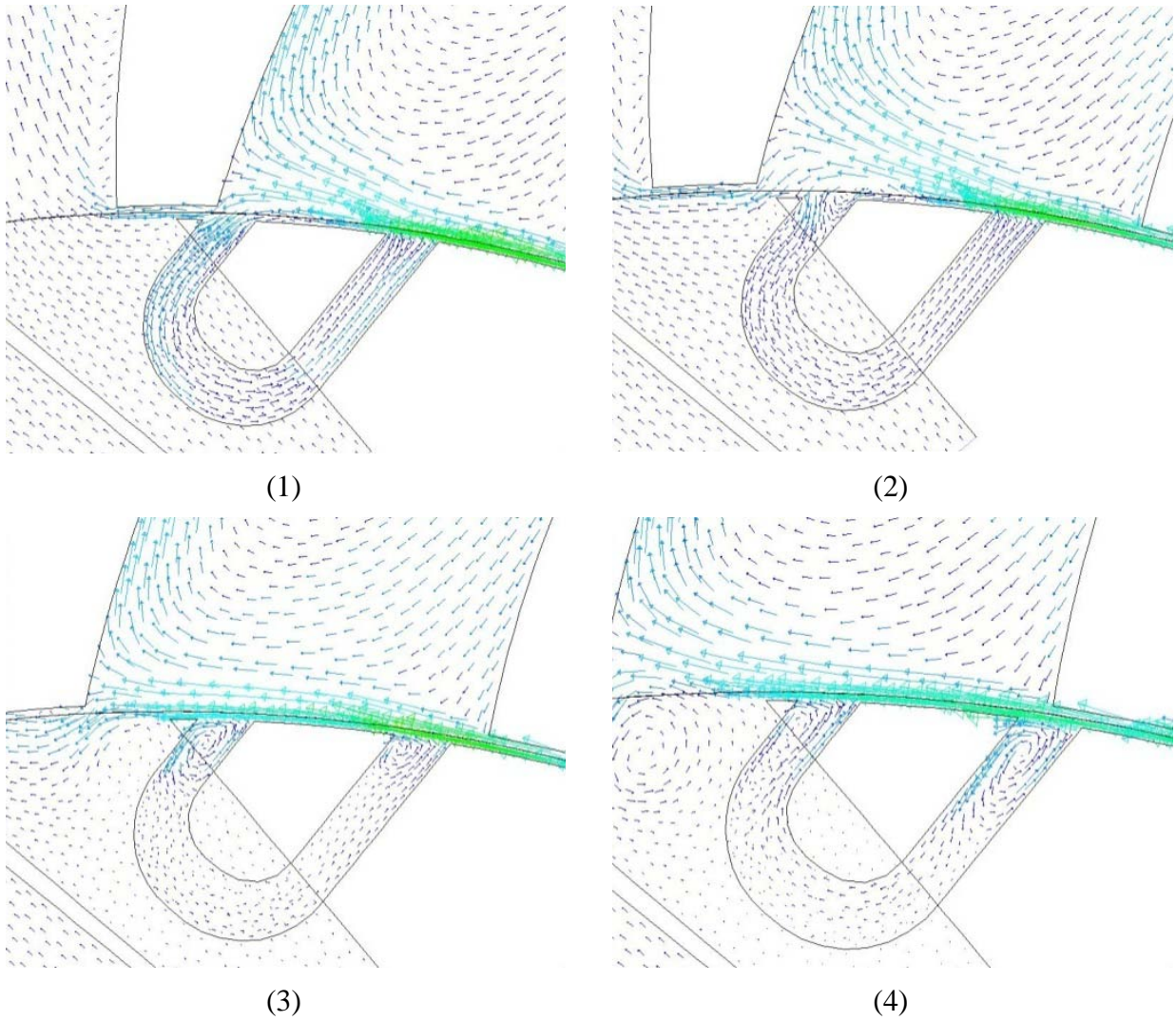
Figure 76: Velocity vector plot sequence of the right U channel during one channel period
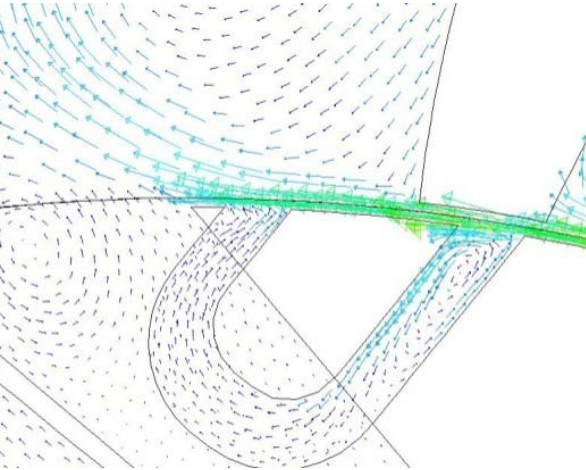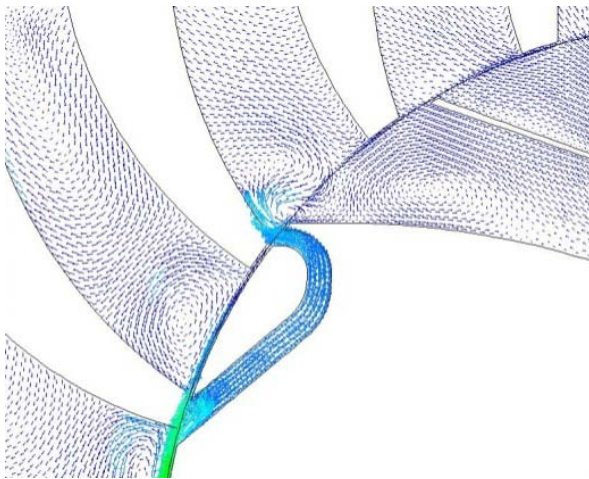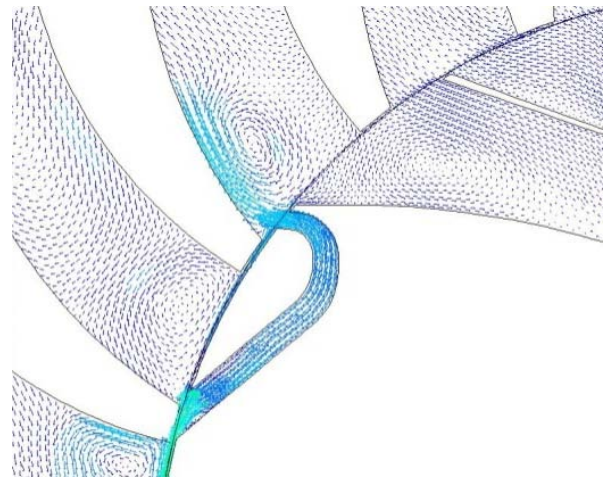
(5)
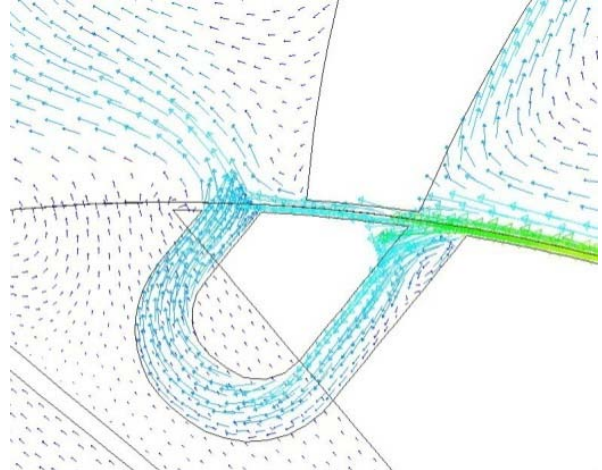
(6)
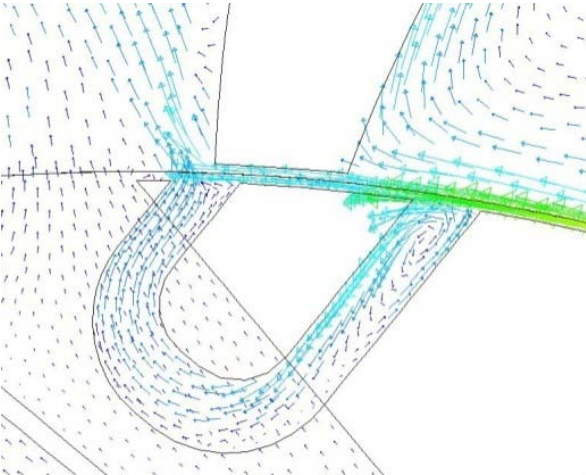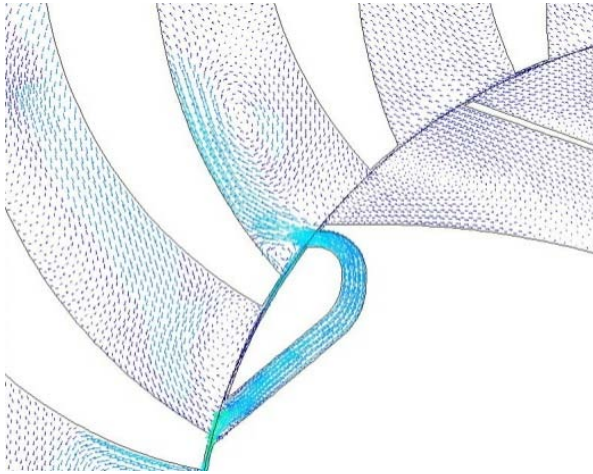
(7)

(8)

Figure 76 Con't

Figure 77: Geometry of the MU channel

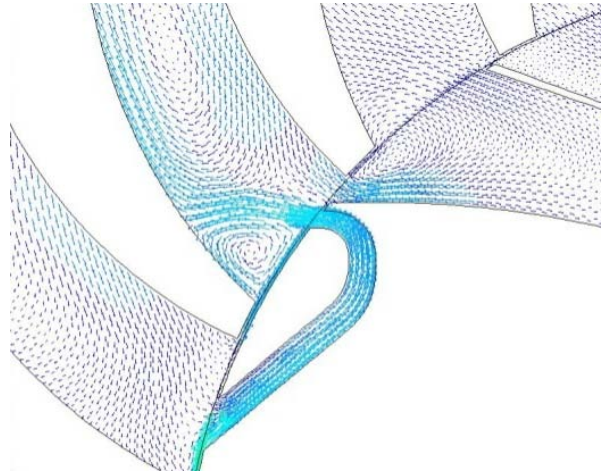| (1) | (2) |

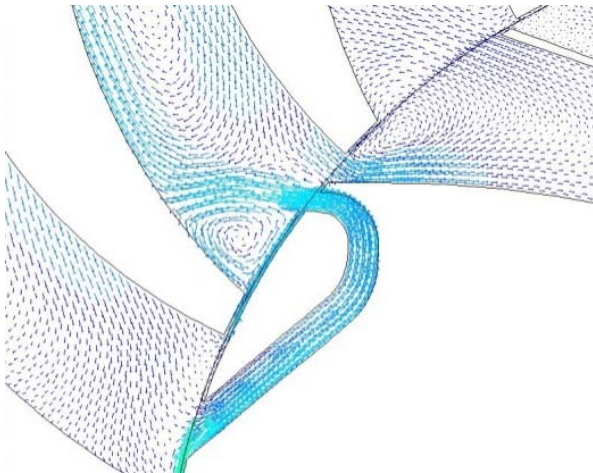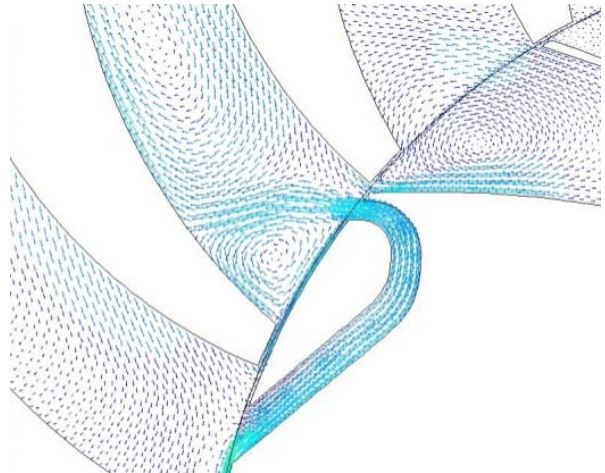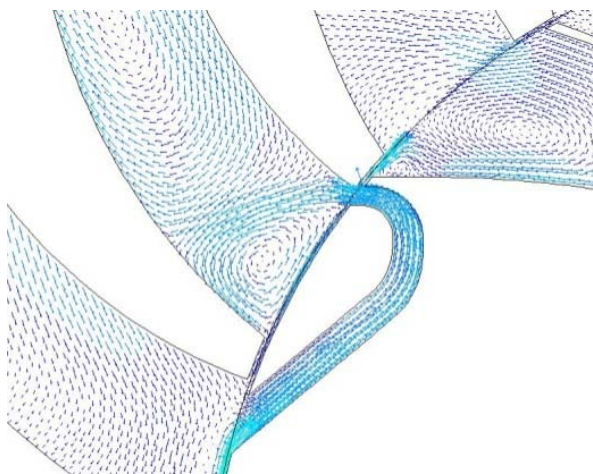Figure 78: Velocity vector plot sequence of the left MU channel during one channel period

(3)

(4)

(5)

(6)

(7)

(8)

Figure 78 Con't

(1)

(2)

(3)

(4)

Figure 79: Velocity vector plot sequence of the right MU channel during one channel period
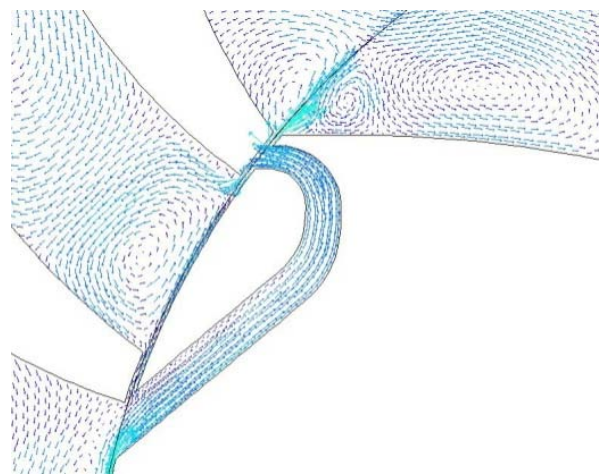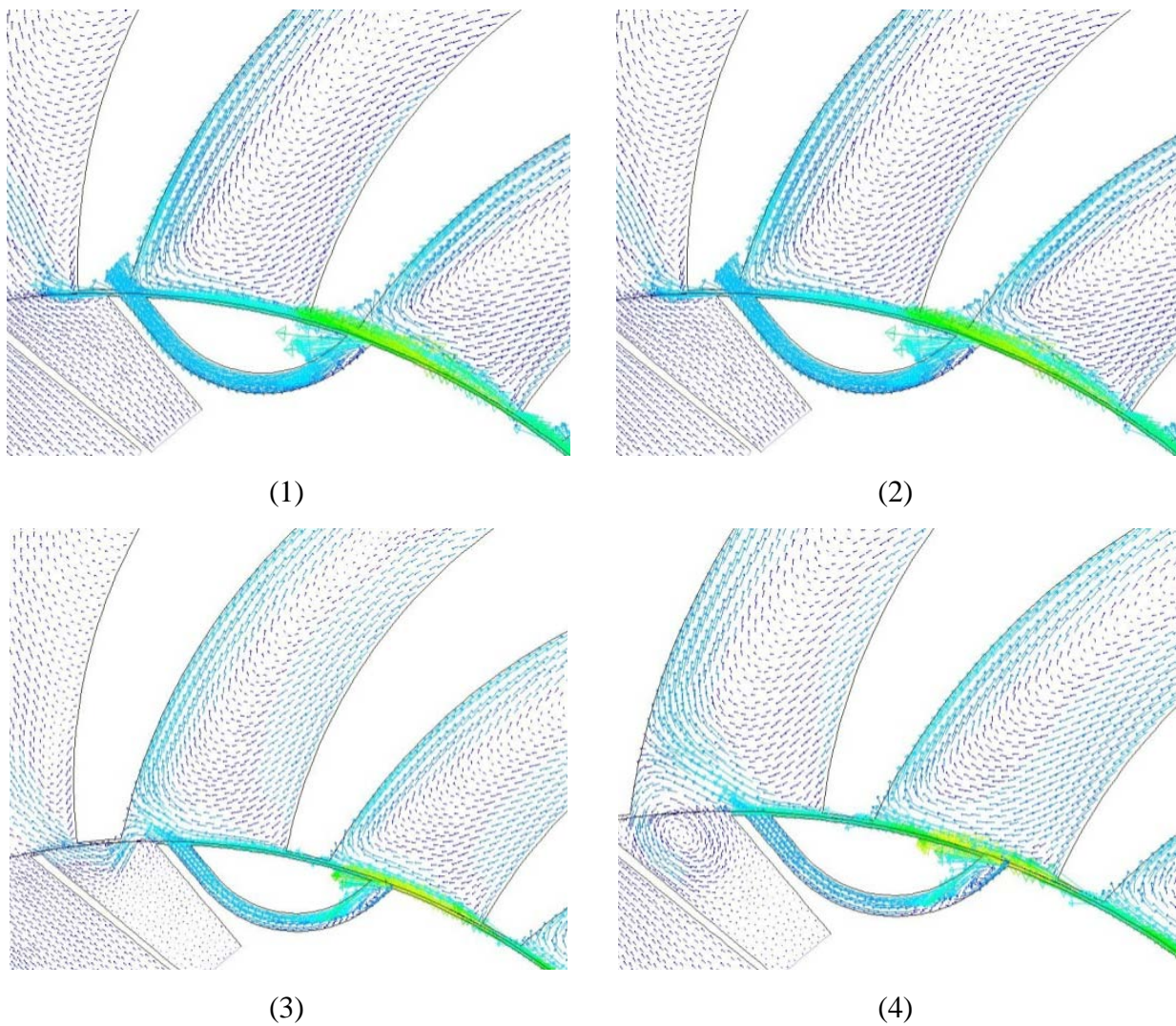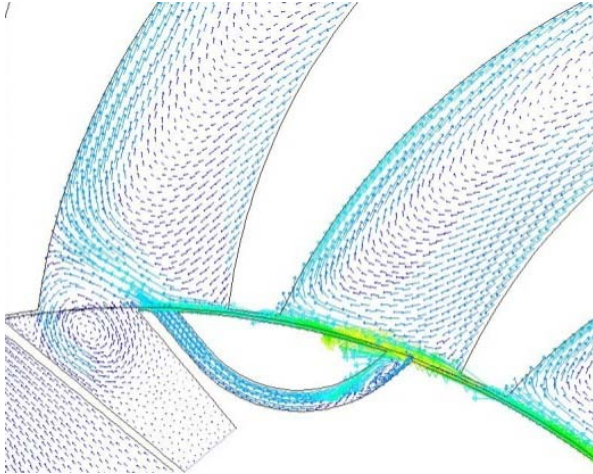
(5)
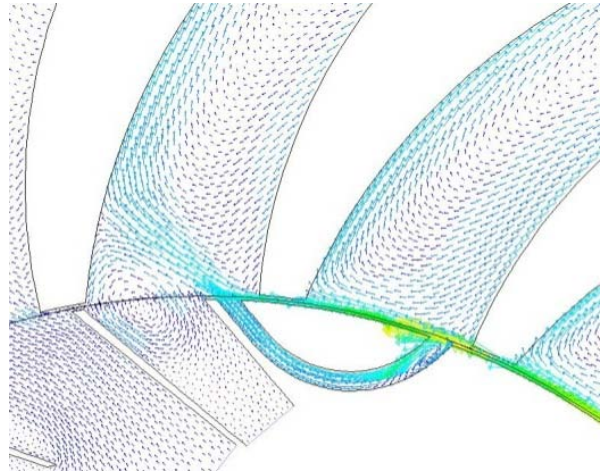
(6)
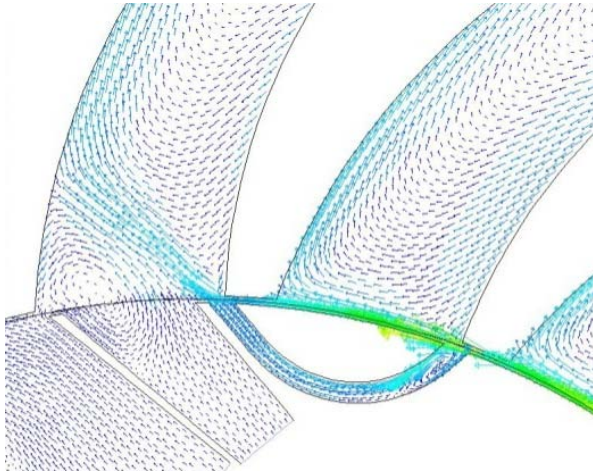
(7)
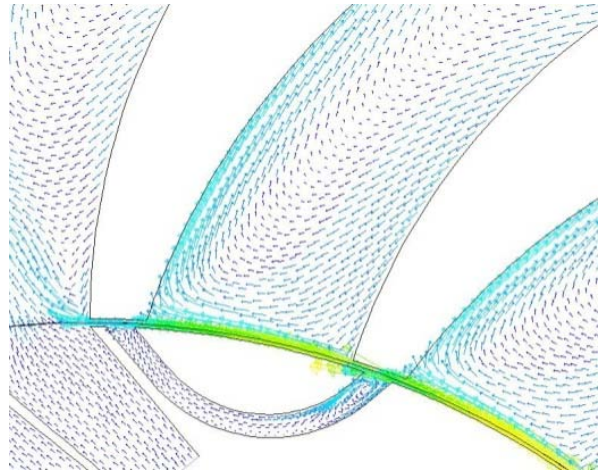
(8)

Figure 79 Con't
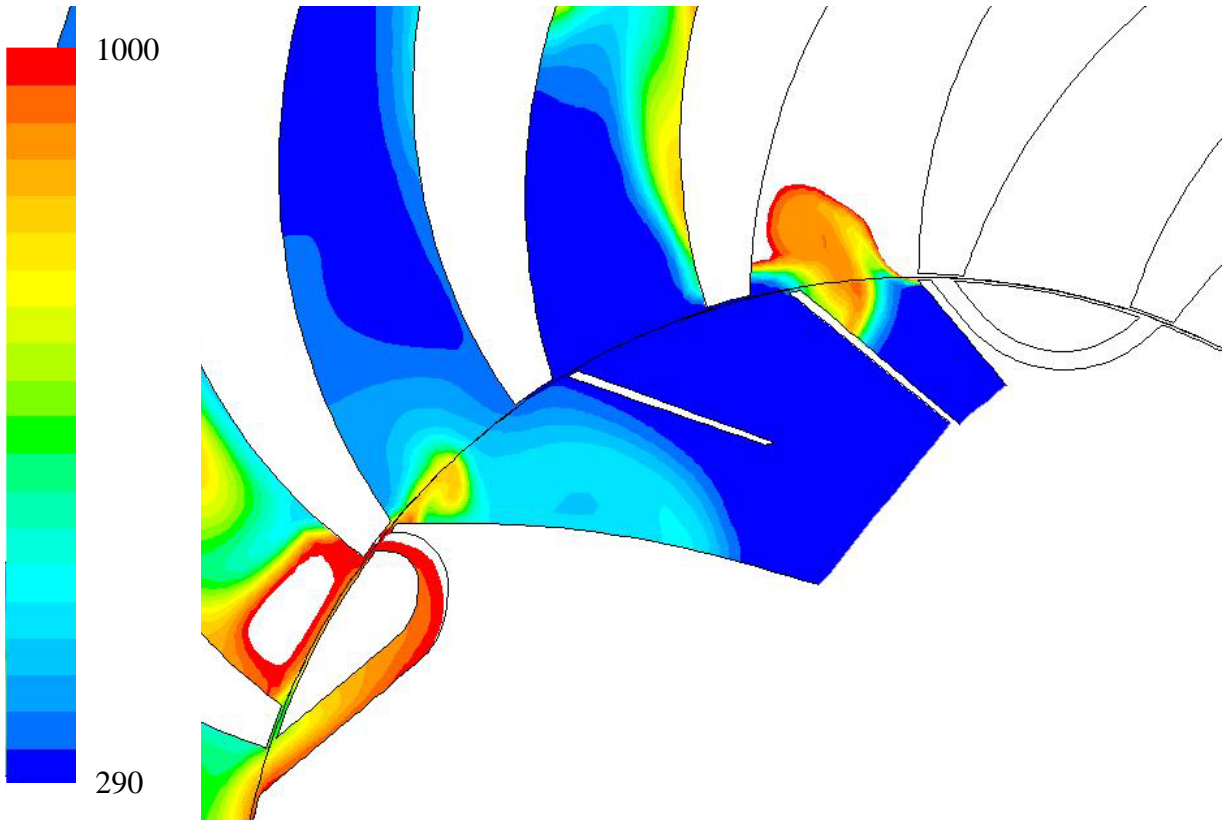
Figure 80: Temperature contour at the end of the third cycle from the pressure patching method for the MU channel design
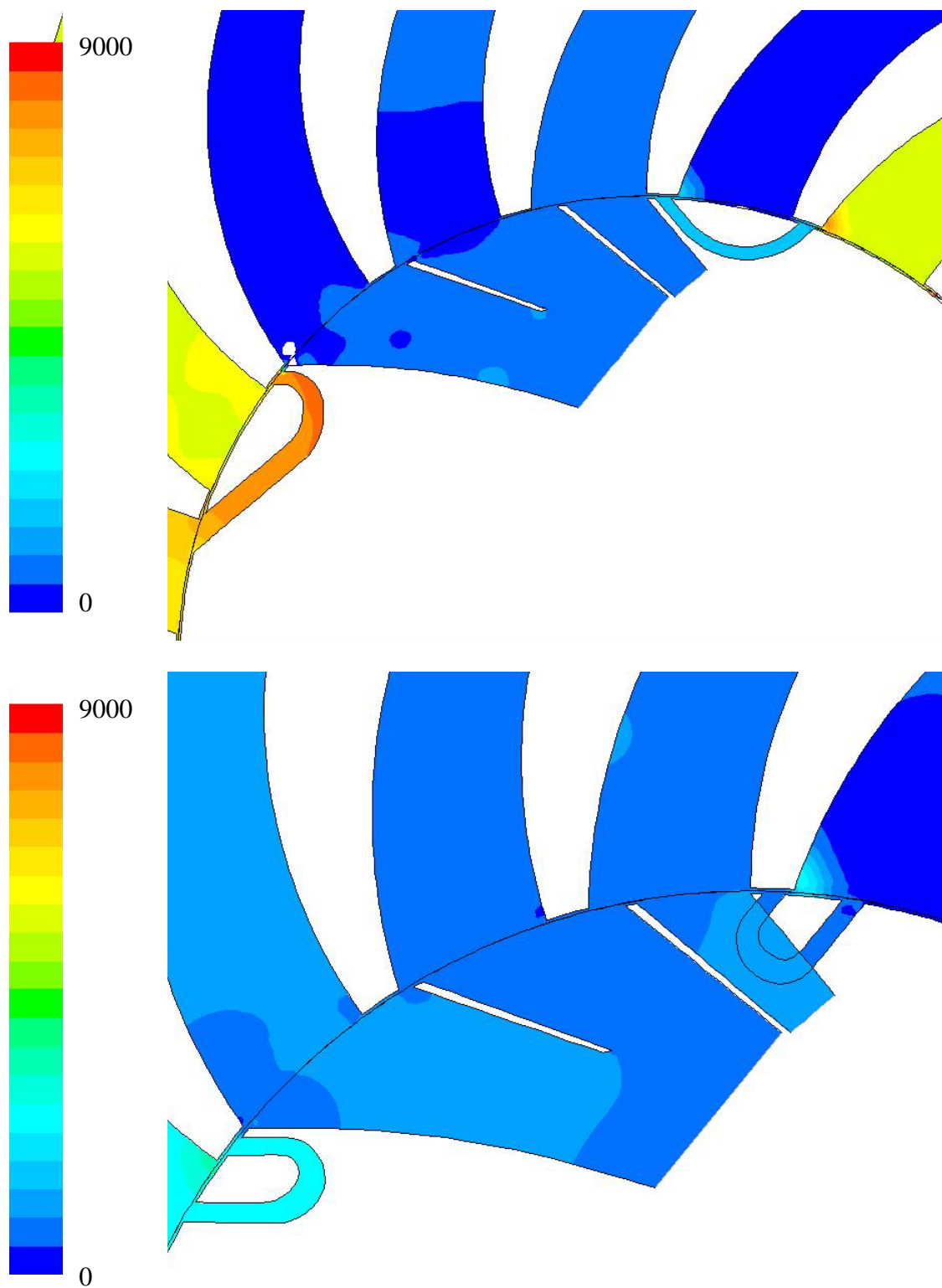
Figure 81: Comparison between the pressure in the MU channels (top) and U channels (bottom)
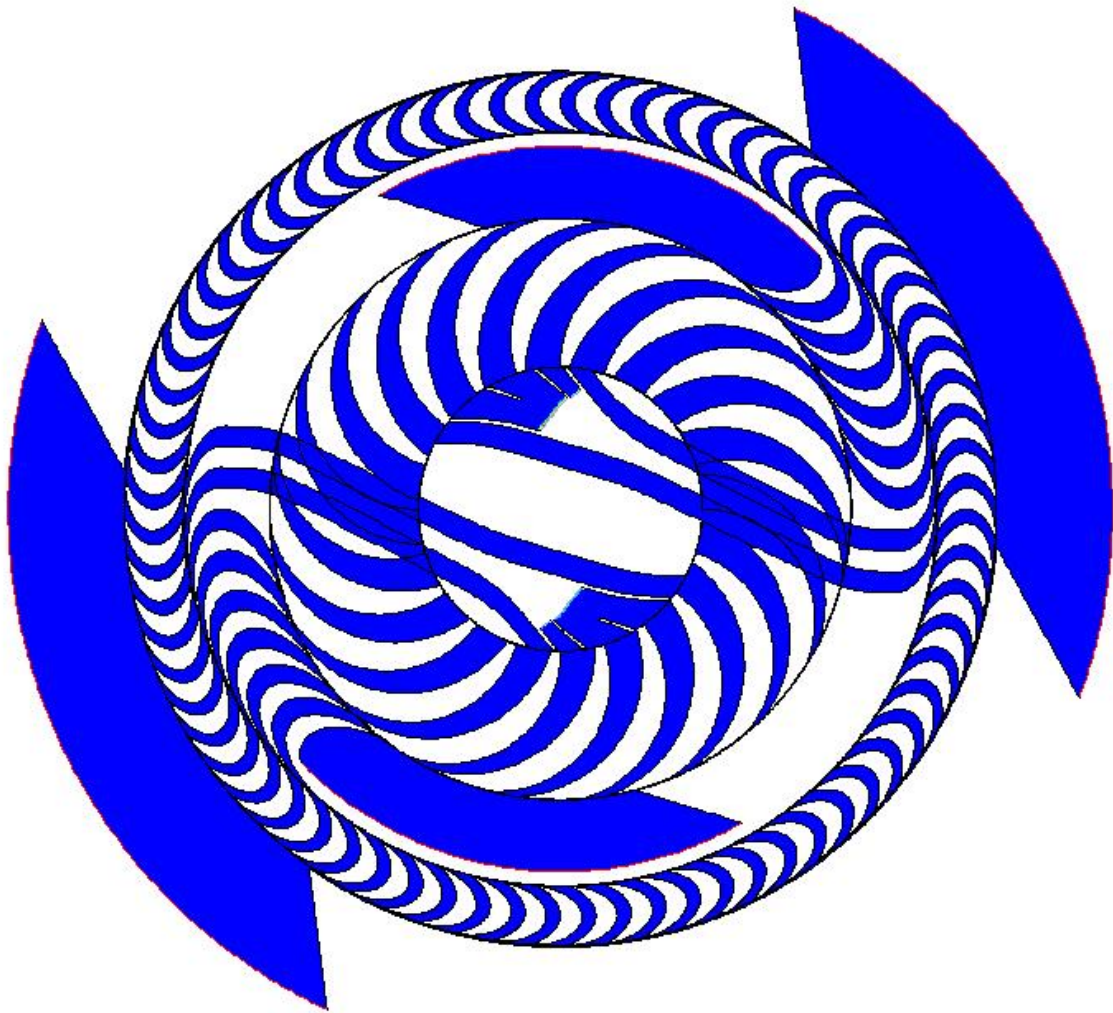
Figure 82: Configuration of a WDE with the leakage pipes
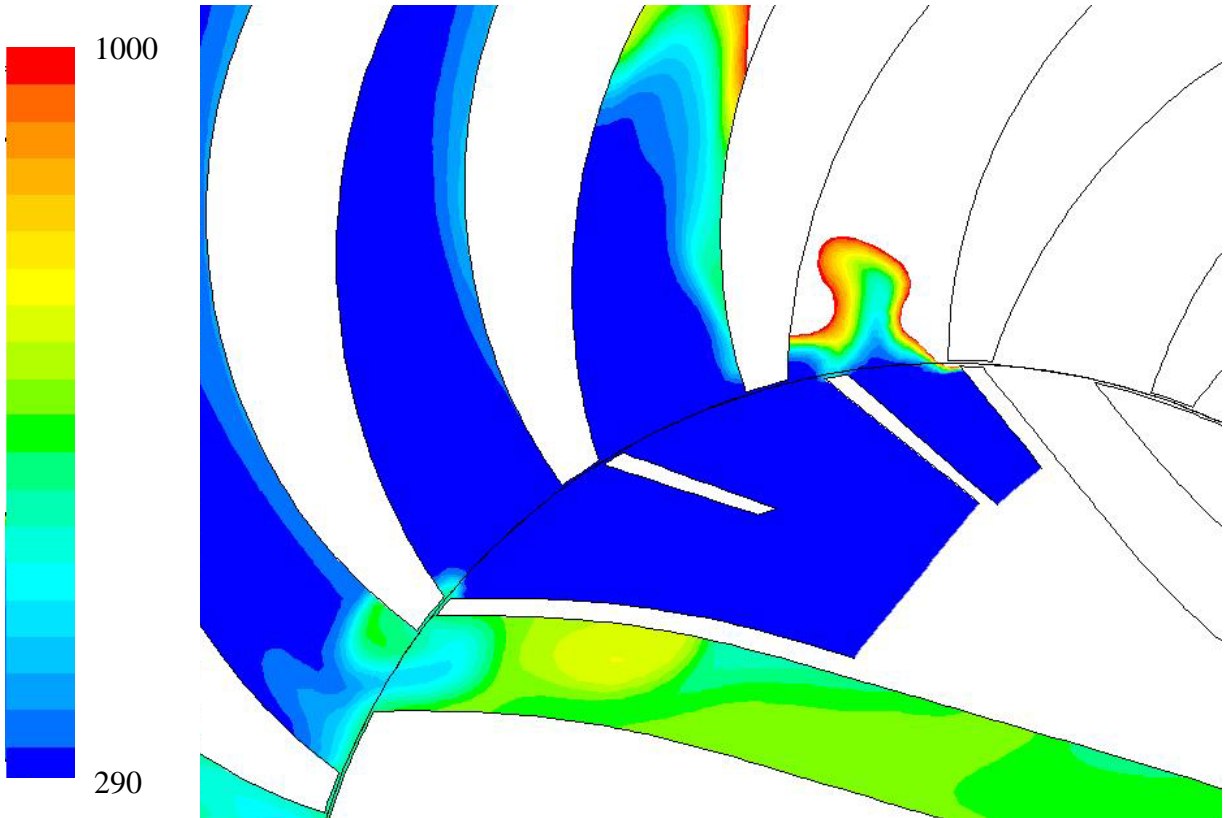
Figure 83: Temperature contour at the end of the third cycle from the pressure patching method for the leakage pipe design

Figure 84: Geometry of the jagged housing wall

Figure 85: Temperature contour at the end of the third cycle from the pressure patching method for the jagged wall design

0.055
0

Contour of mass fraction of methane

Figure 86: Using EGR to generate a shock wave and ignition

REFERENCES

REFERENCES

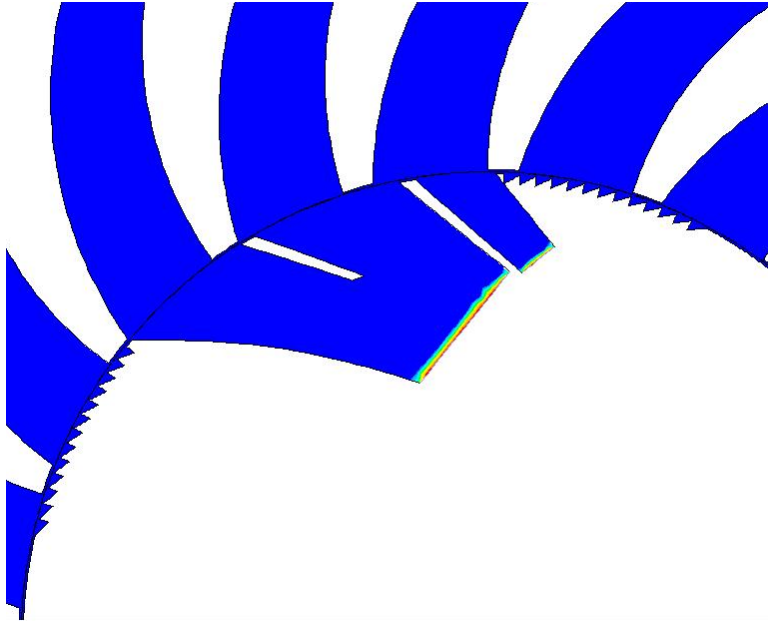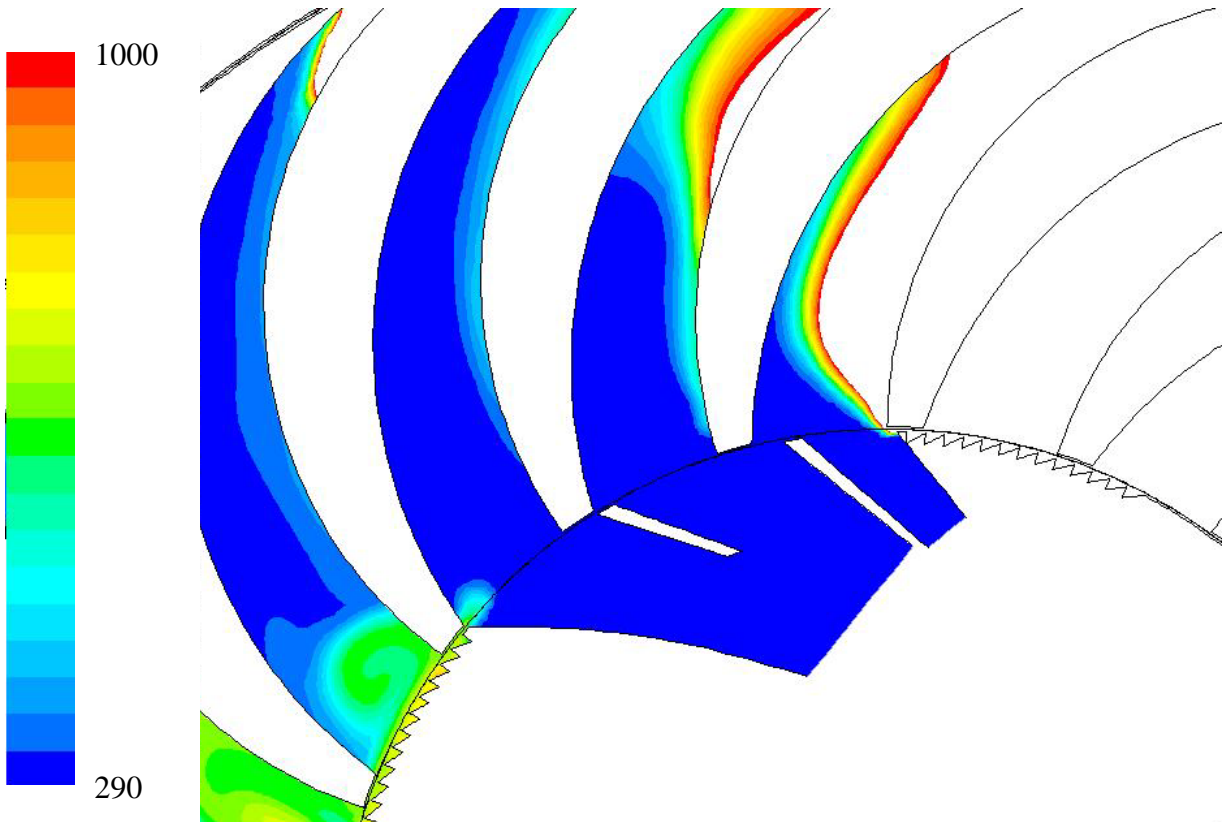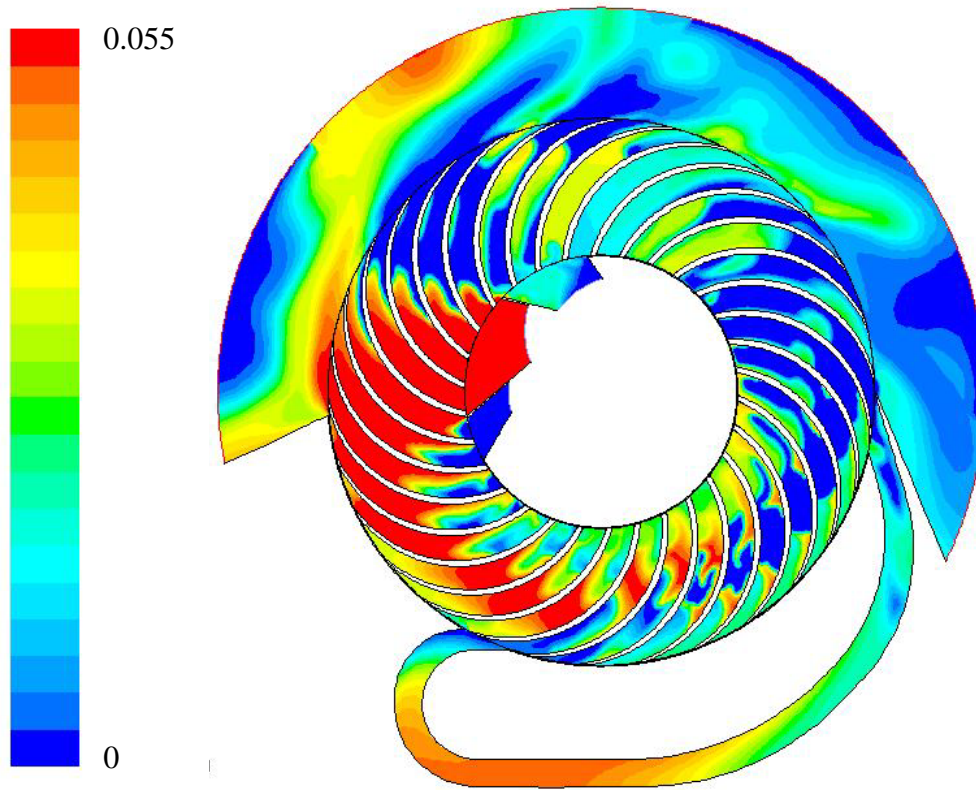[1] Anderson, John, 1995, "Computational Fluid Dynamics: the Basics with Applications", McGraw-Hill Science/Engineering/Math

[2] Aichlmayr, H. T., Kittelson, D. B., and Zachariah, M. R., "Micro-HCCI Combustion: Experimental Characterization and Development of a Detailed Chemical Kinetic Model with Coupled Piston Motion," Combustion and Flame, Vol. 135, No. 3, 2003, pp. 227-248.

[3] Akbari, P., Nalim, M. R., Mueller, N., "A Review of Wave Rotor Technology and Its Applications," ASME Journal of Engineering for Gas Turbines and Power, October 2006, Vol. 128, pp. 717-735.

[4] Akbari, P. and Nalim, M. R., "Review of Recent Developments in Wave Rotor Combustion Technology." Journal of Propulsion and Power, Vol. 25, No. 4, pp 833-844, July–August 2009.

[5] Akbari, P., and Nalim, M. R., "Analysis of Flow Processes in Detonative Wave Rotors and Pulse Detonation Engines," AIAA Paper 2006-1236, 2006.

[6] Akbari, P., Alparslan, B., Kilchyk, V., and Nalim, M. R., "Numerical Analysis of Hydrogen-Fueled Wave Rotors for Gas Turbine Applications," First International Hydrogen Energy Congress, Turkey, 2005.

[7] Azim A., 1974, "An Investigation Into the Performance and Design of Pressure Exchangers," Ph.D. Thesis, University of London.

[8] Azoury P.H., Hai S.M., 1975, Computerized analysis of dynamic pressure exchanger scavenge process, Proc. I Mech E vol. 189/18/75 pp. 149-158

[9] Board on Army Science and Technology, "Meeting the Energy Needs of Future Warriors" National Research Council of The National Academies, Washington, DC, 2004.

[10] Brouillette, M., " Shock Waves at Microscales," Shock Waves, Vol. 13, No. 1, 2003, pp. 3-12.

[11] Clarke, J. F., "Fast Flames, Waves and Detonation," Progress in Energy and Combustion Science, Vol. 15, No. 3,1989, pp. 241-271.

[12] Edwards, D. H., Fearnley, P. and Nettleton, M. A., "Shock diffraction in channels with 90 deg bends", Journal of Fluid Mechanics (ISSN 0022-1120), vol. 132, July 1983, p. 257-270.

[13] Epstein, A. H., "Millimeter-Scale, Micro-Electro-Mechanical Systems Gas Turbine Engines," ASME Journal of Engineering for Gas Turbines and Power, Vol. 126, No. 2, 2005, pp. 205-226.

[14] Fatis A., and Ribaud Y., 1997, "Numerical Analysis of the Unsteady Flow Inside Wave Rotors Applied to Air Breathing Engines," 13 International Symposium on Airbreathing Engines

[15] Fatis A., Lafond and Ribaud Y., 1998, "Preliminary Analysis of the Flow Inside a Three-Port Wave Rotor by Means of a Numerical Model," Aerospace Science and Technology, Vol. 2, No. 5, pp. 289-300

[16] Fatis A., and Ribaud Y., 1999, „Thermodynamic Analysis of Gas Turbines Topped with Wave Rotors," Aerospace Science and Technology, Vol. 3, No. 5, pp. 293-299.

[17] Fernandez-Pello, A. C., Pisano, A. P., Fu , K., Walther, D. C., Knobloch, A. K., Martinez, F. C., Senesky, M., Stoldt, C., Maboudian, R. M., Sanders, S., and Liepmann, D., "MEMS Rotary Engine Power System," Proceedings of IEEE Transactions on Sensors and Micromachines, Vol. 123, No. 9, 2003, pp. 326-330.

[18] Fong, K. K., and Nalim, M. R., "Gas Dynamic Limits and Optimization of Pulsed Detonation Static Thrust," AIAA Paper 2000-3471, 2000.

[19] Hilsenrath, Joseph; et al.: Tables of Thermal Properties of Gases. Circ. 564, National Bureau of Standards, Nov. 1, 1955

[20] Iancu. F, Piechna. J, Dempsey. E, and Müller. N, "The Ultra-Micro Wave Rotor Research a t Michigan State University, second International Symposium on Innovative Aerial/Space Flyer Systems, The University of Tokyo, 2005, pp 65–70.

[21] Iancu, F., Piechna. J., Dempsey. E and Müller N, "Ultra-Micro Wave Rotor Investigations," fifth International Workshop on Micro and Nanotechnology for Power Generation and Energy Conversion Applications, Japan, 2005, pp 93–96.

[22] Izzy, Z., and Nalim, M. R., "Wave Fan and Rotary-Ejector Pulsed Performance Prediction," AIAA Paper 2002-4068, 2002.

[23] Jonsson, V. K., Matthews, L., and Spalding, D. B., 1973, "Numerical Solution Procedure for Calculating the Unsteady, One-Dimensional Flow of Compressible Fluid," ASME Paper 73-FE-30.

[24] Kentfield, J. A. C., 1993, Nonsteady, one-dimensional, internal, compressible flows, Oxford University Press

[25] Kentfield, J. A. C, Thermodynamics of airbreathing pulse-detonation engines, Journal of Propulsion and Power (2002), Volume: 18, Issue: 6, Publisher: American Inst. Aeronautics and Astronautics Inc., Pages: 1170-1175

[26] Litke, P. J., Schauer, F. R., Paxson, D. E., Bradley, R. P., and Hoke, J. L., "Assessment of the Performance of a Pulsejet and Comparison with a Pulsed-Detonation Engine," AIAA Paper 2005-0228, 2005.

[27] Matthews L., 1969, "An Algorithm for Unsteady Compressible One-Dimensional Fluid Flow," M.S. Thesis, University of London.

[28] Mawid, M. A., and Sekar, B., "A Numerical Study of Active Control of Combustion-Driven Dynamic Instabilities in Gas-Turbine Combustors," AIAA Paper 1999-2778, 1999.

[29] Nalim, M. R., "Longitudinally Stratified Combustion in Wave Rotors," Journal of Propulsion and Power, Vol. 16, No. 6, 2000, pp. 1060-1068.

[30] Nalim, M. R., and Paxson, D. E., "A Numerical Investigation of Premixed Combustion in Wave Rotors," Journal of Engineering for Gas Turbines and Power, Vol. 119, No. 3, 1997, pp. 668-675.

[31] Nalim, M. R., and Jules, K., "Pulse Combustion and Wave Rotors for High-Speed Propulsion Engines," AIAA Paper 98-1614, 1998.

[32] Nalim, M. R., and Izzy, Z, "Rotary Ejector Enhanced Pulsed Detonation System," AIAA Paper 2001-3613, 2001.

[33] Nalim, M. R., and Izzy, Z, "Simulation of a Wave Rotor Pulse Detonation Engine with Integrated Ejector," ISABE Paper 2001-1214, 2001.

[34] Nalim, M. R., "Rotary Ejector Enhanced Pulsed Detonation System and Method," US Patent 6,845,620, 2005.

[35] Paxson D. E.,1992, "A General Numerical Model for Wave Rotor Analysis,"NASA TM 105740, July.

[36] Paxson D. E., 1993, „A Comparison Between Numerically Modeled and Experimentally Measured Loss Mechanisms in Wave Rotors," AIAA Paper 93-2522.

[37] Paxson D. E., 1995,"A Comparison Between Numerically Modelled and Experimentally Measured Loss Mechanisms in Wave Rotors," AIAA Journal of Propulsion and Power, Vol. 11, No. 5, pp. 908-914, (also NASA TM 106279).

[38]Paxson D. E., 1995, "A Numerical Model for Dynamic Wave Rotor Analysis," AIAA Paper 95-2800. Also NASA TM-106997.

[39]Paxson D. E.,1996, "Numerical Simulation of Dynamic Wave Rotor performance," AIAA Journal of Propulsion and Power, Vol. 12, No. 5, pp.949-957, (also, NASA TM 106997).

[40]Paxson D. E., 1997, "A Numerical Investigation of the Startup Transient in a Wave Rotor," ASME Journal of Engineering for Gas Turbines and Power, Vol.119, No. 3, pp. 676-682, also ASME Paper 96-GT-115, June, 1996, (also, NASA TM 107196).

[41]Paxson D. E., 1997, "A Numerical Investigation of the Startup Transient in a Wave Rotor," Journal of Engineering for Gas Turbines and Power, 119, No. 3, pp. 676-682. Also ASME Paper 96-GT-115, and NASA TM 107196.

[42]Paxson, D. E., 1998, "An Incidence Loss Model for Wave Rotors With Axially Aligned Passages, " AIAA-98-3251, July, 1998; also NASA TM-1998-207923.

[43]Paxson, D. E., "Wave Augmented Diffusers for Centrifugal Compressors," AIAA Paper 98-3401, 1998.

[44]Paxson, D. E., "An Improved Numerical Model for Wave Rotor Design and Analysis," AIAA Paper 93-0482, 1993.

[45]Paxson, D. E., and Wilson, J., "Recent Improvements to and Validation of the One Dimensional NASA Wave Rotor Model," NASA TM-106913, 1995.

[46]Paxson, D. E., "A Numerical Investigation of the Startup Transient in a Wave Rotor," Journal of Engineering for Gas Turbines and Power, Vol. 119, No. 3, 1997, pp. 676-682.

[47]Paxson, D. E., and Lindau, J. W., "Numerical Assessment of Four-Port Through-Flow Wave Rotor Cycles with Passage Height Variation," AIAA Paper 97-3142, 1997.

[48]Paxson, D. E., "A Sectored-One-Dimensional Model for Simulating Combustion Instabilities in Premix Combustors," AIAA Paper 2000-0313, 2000.

[49]Paxson, D. E., and Perkins, H. D., "Thermal Load Considerations for Detonative Combustion-Based Gas Turbine Engines," AIAA Paper 2004-3396, 2004.

[50]Paxson, D. E., "Performance Evaluation Method for Ideal Airbreathing Pulse Detonation Engines," Journal of Propulsion and Power, Vol. 20, No. 5, 2004, pp. 945-947.

[51]Perkins, H. D., Paxson, D. E., Povinelli, L. A., Petters, D. P., Thomas, S. R., Fittje, J. E., and Dyer, R. S., "An Assessment of Pulse Detonation Engine Performance Estimation Methods Based on Experimental Results," AIAA Paper 2005-3831, 2005.

[52] Piechna J 2005 Wave machines, models and numerical simulation Oficyna Wydawnicza Politechniki Warszawskiej,Warszawa

[53] Piechna, J. R., "Feasibility Study of the Wave Disk Micro-Engine Operation," Journal of Micromechanics and Microengineering, Volume 16, Number 9,   pp. 270-281, 2006.

[54] Pohořelský, L., Obernesser, P., Vavra J., Klir, V., Macek, J, "1-D Model and Experimental Tests of Pressure Wave Supercharger." ASME Paper IMECE2007-43427, Seattle 2007, Washington, USA.

[55] Pohořelský, L., Sané P. A., Rozsas T., Müller, N, "Wave Rotor Design Procedure for Gas Turbine Engine Enhancement." Proceedings of ASME Turbo Expo 2008, Berlin, June 2008.

[56] Resler E., Moscari J., Nalim R., 1994, Analytic design methods for wave rotor cycles, AIAA Joumal of Propulsion and Power 10 (5)

[57] Spadaccini, C. M., Mehra, A., Lee, J., Zhang, X., Lukachko, S., and Waitz, I. A., "High Power Density Silicon Combustion Systems for Micro Gas Turbine Engines," ASME Journal of Engineering for Gas Turbines and Power, Vol. 125, No. 3, 2003, pp. 709-719.

[58] Spadaccini, Peck, J., and Waitz, I. A., "Catalytic Combustion Systems for Microscale Gas Turbine Engines," ASME Journal of Engineering for Gas Turbines and Power, Vol. 129, No. 1, 2007, pp. 49-60.

[59] Snyder, P., Alparslan, B., and Nalim, M. R., "Gas Dynamic Analysis of the Constant Volume Combustor, A Novel Detonation Cycle," AIAA Paper 2002-4069, 2002.

[60] Snyder, P., Alparslan, B., and Nalim, M. R., "Wave Rotor Combustor Test Rig Preliminary Design," ASME Paper IMECE2004-61795, 2004.

[61] Horrocks G.D., Reizes J.A., Mallinson S.G., 1998, Numerical study of flow in a rotating shock tube, 13th Australasian Fluid Mechanics Conference Monash University, Melbourne, Australia 13-18 December 1998

[62] MacCormack, Robert W.: The Effect of Viscosity in Hypervelocity Impact Cratering. AIAA-69-354, Apr.-May 1969.

[63] D Gottlieb and E Turkel, Dissipative two–four methods for time dependent problems. Math. Comp., 30 (1976), p. 703

[64] Dongfang Liang, BinLiang Lin, Roger Alexander Falconer, Simulation of rapidly varying flow using an efficient TVD-MacCormack scheme, International Journal for Numerical Methods in Fluids (2007) Volume: 53, Issue: August 2006, Pages: 811-826

[65] William H Heiser, David T Pratt, Thermodynamic cycle analysis of pulse detonation engines, Journal of Propulsion and Power (2002), Volume: 18, Issue: 1, Publisher: American Inst. Aeronautics and Astronautics Inc., Pages: 68-76

[66] E. Wintenberger and J. E. Shepherd "Thermodynamic Analysis of Combustion Processes for Propulsion Systems." 4second AIAA Aerospace Sciences Meeting and Exhibit, Jan 5-8, Reno NV 2004. AIAA2004-1033.

[67] Weber, Helmut E., 1995, Shock Wave Engine Design, John Wiley and Sons, New York

[68] Wilson J. and Paxson D.E.: Jet engine Performance Enhancement through Use of a Wave-Rotor Topping Cycle. NASSA TM-4486, 1993

[69] Zehnder G., 1970, Berechnungsaufgaben bei der Entwicklung des Comprex. Schweizerische Bauzeitung, 88. Jahrgang, Heft 30, 23. Juli, 1970.

[70] Zehnder G., 1971, Berechnung von Druckwellen in der Auf ladetechnik. Brown Boveri Mitt 4/5 - 71.

[71] Zehnder G., 1971, "Calculating Gas Flow in Pressure-Wave Machines" Brown Boveri Review, No. 4/5, pp. 172-176.